# Probing Micromotion in a Multi-Segmented Blade-Style Ion Trap

by

Fabien Lefebvre

A thesis
presented to the University of Waterloo
in fulfillment of the
thesis requirement for the degree of
Master of Science
in
Physics (Quantum Information)

Waterloo, Ontario, Canada, 2025

© Fabien Lefebvre 2025

## Author's Declaration

I hereby declare that I am the sole author of this thesis. This is a true copy of the thesis, including any required final revisions, as accepted by my examiners.

I understand that my thesis may be made electronically available to the public.

## Abstract

Trapped ions are a leading candidate in quantum computing platforms. Their all-to-all connectivity and high-fidelity multi-qubit interactions serve as an essential pillar for scaling up quantum computing. Trapping linear chains of $^{171}Yb^{+}$ ions has applications ranging from digital quantum computation to analog quantum simulation of physically relevant models. Whilst these applications seem attractive, many experimental challenges prevent trapped ions from easily scaling up. The quadrupole multi-segmented blade-style trap is a leading trap architecture for quantum simulation because of its deep and quadratic confining potential, high optical access and capability to hold long chains of ions. Although, blade-style traps face challenges such as complex electronics control and ion heating caused by micromotion.

Blade-style traps are traditionally hand assembled, and therefore are prone to misalignment, leading to increased levels of micromotion. This limitation causes many adverse effects, all negatively contributing to the quality of the quantum simulations performable with the blade-style trap.

In this thesis, I will describe my work in building the electronic infrastructure to confine long chains of $^{171}Yb^{+}$ ions in a multi-segmented blade-style trap. The bulk of my work will focus on probing micromotion in the trap by using a repump transition with a narrow enough linewidth. I will first present some background on ion dynamics, micromotion and fundamentals of ion trapping. Afterwards, I will discuss the multi-segmented blade-style trap used in this work, along with the electronics that I designed to drive the confining electromagnetic fields. A novel approach of using a balanced radio-frequency drive along with completely out-of-vacuum electronics allows us to reach high secular frequencies. Using this approach, we demonstrate long chains of up to 25 ions with qubit phase coherence exceeding 0.9 s, demonstrating good control over the magnetic field level. The rest of the thesis will present our approach to probe and minimize micromotion in the segmented blade-style trap. Here, I will demonstrate that our results show inherently low micromotion without any compensation fields, indicating that the assembly of the blades is quite optimal. Displacements below 1 $\mu$m are required radially to find the micromotion null. Additionally, I will demonstrate that there is low micromotion at the center and edge of a long chain of ions, showing that for large-scale quantum simulations, we can expect low axial and radial micromotion across a long chain of up to 25 ions. These results demonstrate that hand-assembled blade-style traps can exhibit inherently low excess micromotion, such that the inherent micromotion is at the limit of resolvability for the sideband spectroscopic method. This work will is crucial for obtaining low micromotion for when we eventually run large-scale quantum simulations in this trap.

**Acknowledgements**

Commencer une nouvelle vie dans une nouvelle ville n'était pas la décision la plus facile. Malgré, les amis que je me suis fait ainsi que les souvenirs de ces deux dernières années m'empêchent de regretter mon choix.

Merci à mes parents, André et Lucie pour le support tout aux long de mes études, et de croire en mon succès. Que ce soit des soupers congelés que ma mère m'envoyait, ou des appels lorsque Ottawa me manquait, ils trouvaient toujours une façon de me soutenir à distance. Si j'ai pu arriver jusqu'ici, c'est grâce aux parents formidables que vous avez toujours été.

À mes frères, Jacob et Ludovic, merci pour les beaux souvenirs qu'on a la chance de vivre lorsqu'on se voit quelques fois par année.

À mes amis d'adolescence, Jacob, Caleb et Cameron, merci d'être de tellement bons amis fidèles. C'est incroyable à quel point nous sommes restés proches malgré être situé dans 3 villes distantes.

À mes amis que je me suis fait à Waterloo, Zach, Andy, Noah, Ali, Aki, Lars, Raj, Addison, Ruhi, Chris, Everett, Terry et plusieurs autres, merci pour les beaux souvenirs qu'on a eu la chance de vivre ensemble. Même si nous allons probablement tous éventuellement déménager dans des villes distinctes, je n'oublierai jamais ce groupe d'amis.

Merci à mon superviseur, Rajibul, pour m'avoir transmis tant de connaisances scientifiques, et de m'avoir partagé ton appréciation pour les ions piégés. Merci pour m'avoir formé comme académique, ainsi que de m'avoir poussé à apprendre de nombreuses compétances qui me seront utiles sur le marché de travail.

Merci aux membres de mon comité, Ray, Jim et Bradley, pour les discussions et idées partagées.

Finalement, merci aux membres de mon groupe de recherche, Lewis, Shilpa, Sakshee, Anthony, Monica, Siddarth, Yu-Ting et Mahmood ainsi que les anciens étudiants gradués Nikhil, Sainath et Gilbert. Je n'aurais pas pu demander pour un meilleur groupe de recherche. Tout membre de l'équipe était chaleureux lors de mon arrivée, et notre passion collective pour notre recherche a motivé mon apprentissage. Merci également aux nombreux étudiants du premier cycle pour l'aide avec de nombreux projets.

## Dedication

To those who've ever second-guessed their potential — bet on yourself.

# Table of Contents

**Author's Declaration** ii

**Abstract** iii

**Acknowledgements** iv

**Dedication** v

**List of Figures** ix

**List of Tables** xi

**List of Abbreviations** xii

**1 Introduction** 1

1.1 Working with trapped ions . . . . . 1

1.1.1 Why trap ions? . . . . . 1

1.1.2 Characteristics of a good ion trap . . . . . 2

1.1.3 Literature review - micromotion . . . . . 3

1.2 Contributions . . . . . 4

1.3 Outline . . . . . 5

**2 Trapped ion dynamics and fundamentals** **6**
2.1 The linear Paul trap . . . 6
2.1.1 Confining a charged particle . . . 6
2.1.2 Confining electric fields . . . 7
2.1.3 Pseudopotential . . . 8
2.1.4 Ion motion . . . 10
2.2 Micromotion . . . 12
2.2.1 Micromotion in a quadrupole trap . . . 12
2.2.2 Quantifying micromotion . . . 13
2.2.3 Challenges associated with micromotion . . . 17
2.3 Trapped ion physics . . . 20
2.3.1 Trapping an ion . . . 20
2.3.2 State preparation and measurement . . . 22
2.3.3 Single qubit rotations . . . 22
2.4 Chapter conclusion . . . 24

**3 Blade-style trap electronics** **26**
3.1 Segmented blade-style trap . . . 26
3.1.1 Blade-style trap . . . 26
3.1.2 Confining potentials . . . 28
3.1.3 Freedom over the confining potential . . . 30
3.1.4 Blade conditioning . . . 34
3.2 Electronics . . . 35
3.2.1 Electronics targets . . . 35
3.2.2 Resonator for radio-frequency amplification . . . 36
3.2.3 Printed circuit board for mixing . . . 39
3.2.4 DC control software . . . 43
3.3 RF phase errors in the blade trap . . . 45

3.3.1 RF phase error - intrinsic micromotion . . . 46
3.3.2 RF phase error - excess micromotion . . . 46
3.4 Chapter conclusion . . . 47

**4 Trapping $^{171}Yb^{+}$ in a blade-style trap 50**
4.1 Addressing the ions . . . 50
4.1.1 Laser light delivery . . . 50
4.1.2 Control system . . . 52
4.2 First ion data . . . 53
4.2.1 Microwave Rabi . . . 53
4.2.2 Ramsey scans . . . 54
4.2.3 State preparation . . . 58
4.3 Chapter conclusion . . . 59

**5 Micromotion sensing with 935 nm repump 60**
5.1 Probing micromotion with a repump transition . . . 60
5.1.1 Micromotion detection scheme . . . 60
5.1.2 Experimental sequence . . . 63
5.1.3 Probing micromotion from 3 directions . . . 65
5.2 Micromotion data . . . 67
5.2.1 Minimizing micromotion . . . 67
5.2.2 Radial micromotion compensation . . . 70
5.2.3 Micromotion along a long chain of ions . . . 72
5.3 Chapter conclusion . . . 75

**6 Conclusion and outlook 77**

**References 80**

# List of Figures


2.1 Linear Paul trap diagram . . . . . 8
2.2 Radial comparison of pseudopotential and instantaneous potential . . . . . 11
2.3 Stray Electric field effects causing excess micromotion . . . . . 14
2.4 Single ion trajectory subject to excess micromotion . . . . . 15
2.5 Limitation to Doppler cooling from large micromotion . . . . . 18
2.6 $^{171}Yb^{+}$ energy level diagram . . . . . 21
2.7 $^{171}Yb^{+}$ state preparation and measurement for ground-state hyperfine qubit 23

3.1 Multi-segmented blade trap details . . . . . 27
3.2 Electrode naming convention for the blades . . . . . 29
3.3 Axial trap frequency in terms of axial confining voltages . . . . . 31
3.4 Manipulation of the confining potential in a multi-segmented blade trap . . 33
3.5 Helical resonator for RF amplification . . . . . 38
3.6 Measurement of the resonator quality factor . . . . . 39
3.7 Printed circuit board for signal mixing in the blade trap . . . . . 40
3.8 Mixing board integration in the system . . . . . 43
3.9 Control interface for the direct current on the electrodes . . . . . 45
3.10 Intrinsic micromotion in terms of RF phase error . . . . . 48
3.11 Excess micromotion in terms of RF phase error . . . . . 49

4.1 Laser light delivery in the blade trap . . . . . 51

4.2 Linear chain of 25 $^{171}Yb^{+}$ . . . . . 52
4.3 Stack around our control system . . . . . 53
4.4 Microwave Rabi flopping . . . . . 54
4.5 Coherence time measurements . . . . . 56
4.6 State preparation histogram . . . . . 58

5.1 Atomic physics behind probing micromotion with a repump transition . . . 62
5.2 Experimental sequence for probing micromotion . . . . . 64
5.3 Distribution of the 935 nm light between optical in-fiber components . . . 65
5.4 Cavity trace of the modulated 935 nm light . . . . . 66
5.5 Delivery of 935 nm light to the vacuum chamber . . . . . 68
5.6 Micromotion scans at the DC null . . . . . 69
5.7 Minimization of micromotion in both radial directions . . . . . 71
5.8 Micromotion at the edge of a long chain of ions . . . . . 73
5.9 Micromotion when a large stray field is present . . . . . 75

# List of Tables

2.1 Oscillatory motion breakdown in a confining potential . . . . . 14

3.1 Loading budget of the helical resonator . . . . . 38

4.1 Artiq distribution for experiments . . . . . 52
4.2 Fit parameters for Figure 4.5 . . . . . 55

5.1 935 nm beams for micromotion scans . . . . . 67

# List of Abbreviations

**AC** Alternating Current 7

**AOM** Acousto Optical Modulator 52

**DAC** Digital to Analog Converter 52

**DC** Direct Current 7

**DDS** Direct Digital Synthesizers 52

**ECDL** External Cavity Laser Diode 50

**EIT** Electromagnetically Induced Transparency 22

**EOM** Electro Optical Modulator 20

**FPGA** Field Programmable Gate Array 52

**FSR** Free Spectral Range 66

**FWHM** Full Width Half-Maximum 36

**GUI** Graphical User Interface 43

**IR** Infrared 35

**LCR** Inductor Capacitor Resistor 36

**LO** Local Oscillator 57

**MEMS** Micro-Electro-Mechanical Systems 64

**NA** Numerical Aperture 28

**PCB** Printed Circuit Board 34

**PCF** Photonic Crystal Fiber 66

**PMT** Photo-Multiplier Tube 22

**RF** Radio-Frequency 17

**RMS** Root Mean Square 41

**TTL** Transistor-Transistor Logic 52

**VVA** Variable Voltage Attenuators 64

# Chapter 1

# Introduction

## 1.1 Working with trapped ions

### 1.1.1 Why trap ions?

While some might give you a very broad explanation about the implications of a fully error corrected quantum computer, I believe that we remain far away from any of these sought after application such as factoring large primes. Working in a quantum computing lab is a very eye-opening experience in realizing the complexity and the infrastructure required for the most fundamental control over multiple quantum states. In essence, the trapped ion platform passes all of the DiVincenzo's criteria with flying colors from its qubits coherence time exceeding 1 hour [1], single qubit gates reaching infidelities of $10^{-7}$ [2], two qubit gates reaching infidelities of $10^{-4}$ [3] and $10^{-5}$ infidelities in state preparation and measurement [4]. Additionally, many great techniques have been introduce for scaling up ion traps with the quantum charge-coupled device architecture [5] and integrated photonics in trapped ion surface traps [6]. The remaining challenges are largely related to engineering a large scale system, while maintaining good overall fidelities.

Regardless, groundbreaking science has come out of current state-of-the-art trapped ion testbeds. A few of my favorite recent publications from the trapped ion community include:

- Observation of string-breaking dynamics in a quantum simulator [7]
- Hamiltonian learning for 300 trapped ion qubits with long-range couplings [8]

- Trapped-ion quantum simulation of electron transfer models with tunable dissipation [9]
- Distributed quantum computing across an optical network link [10]
- Multi-site integrated optical addressing of trapped ions [11]

What makes the trapped ion platform so remarkable is its wide range of implications in other fields besides quantum information science. Ranging from quantum chemistry simulations to high-energy particle physics modeling, many classically intractable problems can be mapped onto spin qubits encoded in the energy levels of trapped ions. The all-to-all connectivity of a collection of trapped ions enables simple mediation of entanglement. Despite my earlier critique of the state of these quantum devices, current quantum simulators *presently* have the capability of outperforming classical models, and answering fundamental physics questions. That's why we trap ions.

The quantum simulator discussed in this work is designed to eventually perform large scale quantum simulations with chains of up to[1] 30 $^{171}Yb^{+}$ ions. Some of its exciting features that are currently in the design phase include: dual acousto-optical deflectors for individual addressing, mid circuit measurement and resets, and fast mid-circuit state detection.

### 1.1.2 Characteristics of a good ion trap

To build a quantum simulator capable of large-scale simulations similar to the ones listed above, many fundamental characteristics of the ion trap itself need to check a few boxes. Ignoring any other engineering challenges, a good large-scale quantum simulator with trapped ions must have:

1. Low Micromotion in all three spatial directions,
2. Low Heating Rates,
3. A Good Vacuum with low background pressure.

[1] But not limited to 30 ions. This apparatus can hold many more than 30 ions, but challenges arise when starting to exceed 30 ions.

This thesis will primarily focus on demonstrating my efforts in studying and minimizing micromotion in a multi-segmented blade-style trap which will eventually be used for large-scale quantum simulations. This particular work is important because of the necessity for low micromotion during quantum simulation experiments. As will be discussed, it limits computational time, decreases gate fidelity and directly causes heating of the motional modes. While I will not present data on the heating rate, this work directly contributes to reducing the heating rate in the blade-style trap, therefore addressing the second point of the fundamentals of a good ion trap for quantum simulation.

Additionally, fast quantum logic gates require a high motional secular frequency. The work presented will present my efforts of designing the electronics required to obtain large secular frequencies in the blade-style trap. Our novel approach of using a balanced drive helical resonator and completely out-of-vacuum electronics to drive the oscillating signals in the trap will be presented.

The work presented in the text demonstrates our efforts in designing electronics to reach high secular frequencies in a blade-style ion trap, in addition to the characterization and minimization of micromotion in a blade-style trap. I demonstrate a completely out-of-vacuum approach for electronics which facilitates the prototyping to electronic design for the blade trap. Additionally, I demonstrate the micromotion measured in our blade-style trap. The measurements demonstrate that the micromotion levels without any compensation are inherently low, pointing towards the fact that the blades are well aligned, and our design of the blade trap contradicts the fear of bad micromotion in hand-assembled blade traps. The novelty of the work comes from the design of the electronics and the inherently low micromotion reached in a hand-assembled blade trap.

### 1.1.3 Literature review - micromotion

Since micromotion is such a well known issue in ion traps, the subject has been extensively studied and its compensation implemented in many ion trap architectures. A complete overview of micromotion was first introduced in 1998 by Berkland *et al.* [12]. Many methods have been introduced since to quantify micromotion and then reduce it. Direct probing of micromotion can be done with the photon correlation method [12] or by performing direct sideband spectroscopy [13, 14]. While these methods do provide a way to minimize micromotion, better and more precise methods have since been introduced because of the drastic effect of micromotion on atomic clocks. These include sideband spectroscopy using phase modulated light [15], amplitude modulation of the radio frequency drive [16] and even implementation of machine learning to augment the capability of current sensing techniques [17].

In terms of reaching high secular trap frequencies, blade traps inherently have this capability because of the proximity of the blades to the ion location. Many hand-assembled blade traps are currently used for quantum simulations [18, 19, 20], although none of these employ a balanced (or sometimes called symmetric) radio frequency drive. While a balanced radio frequency drive has been used in other trap geometries, this work presents the advantages for a blade-style trap in necessitating lower voltages to reach secular frequencies up to 5 MHz. The 5 MHz secular frequency target is important in quadrupole ion traps to decrease motional mode spectral crowding, and speed up quantum logic gates. Although varying in geometry, exciting work to reach high secular frequencies has been achieved in near-quadrupole 3 dimensional micro-fabricated traps [21] and monolithic blade traps [22, 23]. These techniques do suffer from imperfections as they micro-fabricate 3 dimensional structures, while our blade-style trap relies on 2 dimensional micro-fabrication, followed by hand assembly.

## 1.2 Contributions

This work was possible due to the team that worked on the blade-style trap system together. While I present much of the work that I completed in designing, assembling and characterizing electronics to then compensate micromotion, many other graduate and undergraduate students played an important role in facilitating the work.

Three graduate students primarily worked on designing and assembling the vacuum chamber and the blade trap itself. Sainath Motlakunta worked on the computer aided design of the system, and the assembly process of the chamber. Nikhil Kotibhaskar worked on the assembly of the chamber and on optimizing the vacuum system. Both of them also worked on simulations of the trap potentials. Lewis Hahn helped with the assembly of the chamber.

In terms of current graduate students, everybody worked on the same experiment, but had their own respective projects. Lewis Hahn worked on the imaging system, and built lots of the laboratory infrastructure from optics table enclosure to setting up monitoring sensors around the lab. He also worked with me in setting up the control system with the help of Mahmood Sabooni and Mahmoud Badawy. Shilpa Mahato designed the microwave system, and helped install and setup some of the lasers used in the lab. Sakshee Samir Patil worked on the delivery of many incoherent light sources to the chamber, and also helped in setting up lasers. All of this work was important for me to eventually probe micromotion in the blade trap. Further detailed contributions will be listed in individual chapters.

## 1.3 Outline

Below is an outline of the thesis contents:

- **Chapter 2** will discuss some relevant background. This will include ion dynamics, an introduction to micromotion and simple ion trapping techniques for experiments.
- **Chapter 3** will introduce the multi-segmented blade-style ion trap. Additionally, it will include the electronics I designed to generate the confinement, and a quick discussion about the effects of RF phase errors between electrodes.
- **Chapter 4** will present some of the preliminary data that was taken during my time. It will present some phase coherence time measurements, a chain of many ions and some system characterizations.
- **Chapter 5** will present the bulk of my work about probing micromotion in the blade-style trap. It will present the technique used, and discuss the results observed from these micromotion scans.
- **Chapter 6** will summarize the results of the thesis.

# Chapter 2

# Trapped ion dynamics and fundamentals

In this chapter, I will discuss some of the fundamentals for trapping an ion. Later chapters' results will rely on the principles detailed here. Firstly, I will go over the derivation of the fields confining a charged particle within a linear Paul trap. I will then provide the steps to obtain the equations of motion of an ion within an ion trap. From this point on, I will introduce the concept of micromotion in an ion trap, and detail the various types of micromotion. Secondly, I will introduce some fundamentals for running experiments with an ion trap system.

## 2.1 The linear Paul trap

The first proposal to confine a charged particle using electromagnetic fields emerged in the 1950s, proposed by Wolfgang Paul [24]. In the following years, he introduced the concept of a quadrupole trap to confine charged particles. This proposal later earned him a Nobel Prize in 1989, and thus was born the linear Paul trap [25].

### 2.1.1 Confining a charged particle

To effectively confine a charged particle in space using electromagnetic fields, is it necessary to have a component of the electromagnetic field to be oscillating over time. This concept follows Earnshaw's Theorem, which states that due to the Laplace equation ($\nabla \cdot E = \nabla^2 \phi =$

0), it is not possible to generate a stable and local equilibrium point for a charged particle to reside solely using static electric fields. To meet the condition where a charged particle resides at a stable minima within effective confinement, one must utilize an oscillating electric field to generate a saddle point within the electromagnetic field. Time-averaged over fast oscillations, the rotating saddle potential yields an effective minima where the charged particle resides, thereby *trapping* the charged particle in space.

The most fundamental of such traps is called the linear Paul trap. This sort of trap is called a quadrupole trap, because the confinement for two of the three spatial directions is done with an oscillating electric field. This type of ion trap consist of four rod electrodes carrying an Alternating Current (AC) signal and two needle electrodes carrying a Direct Current (DC) signal. Combined, these yield an effective trapping potential when averaged over time.

### 2.1.2 Confining electric fields

The following derivation of the confining electric fields will closely follow the one described by Berkland *et al* [12].

To generate an ideal saddle potential, one would require four infinitely long hyperbolic electrodes. Due to fabrication complications and limited optical access, these are typically not fabricated. A close approximation is to use four rods, which near the geometric center between all four rods, the potential is given by

$$\phi_{rods}(x, y) = \frac{\eta V_{rf}}{2R_0^2}(x^2 - y^2)\cos(\Omega_{rf}t). \tag{2.1}$$

To generate this potential, the voltage $V_{rf}$ oscillating at a frequency $\Omega_{rf}$ is applied $\pi$ out of phase on opposing rods spaced $2R_0$ away from each other as shown in Figure 2.1. The fudge factor $\eta$ emerges from the divergence of hyperbolic geometry from the rods, where $\eta = 1$ would indicate a perfect hyperbolic geometry of the electrodes. Typically, a linear Paul trap has a radial fudge factor $0.1 < \eta < 0.9$. This potential confines the charged particle in the *radial* plane.

To generate the *axial* confinement, static potentials are applied on cap electrodes. Near the geometrical center of the trap, the potential can be approximated by

$$\phi_{cap}(x, y, z) = \frac{\kappa V_z}{Z_0^2}[z^2 - \frac{1}{2}(x^2 + y^2)]. \tag{2.2}$$

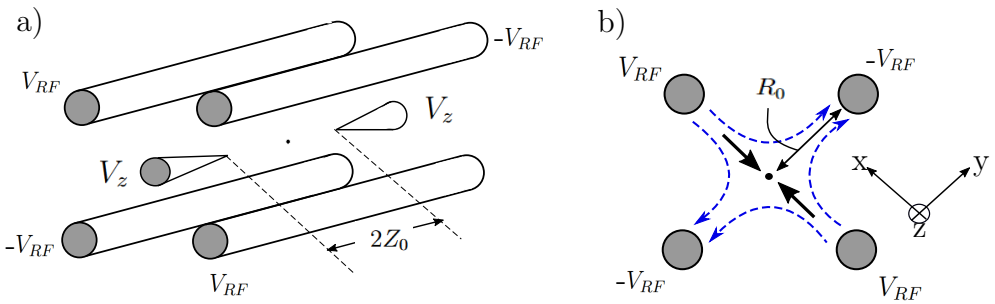



Figure 2.1: Diagram of standard Paul trap. a) Display of the 3 dimensional geometry of the quadrupole trap. b) Cross section in the radial plane. Special thanks to Ali Mustafa Khatai for sharing a schematic from this thesis and allowing me to modify it.

where $V_z$ is the cap voltage, $Z_0$ is the distance between the cap face and the geometric center of the trap and $\kappa$ is once again a geometric factor for the cap electrodes. Because of the divergence from hyperbolic geometry in the axial confinement, the axial fudge factor is typically smaller $\kappa < 0.5$.

Taking the gradient of the total potential $\nabla(\phi_{rods} + \phi_{cap}) = -\mathbf{E}$ yields the electric field

$$\mathbf{E}(x, y, z, t) = -\eta V_{rf}\left(\frac{x\hat{x} - y\hat{y}}{R_0^2}\right)\cos(\Omega_{rf}t) - \frac{\kappa V_z}{Z_0^2}(2z\hat{z} - x\hat{x} - y\hat{y}). \tag{2.3}$$

Figure 2.1 presents a schematic of the Paul trap treated in this specific example. The four rods create radial confinement in the XY plane, and the needles create the axial confinement in the Z direction.

### 2.1.3 Pseudopotential

From the electric field given in Equation 2.3, an intuitive description of the confinement using an oscillating electric field can be derived. Such a confining potential is called the *pseudopotential*. I will follow the derivation given in Steven Matthew Olmschenk's PhD thesis [26].

Constraining ourselves to a single dimension ($\hat{x}$), the effect of an oscillating electric field on a charged particle yields a time-averaged force. Consider a charged particle of mass $m$ and charge $e$ confined between two plates forming a capacitor with distance $2d$ with time dependent voltage $V_{rf}\cos(\Omega_{rf}t)$. Given that these plates are perpendicular along $\hat{x}$, the force is given by

$$\begin{aligned} F &= m\ddot{x} = eE(x,t) \\ F &= eE_0(x)\cos(\Omega_{rf}t) \end{aligned} \tag{2.4}$$

where $E_0 = V_{rf}/2d$. I can then integrate to find the position of the particle as

$$x(t) = x_0 - \frac{eE_0(x)}{m\Omega_{rf}^2}\cos(\Omega_{rf}t), \tag{2.5}$$

given an initial position $x_0$ and no initial velocity. The time-averaged force of Equation 2.4 is null. I now consider the field to be inhomogeneous along $\hat{x}$ as is the case in an ion trap (along any direction), *i.e.* $E_0(x) \neq E_0(x_0)$. Applying a first-order Taylor expansion around $x_0$, the electric field takes the form

$$\begin{aligned} E_0(x) &\approx E_0(x_0) + \left.\frac{\partial E_0(x)}{\partial x}\right|_{x_0}(x - x_0) \\ &\approx E_0(x_0) - \frac{\partial E_0(x_0)}{\partial x_0}\left(\frac{eE_0(x_0)}{m\Omega_{rf}^2}\cos(\Omega_{rf}t)\right). \end{aligned} \tag{2.6}$$

Here I considered that the derivative of $E_0(x_0)$ is smaller that $E_0(x_0)$ itself to simplify Equation 2.6. Equation 2.5 was also substituted in. I can now rewrite the force felt by the charge particle within the inhomogeneous capacitor by substituting Equation 2.6 into Equation 2.4

$$F(t) \approx eE_0(x_0)\cos(\Omega_{rf}t) - e\frac{\partial E_0(x_0)}{\partial x_0}\left(\frac{eE_0(x_0)}{m\Omega_{rf}^2}\cos^2(\Omega_{rf}t)\right). \tag{2.7}$$

Now, time-averaging this force sets $\langle\cos(\Omega_{rf}t)\rangle = 0, \langle\cos^2(\Omega_{rf}t)\rangle = 1/2$, and our time-averaged force on the charged particle takes the form

$$\begin{aligned} \langle F\rangle &\approx -\frac{e^2}{2m\Omega_{rf}^2}\frac{\partial E_0(x_0)}{\partial x_0}E_0(x_0) \\ &\approx -e\frac{\partial \phi_{pseudo}}{\partial x_0} \end{aligned} \tag{2.8}$$

where the *pseudopotential* was introduced as

$$\phi_{pseudo} = \frac{eE_0^2}{4m\Omega_{rf}^2}. \tag{2.9}$$

This can also be expanded to all three spatial directions

$$\phi_{pseudo} = \frac{e|\mathbf{E}_0(x,y,z)|^2}{4m\Omega_{rf}^2}. \tag{2.10}$$

Although only serving as a first order approximation, the concept of deriving a pseudopotential in the radial plane of a linear Paul trap paints a nice picture as to why the charged particle over time remains effectively under confinement. A good visualization is to plot the potential at an instantaneous time t, as compared to the time-averaged effect of the oscillating potential. This is done in Figure 2.2 where the pseudopotential in Equation 2.11 and the instantaneous ($t = 0$) rods potential in Equation 2.1 is compared side-by-side.

Taking the electric field components generated by the rods in Equation 2.3, I can write its pseudopotential as

$$\phi_{pseudo} = \frac{e}{4m\Omega_{rf}^2}\frac{\eta^2 V_{rf}^2}{R_0^4}(x^2+y^2). \tag{2.11}$$

By introducing a radial angular frequency $\omega_r = \frac{e\eta V_{rf}}{\sqrt{2}m\Omega_{rf}R_0^2}$, the pseudopotential can be rewritten as

$$e\phi_{pseudo} = \frac{1}{2}m\omega_r^2(x^2+y^2). \tag{2.12}$$

Therefore, the pseudopotential takes the form of a 2-dimensional harmonic oscillator. A more general derivation will be detailed in the following subsection.

### 2.1.4 Ion motion

To begin deriving the motion under confinement, I consider a particle of mass $m$ and charge $e$ given its position $\mathbf{u} = u_x\hat{x} + u_y\hat{y} + u_z\hat{z}$, subject to a force in the confining electric field

$$m\ddot{\mathbf{u}} = e\mathbf{E}(\mathbf{u}, t), \tag{2.13}$$

Given the electric field previously found in Equation 2.3, I can get the motion along all 3 directions which takes the form

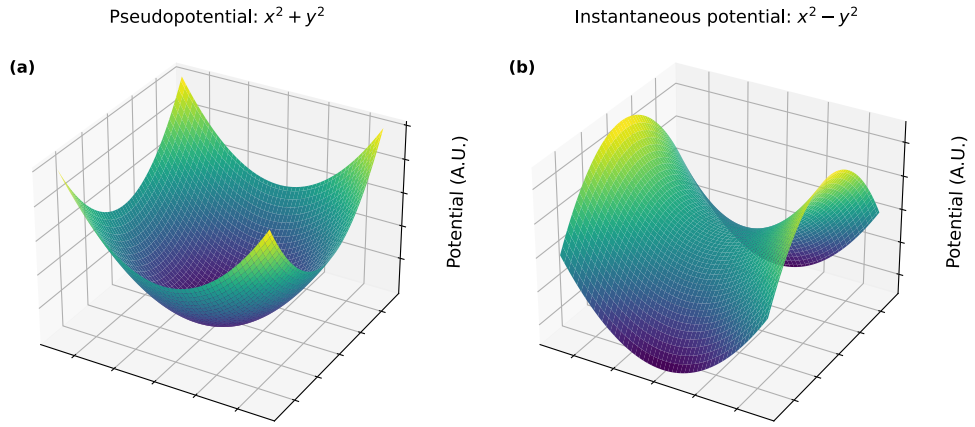



Figure 2.2: Comparison of pseudopotential and instantaneous potentials in the radial plane. a) Display of the time-averaged pseudopotential. b) Potential seen by the ion at some instantaneous time $t$.

$$\ddot{x} + \frac{e}{m}\left[\frac{\eta V_{rf}}{R_0^2}\cos(\Omega_{rf}t) - \frac{\kappa V_z}{Z_0^2}\right]x = 0, \tag{2.14}$$

$$\ddot{y} + \frac{e}{m}\left[\frac{-\eta V_{rf}}{R_0^2}\cos(\Omega_{rf}t) - \frac{\kappa V_z}{Z_0^2}\right]y = 0, \tag{2.15}$$

$$\ddot{z} + \frac{e}{m}\left[\frac{2\kappa V_z}{Z_0^2}\right]z = 0. \tag{2.16}$$

The motion of the ion is now separated into three ordinary differential equations along all 3 spatial directions. I can substitute $\Omega_{rf}t = 2\tau$, $q_x = -q_y = \frac{2\eta e V_{rf}}{m R_0^2 \Omega_{rf}^2}$, $q_z = 0$ and $a_x = a_y = -\frac{1}{2}a_z = -\frac{4\kappa e V_z}{m Z_0^2 \Omega_{rf}^2}$ to obtain three equations that take the form of the Mathieu Equation

$$\ddot{u_i} + [2q_i\cos(2\tau) + a_i]\frac{\Omega_{rf}^2}{4}u_i = 0 \tag{2.17}$$

where $\dot{u_i} = \frac{\partial u_i}{\partial \tau}$ and $i$ denotes one of the three spatial directions such that $\hat{u}_x = \hat{x}, \hat{u}_y = \hat{y}, \hat{u}_z = \hat{z}$.

The Mathieu Equation presented above in Equation 2.17 has a well known solution given some constrains on the parameters $q_i$ and $a_i$. The typical operating scenario for a

Paul trap is to consider $|q_i| \ll 1$ and $|a_i| \ll 1$ because of constraints on electrode distance and applicable voltage. Under these assumptions, the first order solution to the Mathieu Equation given in Equation 2.17 is

$$u_i(t) \approx u_{1i} \cos(\omega_i t + \varphi_{Si}) \left[1 + \frac{q_i}{2} \cos(\Omega_{rf} t)\right]. \tag{2.18}$$

Above, I introduced the secular frequency which is given by

$$\omega_i \cong \frac{1}{2}\Omega_{rf}\sqrt{a_i + \frac{1}{2}q_i^2}, \tag{2.19}$$

and a few other parameters including $\varphi_{Si}$ which depends on the ions initial velocity and position, and $u_{1i}$ which represents the amplitude of the secular motion, dictated by the temperature of the ion. By approximating $a_i \ll q_i$ for $i \in x, y$, I simplify $\omega_{x,y} \approx \frac{1}{2\sqrt{2}}\Omega_{rf}|q_{x,y}|$ and $\omega_r$ derived in the pseudopotential section given in Equation 2.12 is obtained.

Equation 2.18 describes the motion of the ion in all three spatial directions under the confinement of the electromagnetic fields. As described above in Section 2.1.1, the charged particle is effectively confined, although continuously in motion. From Equation 2.18, the two components of the motion are commonly coined as the *secular motion* oscillating at the secular frequency $\omega_i$ and the *intrinsic micromotion* which oscillates at frequencies $\Omega_{rf} \pm \omega_i$.

## 2.2 Micromotion

This section will introduce the concept of micromotion, and how to quantify it.

### 2.2.1 Micromotion in a quadrupole trap

In the section above, I described the motion that a charged particle undergoes within the confining potentials of a linear Paul trap. One important detail that was exempt from the derivation presented is that the charged particle may also be subject to a uniform static electric field at its confinement location. This is a relevant scenario to study because of potential electrode misalignment, which would yield a static and uniform electric field at the confinement location. For example, this was studied for quadrupole blade-style traps in Pei Jiang Low's M.Sc. thesis [27].

Let's consider that there is a uniform static electric field $\mathbf{E}_{dc}$ at the confinement location which applies a force on the charged particle. I can rewrite the Mathieu Equation given in Equation 2.17 as

$$\ddot{u_i} + [2q_i \cos(2\tau) + a_i]\frac{\Omega_{rf}^2}{4}u_i = \frac{q\mathbf{E}_{dc} \cdot \hat{u}_i}{m}. \tag{2.20}$$

The equation of motion then takes the new form

$$u_i(t) \approx [u_{0i} + u_{1i}\cos(\omega_i t + \varphi_{Si})]\left[1 + \frac{q_i}{2}\cos(\Omega_{rf}t)\right] \tag{2.21}$$

with

$$u_{0i} \cong \frac{4q\mathbf{E}_{dc} \cdot \hat{u}_i}{m(a_i + \frac{1}{2}q_i^2)\Omega_{rf}^2} \cong \frac{q\mathbf{E}_{dc} \cdot \hat{u}_i}{m\omega_i^2}. \tag{2.22}$$

I simplified by substituting Equation 2.19. In comparison with Equation 2.18, Equation 2.21 has two extra terms. The first one is a simple displacement of the motion by $u_{0i}$, and the second is a term oscillating at $\Omega_{rf}$ which I will call *excess micromotion*. Excess micromotion can be nulled by eliminating the stray uniform field $\mathbf{E}_{dc}$ at the center of the pseudopotential. Figure 2.3 displays how the strength of $\mathbf{E}_{dc}$ (given by the slope of the orange line) displaces the center point of the motion, causing excess micromotion.

The three principle components of the oscillatory motion are the secular motion, intrinsic micromotion and excess micromotion. All of these behave particularly differently and are described in Table 2.1 below.

A good visualization of all these oscillatory components arises when simulating the trajectory of a single trapped ion given the electric fields generated by all electrodes. This is done by solving the ordinary differential equation step by step. By varying the voltage over time and tracking the acceleration, velocity and position of the ion, I can extract a three dimensional trajectory. As a byproduct, a fast Fourier transform of the trajectory along one axis yields a spectrum with peaks at the frequencies of these oscillatory components. The script used to simulated was adapted from Nikhil Kotibhaskar's thesis [29]. See Figure 2.4 for an example trajectory.

### 2.2.2 Quantifying micromotion

To compare micromotion between different trap architectures or how it scales within a trap, it is useful to have metrics to quantify the micromotion. There are a few standard

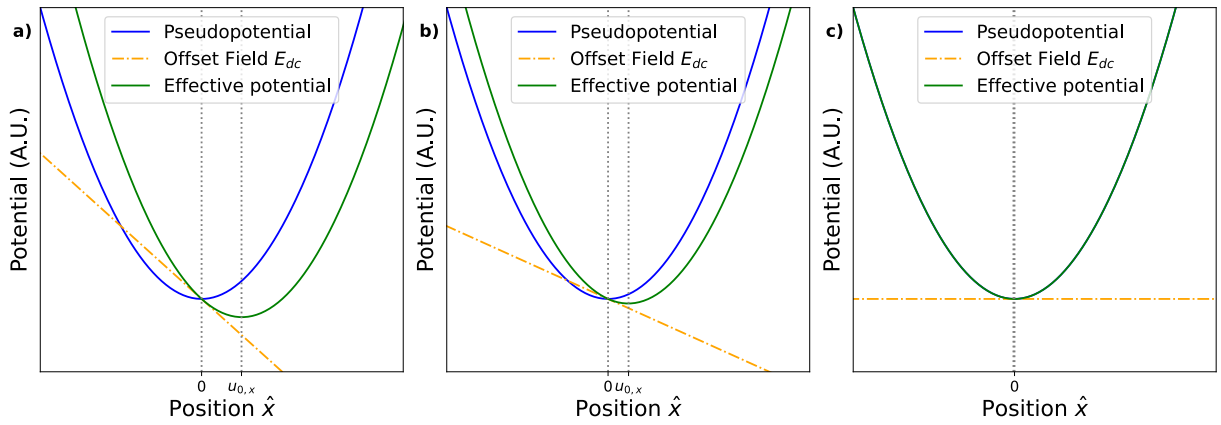



Figure 2.3: Displacement of $u_{0,x}$ as the offset electric field $\mathbf{E}_{dc}$ along $\hat{x}$ increases. Slope of the orange line represents the amplitude of $\mathbf{E}_{dc}$. a) Large uncompensated $\mathbf{E}_{dc}$, b) Smaller uncompensated $\mathbf{E}_{dc}$, c) Compensated $\mathbf{E}_{dc}$, therefore no excess micromotion. Figure idea adapted from [28].

| | **Secular Motion** | **Intrinsic Micromotion** | **Excess Micromotion** |
|---|---|---|---|
| **Amplitude** | $u_{1i}$ | $\frac{u_{1i}q_i}{2}$ | $\frac{u_{0i}q_i}{2} \propto \mathbf{E_{dc}} \cdot \hat{u_i}$ |
| **Angular Frequency** | $\omega_i$ | $\Omega_{rf} \pm \omega_i$ | $\Omega_{rf}$ |
| **Notes** | Principal component of motion | Byproduct of oscillating fields, fixed and intrinsic | Byproduct of static uniform electric fields, can be compensated and nulled |

Table 2.1: Oscillatory motion breakdown in a confining potential

ways to quantify the micromotion, and this subsection will discuss the relevant ones.

**Quantification**

It is useful to quantify micromotion in order to minimize it and compare its level be-

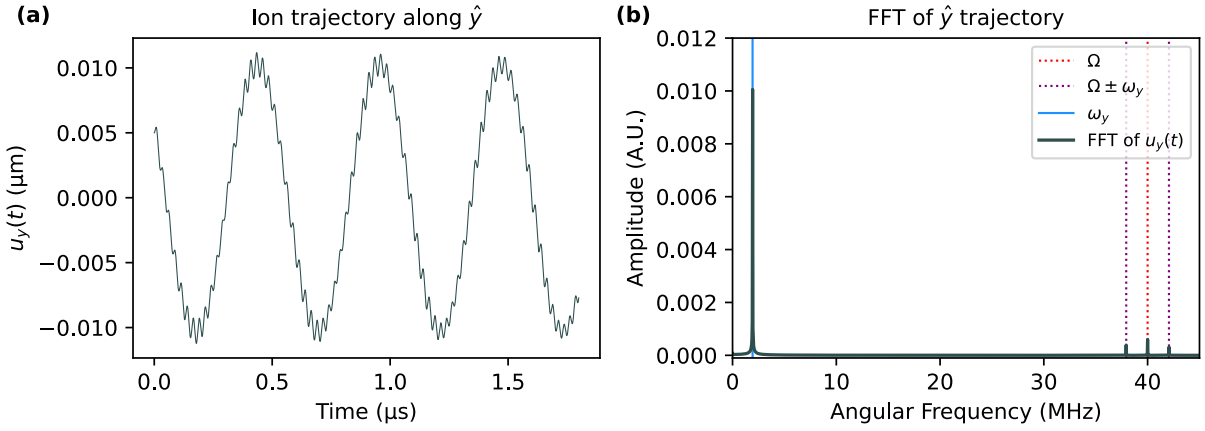



Figure 2.4: Single ion trajectory along $\hat{y}$ within a blade-style trap with a drive frequency of $\Omega_{rf}/2\pi = 40$ MHz and secular frequency $\omega_y$. a) Trajectory under the influence of a stray electric field inducing micromotion, which can be seen as the fast oscillations. b) Fast Fourier Transform (FFT) of the trajectory in (a).

tween different traps. Micromotion is typically measured along individual spatial directions in order to characterize it along all three spatial directions. As described by Keller *et al.* [30], given an ion subject to excess micromotion with a velocity $\boldsymbol{v} = \boldsymbol{v}_{\mu m}\cos(\Omega_{rf}t)$, the first-order Doppler shift caused by this motion can be quantified as a laser phase modulation via the modulation index

$$\beta = \mathbf{k}\cdot\boldsymbol{v}_{\mu m}/\Omega_{rf}. \tag{2.23}$$

The k-vector $\mathbf{k}$ of the light determines the projection of the measurement on the micromotion. The notation $\beta_i$ could be used to describe micromotion along a single spatial direction where $\mathbf{k}$ is along a trap axis ($\mathbf{k} \parallel \hat{i}$). In the rest frame of the ion subject to excess micromotion, I can then write the laser field as

$$E(\omega) \propto J_0(\beta)\delta(\omega-\omega_L) + J_1(\beta)\left[\delta(\omega-\omega_L-\Omega_{rf}) + \delta(\omega-\omega_L+\Omega_{rf})\right] \tag{2.24}$$

where the laser frequency $\omega_L$ with k-vector $\mathbf{k}$ and the first-order Doppler shift through the Bessel functions $J_n(\beta)$ is introduced. Here I treated the ion as a filter for these specific frequencies, hence the introduction of the Dirac delta $\delta$ function.

The dimensionless modulation index $\beta$ and the micromotion velocity $\boldsymbol{v}_{\mu m}$ in m/s serve as good metrics for the micromotion. Another useful metric to quantify micromotion is to use

the displacement from the micromotion null, where micromotion is fully compensated. The distance from the null in a single spatial direction is given by $u_{0i}$ which was first introduced in Equation 2.22. The modulation index can be written in terms of the deviation from the micromotion null in the radial plane [12] such that

$$\beta = \frac{1}{2}\sum_{i\in x,y} k_i u_{0i} q_i \tag{2.25}$$

where $k_i$ is the laser k-vector projection along the direction $i$ and $q_i$ is the Mathieu $q$ parameter along $i$. By setting $\mathbf{k} = k_i$, it is possible to extract $u_{0i}$ and then using Equation 2.22 find the static electric field $\mathbf{E}_{dc}$ in V/m along some spatial direction $i$.

**Probing Micromotion Optically**

Because of the first-order Doppler shift presented above in Equation 2.23, sidebands at the excess micromotion frequency $\Omega_{rf}$ arise around resonances. Treating a simple two level system with levels $|a\rangle$ and $|b\rangle$, linewidth $\Gamma$ driven with laser light detuned $\Delta$ from the atomic resonance, the electric field interacting with the atom at the low intensity limit yields a steady state to solution to the optical Bloch equation [12] taking the form

$$\rho_{bb} \propto \sum_{n=-\infty}^{\infty} \frac{J_n^2(\beta_i)}{(\Delta - n\Omega_{rf})^2 + (\Gamma/2)^2}, \tag{2.26}$$

where $\rho_{bb}$ is the population in the upper state. The modulation index $\beta_i$ depends on the k-vector direction $\hat{i}$ of the light probing that resonance. To get an estimate of the micromotion along all 3 directions within the trap, sending light from 3 orthogonal directions can fully quantify $\beta$ along $\hat{x}, \hat{y}, \hat{z}$. For this sensing method to be useful, the condition $\Gamma \ll \Omega_{rf}$ needs to be met in order to have resolvable sidebands.

One method to find $\beta$ would be to sweep $\Delta$ and fit a spectrum to Equation 2.26. Instead, taking the amplitude of both the atomic resonance and its micromotion sidebands is sufficient since their amplitudes will be proportional to their Rabi frequencies. As such, from Equation 2.24, $\beta$ can be estimated as

$$\frac{\Omega_{\pm 1}}{\Omega_0} = \frac{J_1(\beta)}{J_0(\beta)} \approx \frac{\beta(\beta^2 - 8)}{4(\beta^2 - 4)} \tag{2.27}$$

where $\Omega_0(\Omega_{\pm 1})$ is the Rabi frequency of the carrier (micromotion sideband). The identity used above comes from the series expansion of the Bessel functions, and is valid for $\beta < 2$.

The other most common method for probing micromotion is to use the photon correlation method. This method works particularly well when one is restricted to probing micromotion on a transition with $\Gamma \gg \Omega_{rf}$ where the micromotion sidebands are not resolvable. For more details, see these references [30, 31]. Other methods using phase modulated light fields [15] and amplitude modulation of the trap drive [16] have recently come to light as great alternatives for minimizing excess micromotion.

### 2.2.3 Challenges associated with micromotion

As the bulk of my later thesis sections will focus on probing and minimizing micromotion in a blade-style trap, I will motivate why micromotion is detrimental during experiments.

**Doppler shifts**

As the ion is experiencing excess or intrinsic micromotion, it is now subject to Doppler shifts from the micromotion with respect to the amplitude of the micromotion. This first-order Doppler shift in turn causes spectral crowding near atomic resonances at $\pm$ the micromotion frequency components. The equation governing this first order Doppler shift of a Lorentzian was introduced in Equation 2.26.

Firstly, spectral crowding is problematic because it increases chances of off-resonantly driving micromotion and giving a momentum kick to the ion, which could disrupt its secular motion trajectory. Also, driving any optical transition blue-detuned, which could serve as a cooling operation, now has the increased chance of also off-resonantly driving the motional red sideband of the micromotion peaks. This decreases cooling efficiency.

Additionally, when driving a transition where the power-broadened natural linewidth is about or greater than the trap drive frequency ($\Gamma(I) \gtrsim \Omega_{rf}$), under sufficient micromotion is it possible to heat the ion while being blue detuned from the resonance. This was first observed by Blümel and DeVoe in the same year [32, 33]. An example of this phenomenon is displayed in Figure 2.5. For the same frequency, sufficient micromotion can cause heating over time when blue detuned from a resonance. In this example, I consider a closed cooling cycle on the $^2S_{1/2} \rightarrow {}^2P_{1/2}$ of the $^{171}\mathrm{Yb}^+$ ion at 369 nm with linewidth $\Gamma_{369}/2\pi = 19.6$ MHz and a trap drive frequency of $\Omega_{rf}/2\pi = 20$ MHz. This simple model plots Equation 2.26 for no micromotion, and then $\beta = 2.2$. The modulation of the Lorentzian lineshape from the first-order Doppler shift causes the typically optimal cooling frequency ($-\Gamma_{369}/2$) to be on a negative slope when $\beta = 2.2$, resulting in net heating over time.

**Motional heating**

More importantly, the presence of excess micromotion causes heating at any given moment because of the periodic driving from the AC Radio-Frequency (RF) fields. When the ion's

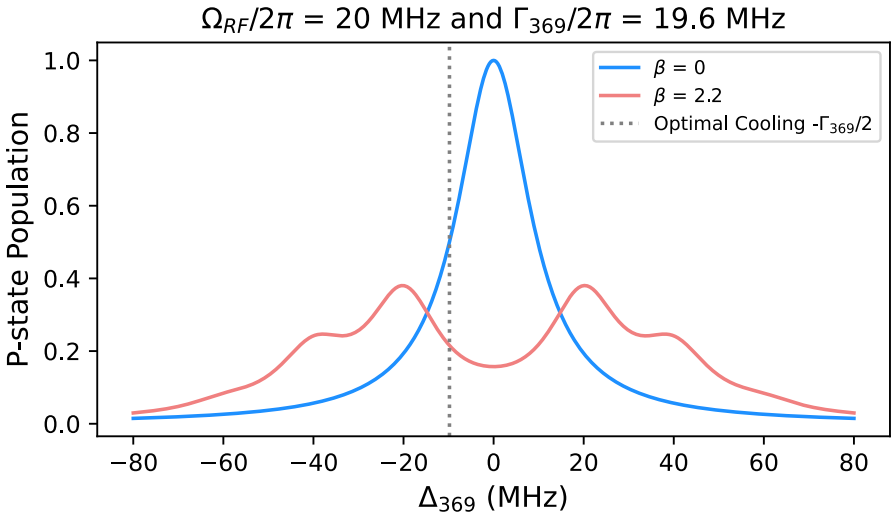



Figure 2.5: First-order Doppler shift effect during a cooling operation under the influence of large excess micromotion. Curves are obtained using Equation 2.26 and amplitude is chosen to normalize P-state population when $\beta = 0$. Dotted line shows optimal frequency of laser detuning when $\beta = 0$, and the sign of the slope at the intersection of the dotted line represents whether cooling or heating occurs. Positive slope represents cooling.

excess micromotion amplitude is high, the ion is spectrally exposed to the frequency of the RF fields, and the periodic driving increases the ion's kinetic energy over time. The increase in net energy from micromotion heating increases the phonon population $\overline{n}$.

A fundamental requirement for quantum experiments with trapped ions is to have the motional quanta of their phononic modes at or near[1] the motional ground state. Below is a non-exhaustive list as to why motional heating and non-zero phonon population is problematic in trapped ion quantum computing:

- Reduced computation time: Computing a digital circuit of depth $D$ can take a considerable amount of time on a trapped ion platform because of the $\tau \sim 100$ us [35] timescale for laser-driven two-qubit gates. Poor heating rates $\dot{\overline{n}}$ from uncompensated excess micromotion (which can easily reach the $\dot{\overline{n}} = 10^3$ quanta/s level) therefore limiting the computation time

- Exiting Lamb-Dicke Regime: As phonon population gets high, we quickly near the boundary of the Lamb-Dicke regime $\eta^2(2\overline{n}+1) \ll 1$. Here $\eta$ is the Lamb-Dicke parameter and it dictates the coupling between the ion's internal states and motional states. Near this limit, any interaction mediated with the ion's motional modes becomes worse as the higher-order contributions become non-negligible. This complicates motional excitation, sideband cooling and any process mediated through the motional modes.

- Decoherence of single qubit gates: For long ion chains, ions reside along the harmonic axial potential. Ions away from the axial null therefore experience a second order effect from the curvature of the potential which adds a term proportional to $z^2$ within the Rabi frequency. As shown by Cetina *et al.* [36], the decoherence of single qubit gates $\theta_{im}$ per mode $m$ and ion $i$ is proportional to the phonon number of mode $m$: $\theta_{im} \propto \overline{n}_m$.

- Amplified phase space trajectories: When performing multi-qubit interactions, they are mediated by the motional states [34]. A completed gate requires disentanglement of the spin and motion, and a common error for two-qubit gates is residual spin-motion entanglement. With nonzero phonon occupation, the amplitude of the phase space trajectory is larger, and any residual spin-phonon entanglement is amplified [37].

[1] Near because some quantum operations in trapped ions such as the Mølmer-Sørensen entangling gate [34] are independent of the phonon motional quanta $\overline{n}$, although significant challenges are faced when moving away from the motional ground state $\overline{n} = 0$.

## 2.3 Trapped ion physics

Here I will discuss some of the basics for experiments, and introduce our ion of choice, $^{171}Yb^{+}$.

### 2.3.1 Trapping an ion

Many things have to go right and fall into place to trap an ion. As detailed above, I first need to generate a confining potential with a stable solution to the trajectory for the ions. To get Ytterbium flowing through the confining potential, a current is applied to an atomic oven source, which is simply a small metal tube with two current leads.

With neutral ytterbium flowing through the trap, 399 nm light is first sent to excite one of the valence electrons from $(6s^2)\ ^1S_0$ to $(6s6p)\ ^1P_1$, and then either 355 nm or 369 nm is delivered for ionization, kicking the electron into continuum. As ytterbium has many naturally abundant isotopes, the frequency of the 399 nm light is used for isotope selection. Ionized $^{171}Yb^{+}$ is now flowing through the confining potentials, and with the aid of Doppler cooling [38], there is a small chance that an ion will get trapped.

Figure 2.6 displays the energy level diagram of $^{171}Yb^{+}$. This specific isotope is chosen for quantum computation purposes because of its simple state preparation and measurement, long lived $^2S_{1/2}$ hyperfine qubit states with first-order insensitivity to magnetic field and many other reasons. Our hyperfine qubit states are defined as

$$^2S_{1/2}\,|F=1, m_F=0\rangle = |1\rangle = |\uparrow\rangle \tag{2.28}$$

$$^2S_{1/2}\,|F=0\rangle = |0\rangle = |\downarrow\rangle \tag{2.29}$$

with $|1\rangle$ our bright state and $|0\rangle$ the dark state.

Doppler cooling is performed on the $^2S_{1/2} \rightarrow\ ^2P_{1/2}$ 369 nm transition. The 369 light is applied resonant to $^2S_{1/2}\,|F=1\rangle \rightarrow\ ^2S_{1/2}\,|F'=0\rangle$, and a 14.7 GHz Electro Optical Modulator (EOM) is used to remove population trapped in $^2S_{1/2}\,|F=0\rangle$. For efficient Doppler cooling, the 369 nm light must project on all 3 motional axis of the ion for cooling along all 3 spatial directions. Additionally, 935 nm light resonant to $^2D_{3/2}\,|F=1\rangle \rightarrow\ ^3[3/2]_{1/2}\,|F'=0\rangle$ passing through a 2.1 GHz EOM repumps populating back to the ground state because of the occasional $^2P_{1/2} \rightarrow\ ^2D_{3/2}$ decay, leaving the ion in the fairly long lived $^2D_{3/2}$ manifold with decay time of about 50 ms. Red-detuning the light by $\Delta_{369} = -\Gamma_{369}/2$ away from the resonance maximizes the efficiency of Doppler cooling,

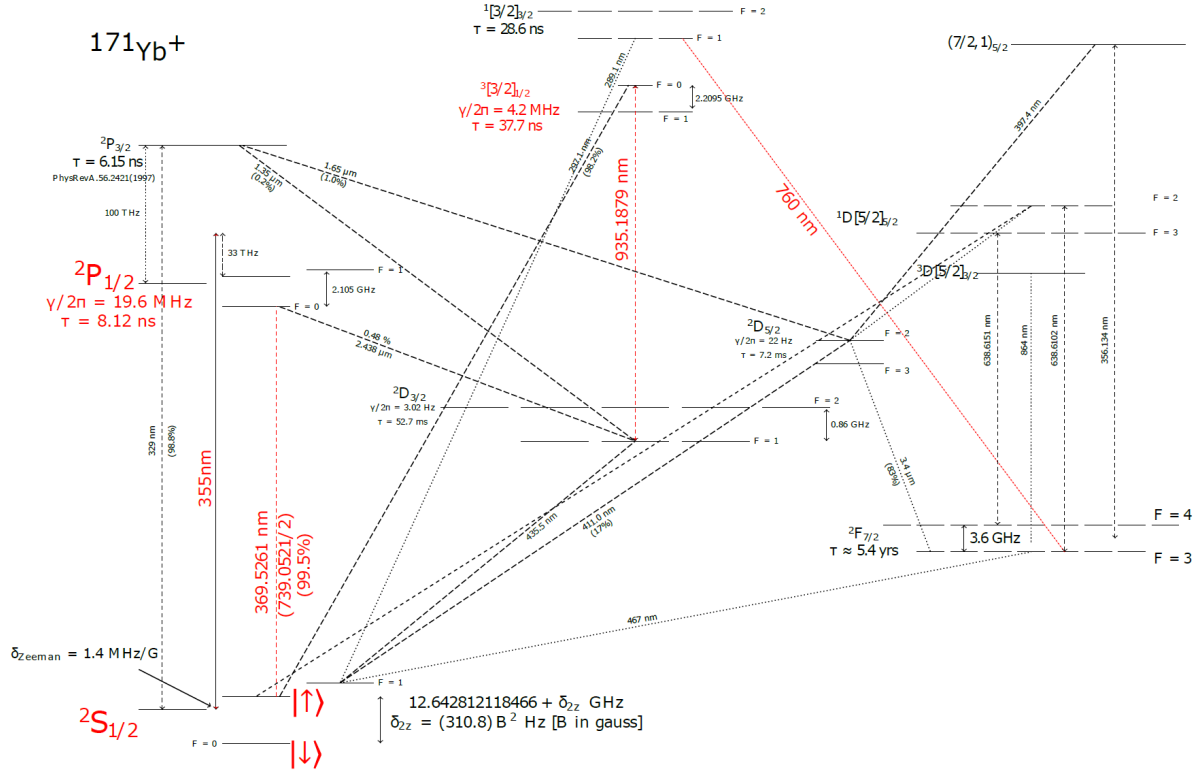



Figure 2.6: $^{171}Yb^{+}$ energy level diagram [39].

and over time reduces the motional quanta of the trapped ion to the Doppler cooling limit [40]. Since the $^2P_{1/2}$ has a lifetime of $\tau = 8.12$ ns, the Doppler cooling cycle to reach the Doppler cooling limit takes a few milliseconds at most. To reach the motional ground state of $\overline{n} = 0$, methods such as resolved sideband cooling [41] or Electromagnetically Induced Transparency (EIT) cooling [42] must be used.

### 2.3.2 State preparation and measurement

Once an ion is trapped and cooled to the Doppler cooling limit, its electronic states can be used as qubit states defined by Equations 2.29 and 2.28. State preparation and measurement are both done using the $^2S_{1/2} \rightarrow {}^2P_{1/2}$ transitions.

**State Preparation**: To complete a state preparation, all population must be driven to the dark state $^2S_{1/2}\,|F = 0\rangle$. Once again, 369 nm light is applied resonant to $^2S_{1/2}\,|F = 1\rangle \rightarrow {}^2P_{1/2}\,|F' = 0\rangle$, but now with a 2.1 GHz EOM to additionally drive $^2S_{1/2}\,|F = 1\rangle \rightarrow {}^2P_{1/2}\,|F' = 1\rangle$. Population is therefore constantly pumped out of $^2S_{1/2}\,|F = 1\rangle$ until trapped in the $^2S_{1/2}\,|F = 0\rangle$ state, which happens to be 2.1 GHz detuned from any 369 nm light. Because of the cycling $^2S_{1/2} \rightarrow {}^2P_{1/2}$ transition, 935 nm light with the same parameters as during Doppler cooling is necessary here. For $^{171}\mathrm{Yb}^+$, optical pumping typically takes about 10 $\mu$s to obtain a dark state with fidelity $\mathcal{F} > 99\%$. A display of the transitions driven and decays happening are displayed in Figure 2.7(a).

**Measurement - State Detection**: State detection is done by having 369 nm light resonant to only the $^2S_{1/2}\,|F = 1\rangle \rightarrow {}^2S_{1/2}\,|F' = 1\rangle$ transition. Because of the forbidden $\Delta F = \Delta m_F = 0$ transitions, this cycling transition will only be driven if the population started in the bright state $|\uparrow\rangle$. Population in $|\downarrow\rangle$ remains trapped as light is off-resonant to any of its possible $^2S_{1/2} \rightarrow {}^2P_{1/2}$ transitions. Once again, 935 nm light is applied with the same parameters. Light is them collected from the ion through an objective, and imaged onto a Photo-Multiplier Tube (PMT) or camera. Total photon collection can then distinguish the bright and dark states based off of a discriminator value. Figure 2.7(b) displays the measurement scheme.

### 2.3.3 Single qubit rotations

State preparation and measurement serve little purpose without any quantum logic to implement in between. The hyperfine qubit states in $^{171}\mathrm{Yb}^+$ are separated by about 12.6428 GHz. To drive single qubit gates, a microwave signal can directly couple both states, or

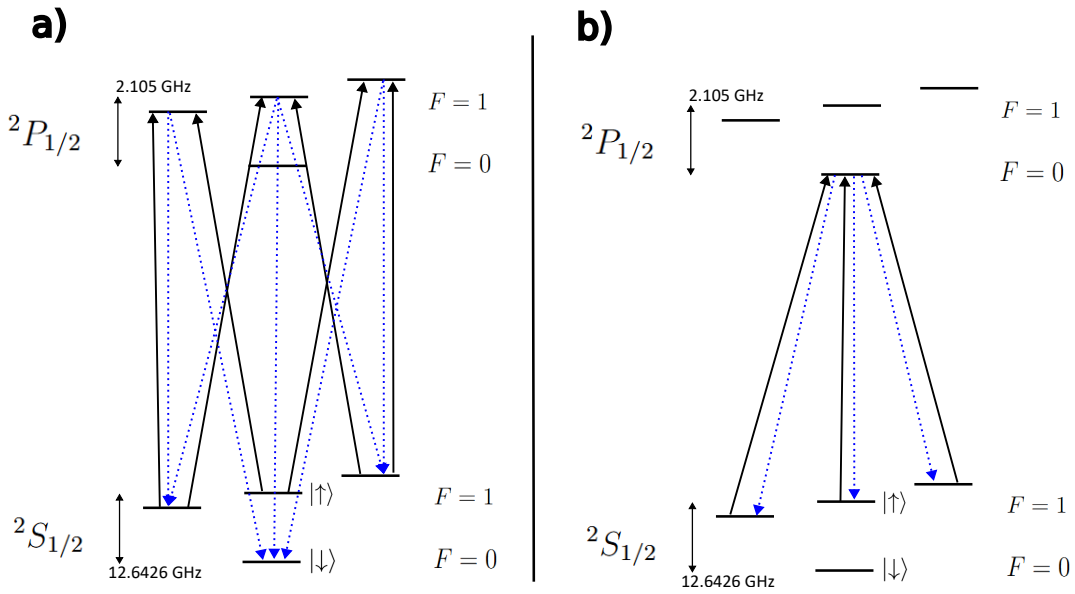



Figure 2.7: $^{171}Yb^+$ state preparation and measurement schemes. a) Light is displayed resonant to $^2S_{1/2}\,|F = 1\rangle \rightarrow {}^2P_{1/2}\,|F' = 1\rangle$, driving the population down to the $|\downarrow\rangle$. State is prepared in the dark state. b) Light is displayed resonant to $^2S_{1/2}\,|F = 1\rangle \rightarrow {}^2P_{1/2}\,|F' = 0\rangle$, driving a cycling transition for the bright state $|\uparrow\rangle$.

a two-photon process such as the stimulated Raman transition can drive the microwave transition through a beatnote.

In the light of this thesis, I will briefly introduce the microwave single qubit gate. A microwave horn is directed towards the ion's location, and applying the resonant hyperfine frequency to $|\downarrow\rangle_z \rightarrow |\uparrow\rangle_z$[2] can drive Rabi oscillations. The interaction Hamiltonian from the applied microwave signal of $\Omega_{rf}\cos(\omega_{hf}t+\phi)$ following a rotating wave approximation [43] is given by

$$\hat{\mathcal{H}}_{int} \approx \frac{\hbar}{2}\left(\Delta\hat{\sigma}_z + \Omega\hat{\sigma}_\phi\right). \tag{2.30}$$

Here, $\Delta$ is the detuning from the resonance frequency $\omega_{hf}$ and $\Omega$ is the Rabi frequency given by interaction of the dipole operator of the atom's transition and the electric field. Also, $\hat{\sigma}_i$ is a Pauli operator along $\hat{i}$ and $\hat{\sigma}_\phi = \cos(\phi)\hat{\sigma}_x - \sin(\phi)\hat{\sigma}_y$. From Equation 2.30, any of the single qubit Pauli operators can be imparted onto the qubit state of the ion. For example, preparing a $|\uparrow\rangle_z$ is done by first optical pumping, applying the unitary of Equation 2.30

$$\begin{aligned}
&\hat{U}(t)\,|\downarrow\rangle_z = e^{-i\hat{\mathcal{H}}_{int}t/\hbar}\,|\downarrow\rangle_z \\
&\hat{U}(t)\,|\downarrow\rangle_z \approx \cos\left(\tilde{\Omega}t/2\right)\hat{I} + i\sin\left(\tilde{\Omega}t/2\right)\left[\frac{\Omega}{\tilde{\Omega}}\hat{\sigma}_\phi + \frac{\Delta}{\tilde{\Omega}}\hat{\sigma}_z\right]|\downarrow\rangle_z
\end{aligned} \tag{2.31}$$

where $\tilde{\Omega} = \sqrt{\Omega^2+\Delta^2}$. Then, applying a microwave signal with $\Delta = 0$, $\phi = 0$ and applying it for a time $t = \frac{\pi}{\Omega}$ yields

$$\begin{aligned}
&\hat{U}(t)\,|\downarrow\rangle_z \approx i\sin(\pi/2)\,\hat{\sigma}_x\,|\downarrow\rangle_z \\
&\hat{U}(t)\,|\downarrow\rangle_z \approx i\,|\uparrow\rangle_z
\end{aligned} \tag{2.32}$$

Described above is how one would go about preparing the $|\uparrow\rangle_z$ with microwave after an optical pumping sequence.

## 2.4 Chapter conclusion

In this chapter, I introduced some fundamental concepts of ion dynamics in a quadrupole trap. I derived the equations of motion of a charged particle is a quadrupole linear Paul

[2] I introduce the z subscript because the hyperfine states are the eigenvectors of $\hat{\sigma}_z$.

trap. Additionally, I introduced the concept of micromotion. I motivated why micromotion is undesirable, and I then described how it can quantified in various ways. Finally, I introduced some fundamentals required for trapped ion experimental sequences. I talked about how $^{171}Yb^{+}$ can be laser cooled and trapped. Afterwards, I explained schemes such as state preparation, measurement and microwave single qubit logic gates. In the following chapter, I will extend the principles of the quadrupole trap to a multi-segmented blade-style trap, and present the infrastructure needed to achieve these RF frequencies and voltages.

# Chapter 3

# Blade-style trap electronics

This section will outline the progress I helped achieve since the blade trap has been under use. I will begin by giving an overview of the current control over the confining potentials with the many electrodes in the blade trap. Afterwards, I will describe the electronics that I built to deliver the DC and RF signals to the trap. I will end the chapter with some simulation data where I studied the effects of RF phase mismatch for the blade-style trap. The blade trap itself was designed and assembled by Sainath Motlakunda, Nikhil Kotibhaskar and Lewis Hahn. In terms of electronics, I went through the design and assembly process myself, getting advice, suggestions and help from Lewis Hahn along the way.

## 3.1 Segmented blade-style trap

This section will cover the important information about the quadrupole blade-style trap that will be discussed for the rest of the thesis. In this section, I will discuss details about the confining potentials of the blade-style trap.

### 3.1.1 Blade-style trap

A blade-style trap is a specialty ion trap with many similarities to the Paul trap discussed above. Since both of these are quadrupole traps, where the radial confinement is done with oscillating RF electric fields, most of the derivations above follow the ones of the blade-style trap closely.

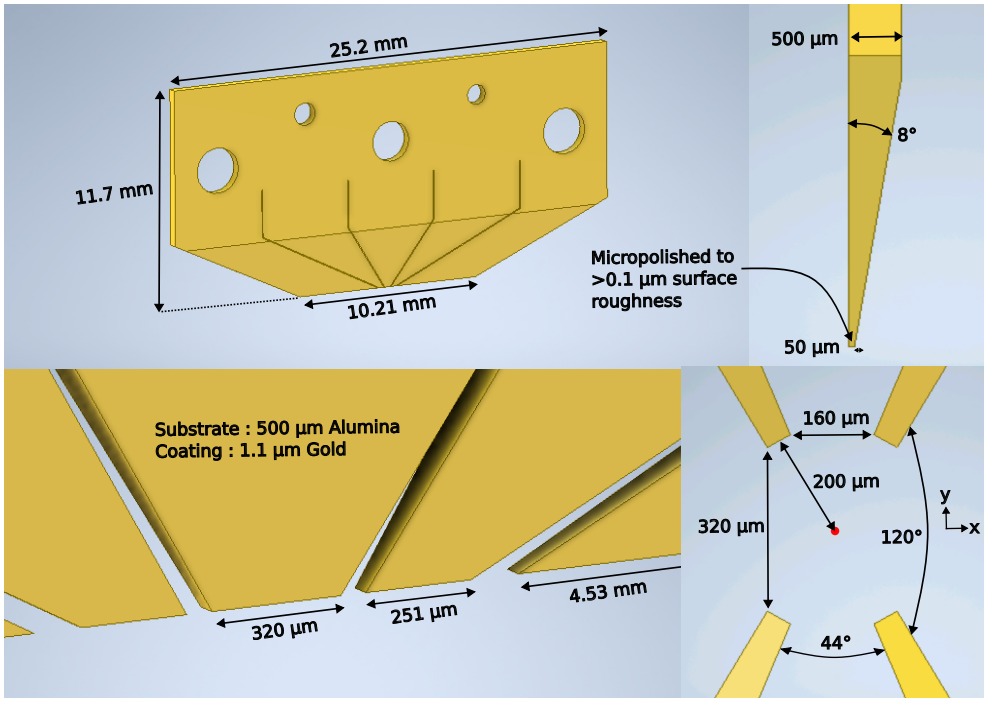



Figure 3.1: Details about the blades in the blade-style trap. Four blades are 5-fold segmented for a total of 20 electrodes.

The blade-style trap used for this work was developed by previous graduate students in the group. Details about blade fabrication, blade assembly, vacuum chamber details and other information can be found in their theses [44, 45, 39]. The blades from the blade-style trap in question are shown in Figure 3.1. It consists of four blades which are individually 5-fold segmented. Notably, the geometric center of the trap where the ions reside is 200 $\mu$m from the tip of the blades, the central segments of the blades is 320 $\mu$m wide and the larger angle between blades is of 120 °.

If this style of trap is similar to the Paul trap, why are people interested in using them?

1. **Deep and Steep potentials**: Blade-style traps offer very deep confining potentials, and they can also reach high trap frequencies, of up to 5 MHz, because of the blade proximity to the ion. Such secular frequencies decrease spectral crowding, and anything beyond requires the blades to be too close to the ion, leading to bad anomalous heating [46]. Additionally, the mass of the ion plays an important role, and reaching 5 MHz secular frequency for $^{171}Yb^{+}$ in a blade trap is fairly novel. Trap depth is

important for keeping ions in the trap, otherwise an event such as a collision with a background molecule could kick an ion out of the potential. On the other hand, large secular frequencies are important for fast quantum logic gates.

2. **Inherent Geometry for Quadratic Potentials**: The inherent geometry of four long identical blades gives rise to very quadratic potentials. Quadratic potentials are important for eliminating higher order terms to the potential, which disrupt the ions motion. Although, this segmented blade trap allows to also generate axially quartic potentials to evenly space ions. Three dimensional traps offer higher quality quadratic potentials than surface traps [21].

3. **High Optical Access**: As this style of trap requires no needles for axial confinement, light can be sent through the axial direction (parallel to all blade faces). Also, this geometry offers $> 0.5$ Numerical Aperture (NA) on both sides ($\hat{x}$ in Figure 3.1) and $> 0.3$ NA on the top and bottom ($\hat{y}$ in Figure 3.1).

4. **Capability to hold long ion chains**: Because of the high secular frequencies achievable with control over axial confinement, blade-style traps are well-suited to comfortably hold linear chains of 30-50 ions.

The principal drawback of the blade-style trap is that it is a hand-assembled trap. Hand-assembled traps are typically more prone to micromotion due to misalignment [27]. Three dimensional traps lack the benefits of microfabrication that surface traps harness. Although the microfabrication precision can not be matched by hand assembly of a blade-style trap, I will later demonstrate that this hand assembled trap exhibits low excess micromotion. Alongside many other benefits of three dimensional traps, this particular hand-assembled segmented blade-style trap has inherently low micromotion, and all the tools necessary to minimize it.

### 3.1.2 Confining potentials

Our blade trap has a total of 20 electrodes and each one of these carry an RF signal and a DC signal. Due to the many electrodes, the naming convention adopted is detailed in Figure 3.2.

To motivate the difference of the confining potentials in regards to a Paul trap, I will highlight the fudge factors introduced from this geometry to display the divergence from hyperbolic geometry. Radial confinement in the trap is done through balanced RF drive.

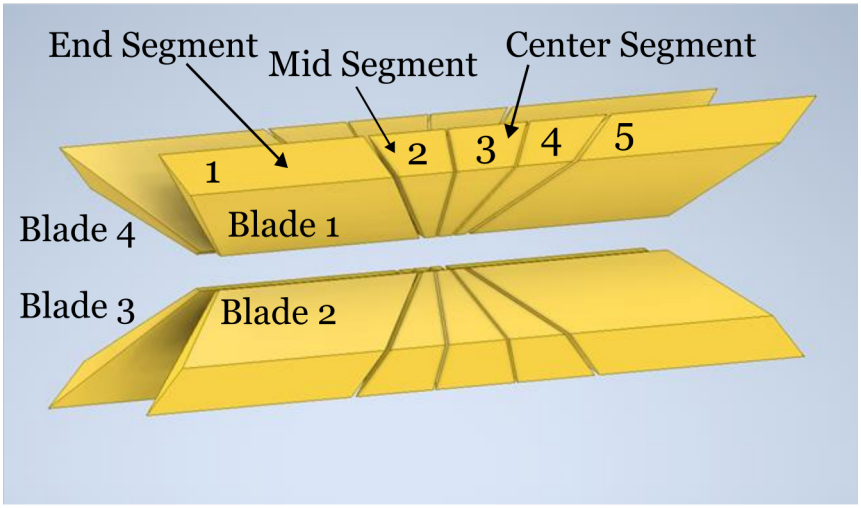



Figure 3.2: **Naming convention for the 20 electrodes in the blade trap.** First, the blades are labeled 1 through 4, and additionally the segments are numbered 1 through 5 on each blade. Therefore, when referring to a certain electrode we may say Electrode-(*Blade*)-(*Segment*), such as E-2-4. Additionally, names are given to the types of segments as End Segment, Mid Segment and Center Segment.

This is done by applying $+V_{rf}\cos(\Omega_{rf}t)$ to blades 1 and 3, and then $-V_{rf}\cos(\Omega_{rf}t)$ to blades 2 and 4. As described in Equation 2.1, we can approximate a certain potential surface near the trap center despite non-hyperbolic electrodes with a correction fudge factor $\eta$. It was previously simulated that our blade trap has $\eta \approx 0.81$ [39].

In terms of the axial fudge factor, it is slightly more complicated to extract it in the case of a segmented blade trap. Because of the 5-fold segmentation, axial confinement is generated from either all end segments, all mid segments, or a combination of both. Therefore, following Equation 2.2, the axial potential of a segmented blade trap follows

$$\begin{aligned} \phi_{axial} &= \phi_{end} + \phi_{mid}, \\ \phi_{axial}(x,y,z) &= \left[\frac{\kappa_{end}V_{end}}{Z_{end}^2} + \frac{\kappa_{mid}V_{mid}}{Z_{mid}^2}\right]\left[z^2 - \frac{1}{2}(x^2+y^2)\right] \end{aligned} \tag{3.1}$$

where the contributions from both end segments and mid segments are included. I gave each of them their own fudge factors $\kappa$ and introduced two distances $Z_{end}$ and $Z_{mid}$. The

subscript *end* and *mid* are to differentiate end segments and mid segments. For these, I will select the distance from the start of the electrode to the geometric center of the trap. Therefore, it was determined that $Z_{end} = 578\mu$m and $Z_{mid} = 214\mu$m. Ignoring any contributions besides the electrodes treated here, our Mathieu $a$ parameter from Equation 2.20 then takes the form

$$a_x = a_y = -\frac{1}{2}a_z = -\frac{4e}{m\Omega_{rf}^2}\left[\frac{\kappa_{mid}V_{mid}}{Z_{mid}^2} + \frac{\kappa_{end}V_{end}}{Z_{end}^2}\right] \tag{3.2}$$

and such, the axial frequency is given by Equation 2.19 as

$$\begin{aligned}
\omega_z &\cong \frac{1}{2}\Omega_{rf}\sqrt{a_z + \frac{1}{2}q_z^2} \\
\omega_z &\cong \frac{1}{2}\Omega_{rf}\sqrt{a_z} \\
\omega_z &\cong \sqrt{\frac{2e}{m}\left[\frac{\kappa_{mid}V_{mid}}{Z_{mid}^2} + \frac{\kappa_{end}V_{end}}{Z_{end}^2}\right]}.
\end{aligned} \tag{3.3}$$

Above, it was taken for granted that $q_z = 0$, which is the case for the quadrupole geometry. From the basis potentials that a previous graduate student Sainath Motlakunta generated for the blade trap, I was able to vary the end segment and mid segment voltages to find the $\kappa$ parameters in terms of the axial trap frequency. This is displayed in Figure 3.3, where I found $\kappa_{mid} = 3.23(6)\cdot 10^{-5}$ and $\kappa_{end} = 2.96(1)\cdot 10^{-4}$. Fitting was done with SciPy and the fit had an $R^2 > 99$ %, resulting in a good fit. Taking the distances $Z_i$ and $\kappa_i$ along with voltages $V_{end}$ and $V_{mid}$, the axial trap frequency can be estimated from Equation 3.3.

For further details on the pseudopotential and effective trapping potential in this blade style trap, refer to [44].

### 3.1.3 Freedom over the confining potential

As already mentioned, our blade trap has a total of 20 electrodes which all carry RF and DC signals. Besides generating the radial and axial confinement described above, what additional freedom over the confining potential do we have? Here I will discuss all accessible controls on the potential with a segmented blade trap. The basis potentials for all 20 electrodes were extracted from COMSOL by Sainath Motlakunta [39], and I post processed them to get these results. To get the basis potentials, COMSOL excites one

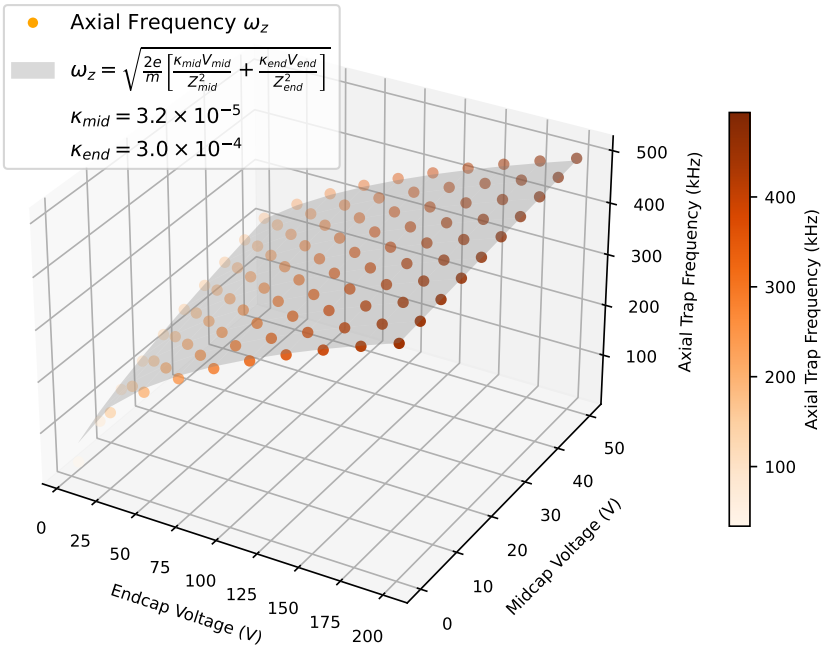



Figure 3.3: Axial trap frequency for various end segment and mid segment voltages. Grey surface represents a SciPy fit to Equation 3.3 to find the fudge factors of the end segments and mid segments. Colored dots represent data extracted from electrostatic simulation.

electrode at a time with 1 V and extracts the potential generated within a grid. After getting the basis for each of the 20 electrodes, the total potential of a combination of different voltages on different electrodes is found by linearly adding these basis potentials multiplied by their respective voltage. The simulation is done on a 8 $\mu$m $\times$ 8 $\mu$m $\times$ 100 $\mu$m grid centered in the geometric center of the trap, where the 100 $\mu$m is along the axial direction $\hat{z}$.

- **Radial Confinement with RF**: This blade-style trap has a balanced RF drive where blades 1 and 3 receive an oscillating voltage that is $\pi$ out of phase from the same voltage received by blades 2 and 4. Figure 3.4(a) displays this confinement which can reach radial secular frequencies of up to $\omega_r/2\pi = 5.1$ MHz with a peak voltage $V_{rf} = 450$ V.
- **Axial Confinement with DC**: The axial confinement is generated by applying a voltage to all end segments or all mid segments, or a combination of the two.

Figure 3.4(b) displays how adding an end segment voltage causes radial anti-trapping, which generates anisotropic radial secular frequencies. Figure 3.4(e) displays the axial quadratic potential for 100 V on the end segments.

- **Rotation of potential radially**: Introduced is a voltage called $V_{skew}$ [44], which has the effect of rotating the potential in the radial plane. To rotate, $+V_{skew}$ is applied on blade 1 and 3, and $-V_{skew}$ is applied on blades 2 and 4. The freedom over the rotation angle is useful when wanting to have some laser project on both radial components. Figure 3.4(c) displays this rotation, which also causes anti-trapping, seperating the radial secular frequencies.

- **Displacement of potential**: The potential can also be freely displaced with all 20 DC controls. This is done by applying a constant voltage on a pair of blades, for example $V_{up}$ would be applied on blades 2 and 3. Radially, there is $V_{up}$,$V_{down}$,$V_{right}$ and $V_{left}$. This is shown in Figure 3.4(d) for a displacement up and right. Axially, we can also displace the potential by applying a constant voltage on all end segments at one end of the blades (from Figure 3.2, either $V_{forward}$ from all electrodes #1 on all blades, or all electrodes #5 on all blades for $V_{backward}$). An axial displacement is shown in 3.4(e). All of these displacements come in handy when minimizing micromotion, as will be discussed later.

Needless to say, even more capabilities are available with segmented blades which are not stated here. Quartic potentials can be generated for equispaced chains of ions [39], a double-well can be generated [44] and many other unique quadratic potentials can be generated using non-trivial combinations of voltages that can be worked out using machine learning tools [31].

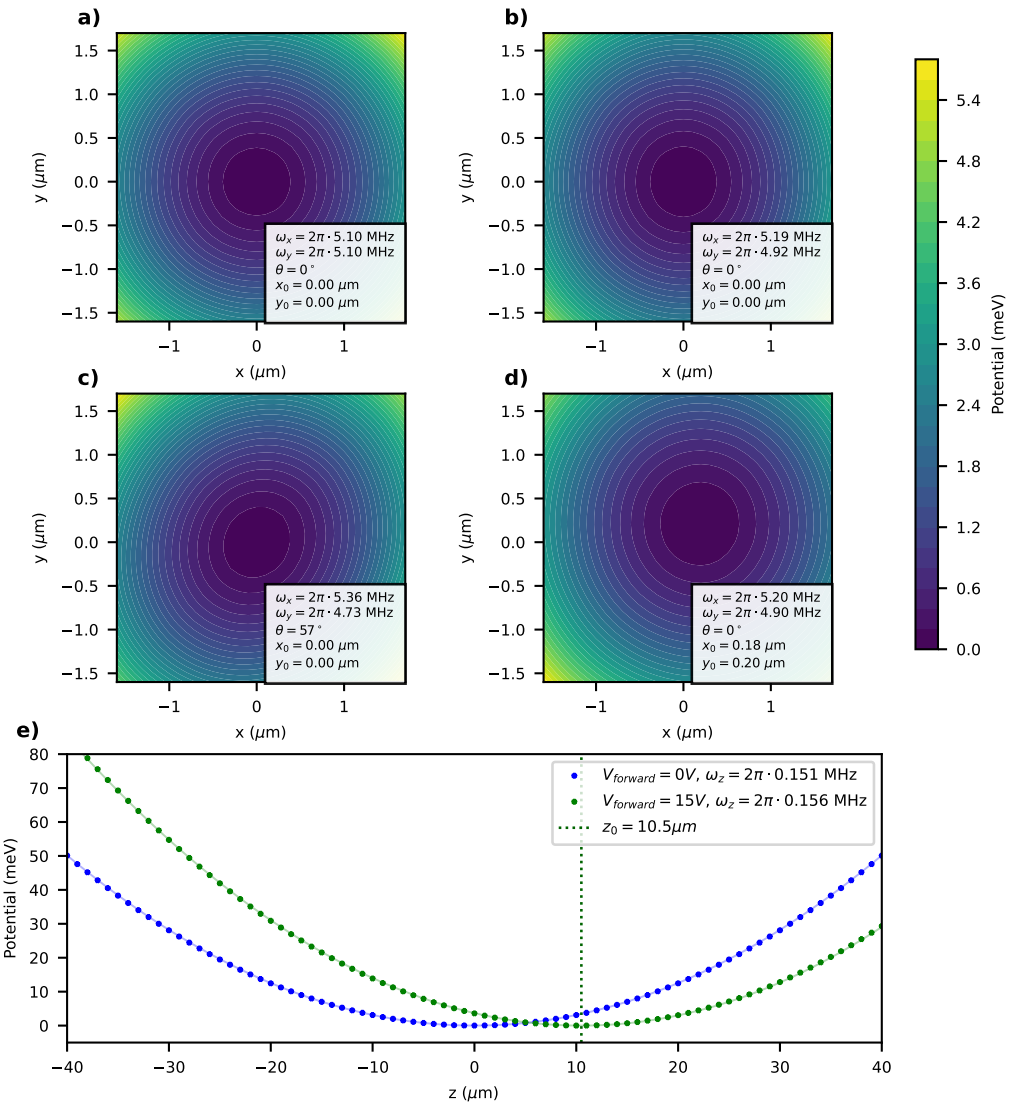



Figure 3.4: Manipulation of the confining potentials in a blade style trap with 5-fold segmented blades with drive frequency $\Omega_{rf}/2\pi = 40$ MHz. Comparison of various manipulations achievable with the many DC controls available. a) $V_{rf} = 450$ V for 5 MHz secular frequency. b) $V_{rf} = 450$V and $V_{end} = 100$ V, end segment voltage causes anisotropic radial potential. c) $V_{rf} = 450$ V, $V_{end} = 100$ V and $V_{skew} = \pm 5$ V, rotates potential by $\theta$ about the $\hat{y}$ axis. d) $V_{rf} = 450$ V, $V_{end} = 100$ V and $V_{up} = V_{right} = 0.15$ V, causes radial displacement of potential. e) $V_{end} = 100$ V with and without $V_{forward} = 15$ V, causes axial displacement of potential.

### 3.1.4 Blade conditioning

Before attempting to trap, it was decided to condition our blades with high voltage RF. Despite our best attempts to create a very clean gold surface on the blades near the ion, imperfections are still bound to be present on the surface. Conditioning consists of sending increasingly high voltage RF until some of these imperfections hopefully melt away and smooth out. If an imperfection is present, with the added surface area it would be expected to flow more current and heat more than a flat surface, and therefore would smooth out. This method is very common for surface traps, and was studied for RF breakdown [47]. The conditioning procedure went as follows:

1. Start at a low peak RF voltage and increment in steps of 25 V until a peak voltage $V_{rf} = 400$ V is reached.
2. Monitor resonator reflection, and adjust drive frequency if need be.
3. Monitor pressure through our vacuum gauge and also monitor temperature of the thermocouple on the ceramic that holds the blades.
4. Monitor Printed Circuit Board (PCB) to see if it is heating up.

Ultimately, it is difficult to know whether this type of procedure does anything, because a device such as a scanning electron microscope would be needed to image the surface quality of the blades before and after. It is still a good procedure to avoid damaging the blades later on with sudden high RF voltage. Although, we did observe and learn a few things along the way, which include:

- The reflection from the resonator would decrease by 0.5 to 2 dB at every 25 V step beyond $V_{rf,peak} = 275$ V. This indicates that the resonance was shifting, which could be because of a change in load resistance or capacitance. This change could also be explained by thermal effects from the resonator. To remain at the estimated voltage, the RF frequency was adjusted at every step, and the changes would be at most 0.1 %.
- Observed no heating of the shapal ceramic blade holder through the thermocouple. This ceramic was chosen because of this low RF heating. Driving the blades at $V_{rf,peak} = 400$ V for 20 minutes showed no considerable shapal heating ($< 0.2$ °C) through our thermocouples on the shapal holder.

- Noticed that the PCB was heating up at $V_{rf,peak} = 400$ V, viewed through an Infrared (IR) thermometer. Although the temperature value on the IR thermometer could not be trusted, there was a local hot-spot on the PCB. The thermometer could not be calibrated, but a relative temperature difference on the PCB was observed. This is a sign that for the next PCB iteration, alternative substrate with lower RF heating compared to the cheaper FR4 should be considered.

## 3.2 Electronics

This section will detail the electronics that I designed to deliver the RF and DC to all 20 electrodes within the vacuum chamber.

### 3.2.1 Electronics targets

In terms of pure electronics targets, previous grad students along with myself set some of these to reach certain secular frequencies and limit noise. These targets can be summarized in a few bullet points:

- **Deliver RF to all 20 electrodes**: A novelty of our design is that all electrodes see an RF signal in the blade trap. 10 of them see a signal that is $\pi$ out of phase, and this will be generated with a balanced helical resonator. This requires splitting the RF outside the chamber and ensuring path length is matched on all 20 electrodes to avoid RF phase mismatch.
- **Deliver a unique and clean DC signal to all 20 electrodes**: Compared to an unsegmented blade trap, this adds a significant level of complexity for the control. Although, the many benefits were listed in the section above. All individual DC signals will be filtered, and then mixed with the RF before entering the vacuum chamber.
- **Do all of this external to the vacuum chamber**: Since no electronics are placed inside the vacuum (besides kapton wires going to the electrodes), everything must be put together outside the vacuum chamber.
- **Target numbers**:
    1. Can reach RF of $V_{rf} = 500$ V (peak voltage)

2. Can reach DC of $V_{end} = 1$ kV and $V_{midcap} = V_{center} = 100$ V
3. Phase matching error between any RF line to be below $\varphi_{rf} < \frac{\pi}{2} \cdot 10^{-2}$

These numbers were chosen from electrostatic simulations in order to reach radial secular frequencies up to 5 MHz. Also, to reach axial secular frequencies up to 500 kHz with the possibility of generating quartic axial confinement, and a path length matching condition which is realistic (on the order of millimeters) when designing a PCB and electronics.

An concern that arises after reading these bullet points is to ask why put electronics outside the chamber? While the concern for noise pickup between the filters external to the chamber and the electrodes is valid, heating rates have not been measured yet, and that will ultimately dictate this. The heating rate mentioned here refers to heating of the motional mode quanta through excitation from electronic noise at their resonance frequency, as stated in Section 2.2.3. On the upside, having the electronics external to the chamber allows for very fast prototyping of electronics. For example, DC filters could be adjusted in a few hours by changing capacitors that are external to the vacuum chamber.

### 3.2.2 Resonator for radio-frequency amplification

Generating a stable source of a 40 MHz signal at 500 V peak voltage is quite non-trivial. Fortunately, driving the RF of a quadrupole ion trap with a helical resonator acts as an Inductor Capacitor Resistor (LCR) circuit. The trap-resonator can exhibit a resonance in the RF regime, and generate the desired high voltage oscillating signals. I built the resonator for our ion trap following the methods given by Siverns *et al.* [48].

The trap-resonator combination with capacitive load $C$ and resistive load $R$ driven by a resonator with inductance $L$ has a resonance and quality factor

$$\omega_0 = \frac{1}{\sqrt{LC}}, \tag{3.4}$$

$$Q = \frac{\omega_0}{\Delta\omega_{FWHM}} = \frac{1}{R}\sqrt{\frac{L}{C}}. \tag{3.5}$$

Here, $\Delta\omega_{FWHM}$ is the Full Width Half-Maximum (FWHM) around the resonance. By considering the peak voltage across the inductor $V_{peak} \approx L\omega_0 I_{peak}$[1] and the dissipation through the resistor $P = \frac{1}{2}RV_{peak}^2$, the peak voltage across the LCR circuit is given by

[1] This voltage is oscillating, but we consider the voltage at a time $t$ where the sinusoidal term equals 1.

$$V_{peak} \approx \kappa\sqrt{2PQ} \tag{3.6}$$

with $\kappa = (L/C)^{1/4}$.

During the design of our resonator, I wanted to maximize the $Q$, which reduces the power $P$ in Watts necessary to reach high voltages. Additionally, I was wanting to limit the capacitive load on the system as $Q \propto C^{-1/2}$. The target was a resonator at around 40 MHz with a high quality factor $Q$.

The balanced helical resonator designed follows the instructions given in [48]. Within a copper can of inner diameter 76.2 mm and length of 75 mm, I inserted a primary coil, and a secondary coil of inductance $L$. The primary coil is driven by an RF source (Rohde & Schwarz SMB100B) amplified by an RF amplifier (RF Bay MPA-40-40), which is then grounded to the can after passing through the primary coil. On the contrary, the secondary coil has both leads left open ended out of the copper can, leaving the two outputs as a differential pair oscillating $\pi$ out of phase.

Building these coils requires some optimization because the goal is to hit a target resonance $\omega_0$ with a maximal quality factor $Q$. Therefore, the secondary coil parameters have to be optimized to find the best $Q$ based off of trap characteristics $C_{trap}$ and $R_{trap}$ as well as the inherent capacitance present within the helical resonator can. Our secondary coil made of bare copper has parameters length $b = 50$ mm, coil diameter $d = 30$ mm, wire diameter $d_w = 5.2$ mm and number of turns $N \approx 5.8$. Although higher $Q$ values could have been achieved with a smaller coil diameter $d$, this configuration was the most feasible due to the hand assembly which is very difficult to wind with the wire diameter of $d_w = 5.2$ mm. Figure 3.5 displays the secondary coil that was wound using a 3d printed piece and the final design of the helical resonator can. The coupling of both coils is done by mechanically displacing the primary coil within the secondary until the impedance is matched and power gets transmitted.

To characterize our resonator, the signal is passed through a bi-directional coupler, and the reflection signal out of the resonator is observed. Using the tracking generator function on our spectrum analyzer (Rigol DSA832-TG), the resonance where power is minimally reflected from the resonator can be found. Figure 3.6(a) displays the circuit to measure our $Q$, while Figure 3.6(b) displays the signal observed. From this signal, I found that the resonance $\omega_0$ and the FWHM $\Delta\omega_{FWHM}$ to extract the $Q$ parameters. From a reflection signal, the FWHM is measured 3 dB away from the noise floor. As the resonator gets loaded, the added capacitance decreases the $Q$ considerably, which is why all capacitive loading must be avoided. By considering that the inductance $L = 0.54$ $\mu$H of the secondary

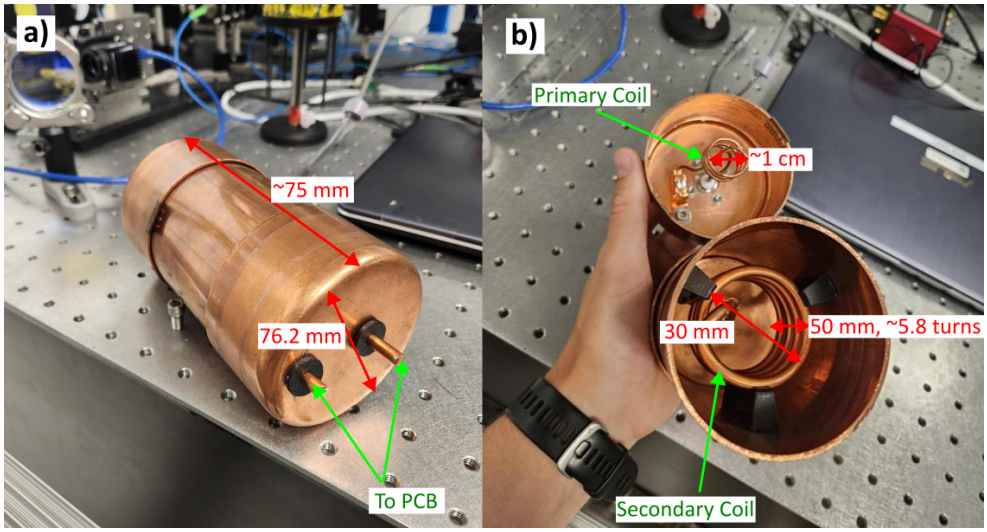



Figure 3.5: Helical resonator can for RF amplification. a) Fully assembled resonator can, showing the two metal conductor leads that connect to the mixing PCB. b) Internals of the resonator. Primary coil was built to fit inside the secondary to reach good coupling when mechanically adjusting. Secondary coil is fixed in the can with 3d printed brackets.

coil stays fixed, the total capacitance $C$ and resistance $R$ can be extracted from the $Q$ and $\omega_0$ parameters using Equations 3.5 and 3.4.

| **Resonator Load** | **Capacitance Added** |
|---|---|
| Bare Resonator (Unloaded) | 3.3 pF |
| Loading with PCB | 13.9 pF |
| Loading with in-vacuum wires + trap | 28.2 pF |
| **Full loaded system** | **45.2 pF** |

Table 3.1: Loading of resonator from different stages between the resonator and the trap. This capacitance permits us to operate at a frequency $\omega_0 = 2\pi \cdot 35.12$ MHz with $Q \approx 72$. The added resistance is not indicated because the bulk of the resistance arises from the bare resonator itself. Capacitive loading is typically the challenge as anything near the electronics can capacitively couple to a pF level.

After the measurement of the resonator with different loads, it was determined that the total added capacitance and resistance from various loads in our system can be summarized, as displayed in Table 3.1. This data was obtained by measuring the $Q$ and resonance

frequency $\omega_0$ with a varying load on the resonator. Although our $Q$ is only $Q = 72$, I was able to reach a trap frequency of $\omega_0/2\pi = 35.12$ MHz, very near the target of 40 MHz. Additionally, from Figure 3.6(b), $> 30$ dB coupling is obtained. In the next section I will discuss the PCB mentioned in the table.

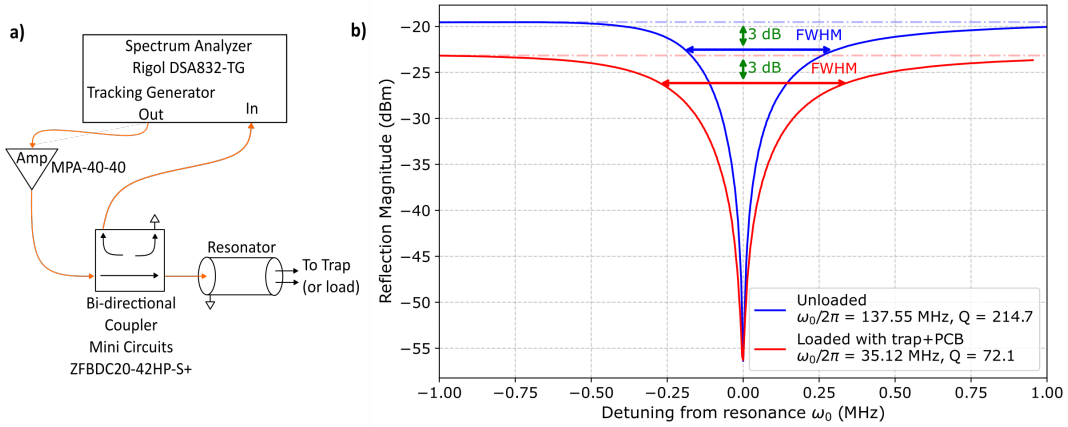



Figure 3.6: Measurement of the $Q$ from the reflection of the resonator with a tracking generator on a spectrum analyzer. a) Setup for measurement using a bi-directional coupler. b) Effective traces for our resonator loaded and unloaded, measured with span of 2 MHz and resolution bandwidth of 10 kHz. FWHM is measured 3 dB away from the noise floor (dash-dot line).

### 3.2.3 Printed circuit board for mixing

The PCB outside of the vacuum chamber is one of the novelties of our ion trap. This PCB serves 3 principle purposes:

1. Combine the RF and DC signal for all 20 electrodes.
2. Filter the DC signals before entering the chamber.
3. Ensure all 20 path-length matched traces are fed to the vacuum feed-through.

The PCB layout is displayed in Figure 3.7. This PCB was designed in KiCAD. Figure 3.7(a) displays the schematic of the electronics. Simply put, 20 DC signals first get low-passed, and then get mixed with one of the two out-of-phase RF signals through and RC

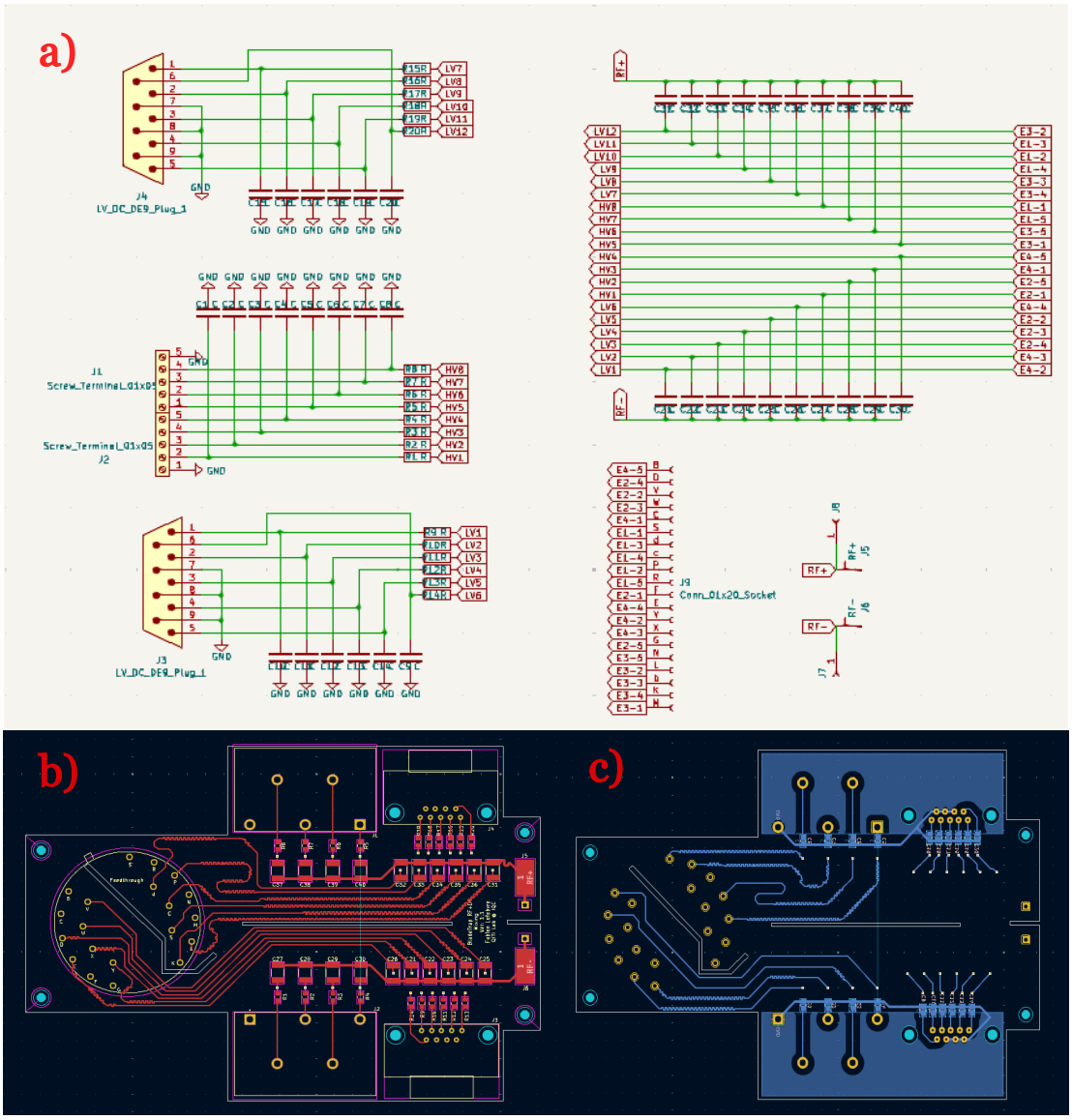



Figure 3.7: RF and DC mixing PCB. a) Schematic of the electronics on the PCB. Three connectors in yellow lead to low-pass DC filters, and then the signal is mixed with either the in-phase RF or out-of-phase RF. Afterwards, a mapping is done for the labeling of our vacuum feedthrough. b) View of the top layer of the PCB. c) View of the bottom layer of the PCB.

mixer. Afterwards, all 20 mixed signal traces are delivered to the vacuum feedthrough to deliver the 20 signals to the blades.

**Filtering of DC**: The lowpass filter on all DC lines was chosen to have a cutoff frequency $f_c = 1/(2\pi RC) \approx 160$ Hz with $C = 100$ pF and $R = 10$ MΩ. This capacitor (Part#: QCCT102Q101J1GV001E) was chosen because of its low error ±5% and its low thermal coefficient C0G NP0 ±30 ppm/K. The resistor (Part#: RCS080510M0FKEA) was chosen with similar attention, where its error is of ±1 % with a temperature coefficient of ±100 ppm/K. Both of these components also were selected to be able to handle up to 1 kV of DC or RF signal.

In terms of the mixing, the goal is have the RF see high impedance on the DC line, and the DC to see high impedance on the RF line. Typically, these mixing circuits are done with an RL circuit, but because of the high RF voltage, a capacitor will have to be used instead of an inductor because of its higher voltage handling capabilities. The resistor used is the same as the low-pass filter, while I selected a mixing capacitor (Part#: C1812C334KCRACTU) of $C = 0.33$ μF. For this capacitor, because of its higher capacitance it was more difficult to find one with a small error, and I had to resort to one with error of ±10 %. The circuit of the mixing is displayed in 3.7(a).

**Johnson-Nyquist Noise**: While selecting the components, I also considered the Johnson-Nyquist noise that these components would introduce. I do not consider shot noise in the analysis because the current flowing through the system is minimal, and operates in more of a steady-state. Johnson-Nyquist noise is considered for both components which mix the RF and DC. In terms of noise at $f = 40$ MHz from the resistor, the Johnson-Nyquist Root Mean Square (RMS) voltage noise is given by

$$V_{rms} = \sqrt{4k_B TRf} \approx 2.5 \text{ mV} \tag{3.7}$$

where $k_B$ is the Boltzmann constant, $T$ is the room temperature in Kelvin (300 K) and $f$. This noise should be negligible relative to the 100s of volts that are sent in RF to the trap. In terms of the capacitor, I do not consider the noise it could introduce because there is no switching on the capacitor during regular operation, and therefore "kTC" noise can be ignored [49]. This noise arises from charge build-up and is proportional to $k_B TC$.

**Path Length Matching**: Furthermore, the path-length matching was done using built-in KiCAD functions. Although, the path-length matching does not only matter on the PCB. The kapton wires in the vacuum chamber that connect the feedthrough to the in-vacuum electrode PCBs were cut to $< 5$ mm length matching. As such, the target on the PCB was to match the path length of all RF traces to the output below $< 2$ mm.

As can be seen in Figure 3.7(b-c), the path length matching is done through serpentine routing.

**PCB DC + Grounding**: The approach for grounding on the PCB was fairly straightforward. The ground plane on Figure 3.7(c) is set by the ground of the 20 DC signals coming from a common DC crate. The reasoning behind a partial ground plane in regards to a full ground plane on the circuit is to avoid any capacitive loading of the resonator. While it is ideal to keep a signal trace above a ground plane, in our application we want to avoid any capacitive coupling to the ground which would increase the resonator load, and decrease the quality factor $Q$.

The PCB receives 20 DC signals from a common crate (ISeg EHS-84-01p and EHS-84-10p). High voltage terminal blocks were added for the end segment traces (because they can take up to 1 kV), and DSub terminals were added for all other 100 V traces.

**Power Handling Capabilities**: For the first version of the PCB, the substrate was chosen to be FR-4. As the most cost effective substrate, it was chosen in case of possible design reiteration. Traces with various maximal voltages were spaced apart vaguely following IPC-2221B standards. Additionally, all components and terminal blocks were chosen to sustain the maximal power any of the sources could deliver.

Additionally, on the PCB next to the big solder pads for the RF input (next to the PCB naming label), two small soldering connections were added for the future addition of an RF sampling circuit. While still an on-going project, it is planned to add an RF sampling circuit to stabilize the RF power going to the trap.

**Connection to the Vacuum Feedthrough**: The physical board is displayed in Figure 3.8(a). The kapton wires seen in Figure 3.8(b) were placed on the PCB to match the pin positioning on the feedthrough connector (Kurt J. Lesker IFTRG327013). All of these kapton wires were also cut to $< 5$ mm for path length matching. Originally a connector was bought to connect directly to it, but it was observed by previous graduate students Nikhil Kotibhaskar and Sainath Motlakunta that the connector itself loaded the resonator by a lot. Hence, these wires are connected directly to the feedthrough connector.

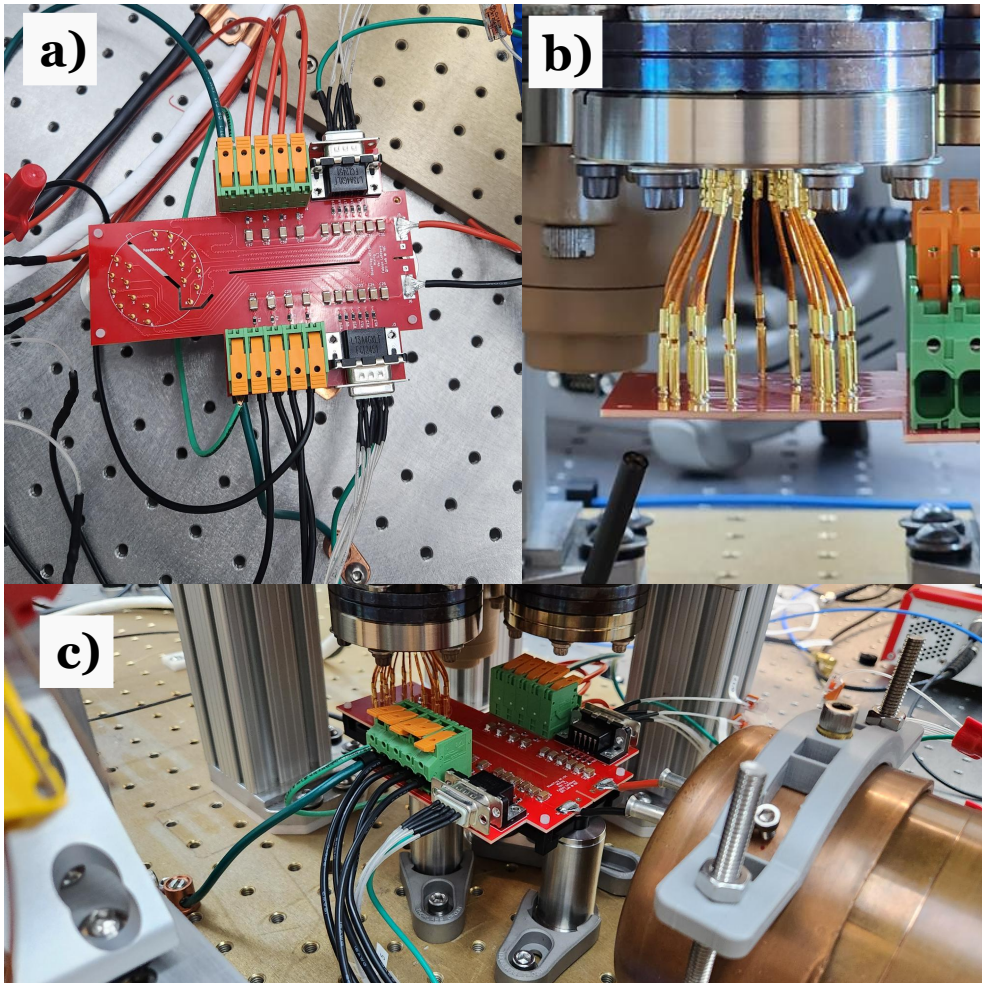



Figure 3.8: Physical mixing PCB. a) Board itself with the green terminal blocks for the 1 kV DC signals and the Dsubs for the 100 V DC signals. The RF is delivered through the red and black leads to the right. Connections for feedthrough wires are to the left of the PCB. b) Kapton wires connected directly to the PCB pins to the feedthrough. c) Full system with 20 DC sources and the resonator connected. PCB ground is referenced to the DC sources.

### 3.2.4 DC control software

Because of the complicated mapping from our DC supply channels to the electrodes themselves, I wrote a Graphical User Interface (GUI) for ease of setting voltages on all 20

electrodes. The GUI was written through Python using the PyQt6 package. This is a user friendly package with a great toolkit for generating GUIs.

The aim for the GUI was to group together electrodes to be able to apply some global change to the confining potential. While in other simpler trap geometries like a Paul trap it would be common to adjust a single voltage at a time, in a complex geometry like a segmented blade trap, it is more common to adjust groups of voltages together.

The GUI itself is displayed in Figure 3.9. The various groups are shown in the first column, where $V_{end}$, $V_{mid}$ and $V_{center}$ pertain to the groups shown in Figure 3.2. Then, $V_{skew}$ is used to apply a rotation to the potential as shown in Figure 3.4(c). Finally, 6 displacement voltages (in both directions for all 3 spatial directions), are individually grouped. These displacements will come in handy to relocate the ion in the trap for micromotion compensation. In addition, offset voltages can be added to individual electrodes if need be. The voltages and currents of all 20 electrodes are then updated in real time and displayed on the GUI.

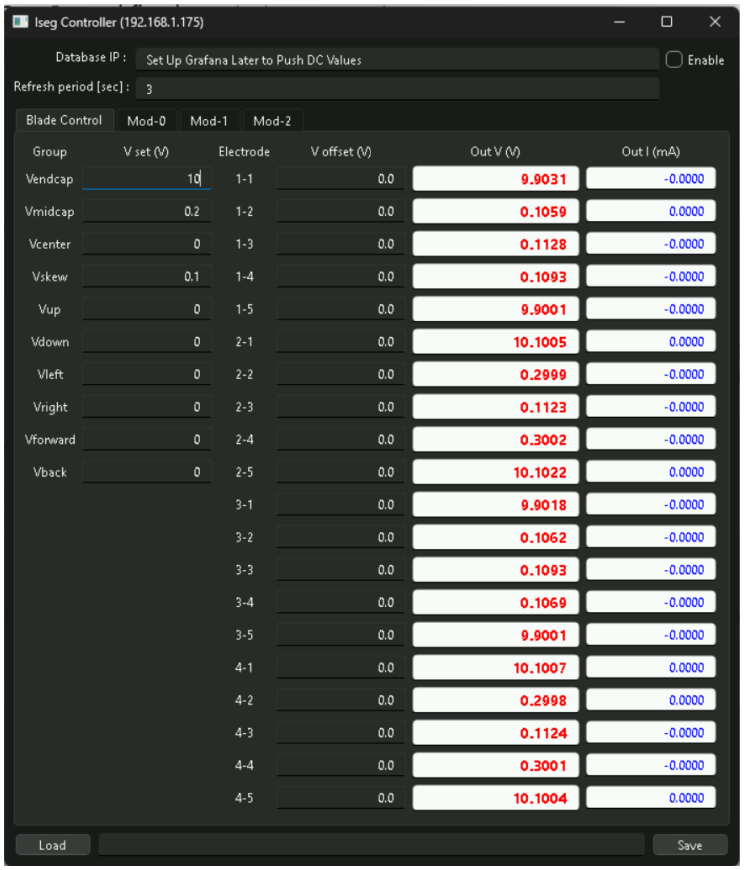



Figure 3.9: ISeg controller GUI built using the PyQt6 Python package. The currents are all 0 here because of the steady state reached in the system. Current mostly flows when changing voltages.

## 3.3 RF phase errors in the blade trap

A valid concern with the approach where the RF is split outside the vacuum chamber is that there might be an RF phase error between electrodes which could cause micromotion. Using the ion trajectory method mentioned above, the added intrinsic and excess micromotion from a phase error on the end segment, mid segment or center segment electrode can be extracted. In this section, these effects are studied.

The following simulations were performed for a single ion in a the blade trap where $\Omega_{rf} = 2\pi \cdot 40$ MHz, $V_{rf} = 400$ V and $V_{end} = 5$ V. The trajectory is then simulated as an

RF phase error on various segments is applied.

### 3.3.1 RF phase error - intrinsic micromotion

Given that the intrinsic micromotion and secular motion amplitudes are well known from the FFT of the simulation, the Mathieu $q_i$ parameters can be extracted from both amplitudes given in Equation 2.21. Figure 3.10 displays the change in the Mathieu $q_i$ parameters along all 3 motional axis for RF phase errors applied on a single of the 20 electrodes. The RF phase error is varied from $\frac{\pi}{2} \cdot 10^{-5}$ to $\frac{\pi}{2} \cdot 10^{-2}$ since it is believed that our RF phase is matched to at least $\frac{\pi}{2} \cdot 10^{-2}$ between all electrodes.

A few interesting observations from these simulations indicate that:

- A phase error on any of the 3 types of electrode segments causes the $q_z$ parameter to become non-zero. This indicates that from Equation 2.20, the RF is now projecting onto the $\hat{z}$ axis and contributing to the axial confinement. The largest contribution to this is phase errors on the mid segment. This axial intrinsic micromotion is non-compensable.
- The radial Mathieu $q_x, q_y$ parameters are driven away from each other as an RF phase error is applied to the mid segments or end segments. This can cause challenges if the goal is to have isotropic radial frequencies, and requires further DC compensation to satisfy this condition. The changes in $q$ displayed here do not cause a risk to exit the Mathieu stability region based on the results of the simulation[2]. For the center segment, the curve is non-monotonic which will require further investigation.

The biggest take away from Figure 3.10 is that the intrinsic micromotion causes a non-zero $q_z$ parameter which is non-compensable.

### 3.3.2 RF phase error - excess micromotion

From the same data set, the amplitude of the excess micromotion can give information about the stray electric field $\mathbf{E}_{dc}$ added when an RF phase error is present. Figure 3.11 displays the change in the stray electric field causing excess micromotion. This electric field can be extracted from Equation 2.22 given that the secular frequency $\omega_i$ is known.

The takeaways of the change in excess micromotion are that:

[2]Exiting the Mathieu stability region would yield an ion trajectory which does not follow Equation 2.21. At the $q$ parameters displayed in Figure 3.10, this is not the case.

- An RF phase error on the end segment causes a considerable increase in axial stray electric field.
- An RF phase error on the mid segment causes a considerable stray electric field along all 3 motional directions. The field added along the axial direction follows a non-monotonic behavior.
- An RF phase error on the center segment causes a stray electric field along both radial directions.

Although these can in theory be compensated with a compensation DC field from the DC control of the 20 electrodes, these are undesirable. An important note about the plots from Figure 3.10 and Figure 3.11 is that this treats a single RF phase error on one segment while all others remain in phase. This may not be the most accurate case in practice, since the relative phase errors between all electrodes would be more randomized. Therefore, these effects can be expected to be somewhat washed out when all electrodes are subject to one of these random RF phase errors.

## 3.4 Chapter conclusion

In this chapter, I introduced the multi-segmented blade-style trap. I presented some work on understanding how the ion is confined in such a quadrupole trap, and demonstrated the full control available with all the DC control from the blade segmentation. Additionally, I presented the advantages of balanced radio-frequency drive. Afterwards, I presented the physical implementation of our fully out-of-vacuum electronics that drive the electronic controls of the blade trap. The resonator and PCB designed were introduced, along with the control software for manipulating the DC controls. I additionally presented some work for understanding the effects of RF phase mismatch on electrodes leading to micromotion. The next chapter will demonstrate some of the first data collected in the blade-style trap using the electronic infrastructure described above.

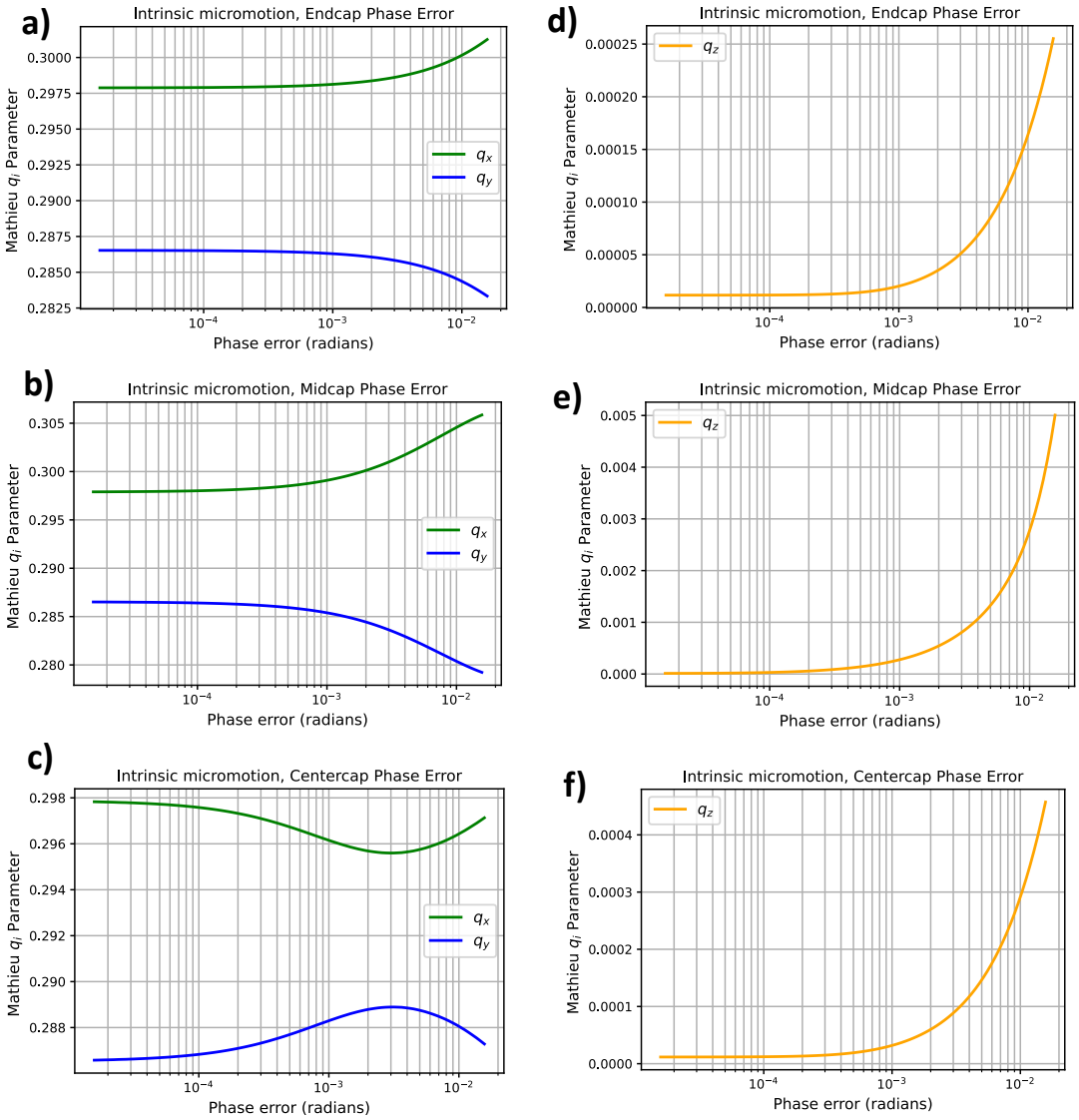



Figure 3.10: Intrinsic micromotion for varying phase errors on various electrodes. Vertical axis displays Mathieu $q$ parameter from Equation 2.20 along all three spatial directions. For the simulation, $\Omega_{rf}/2\pi = 40$ MHz, $V_{rf} = 400$ V and $V_{end} = 5$ V.

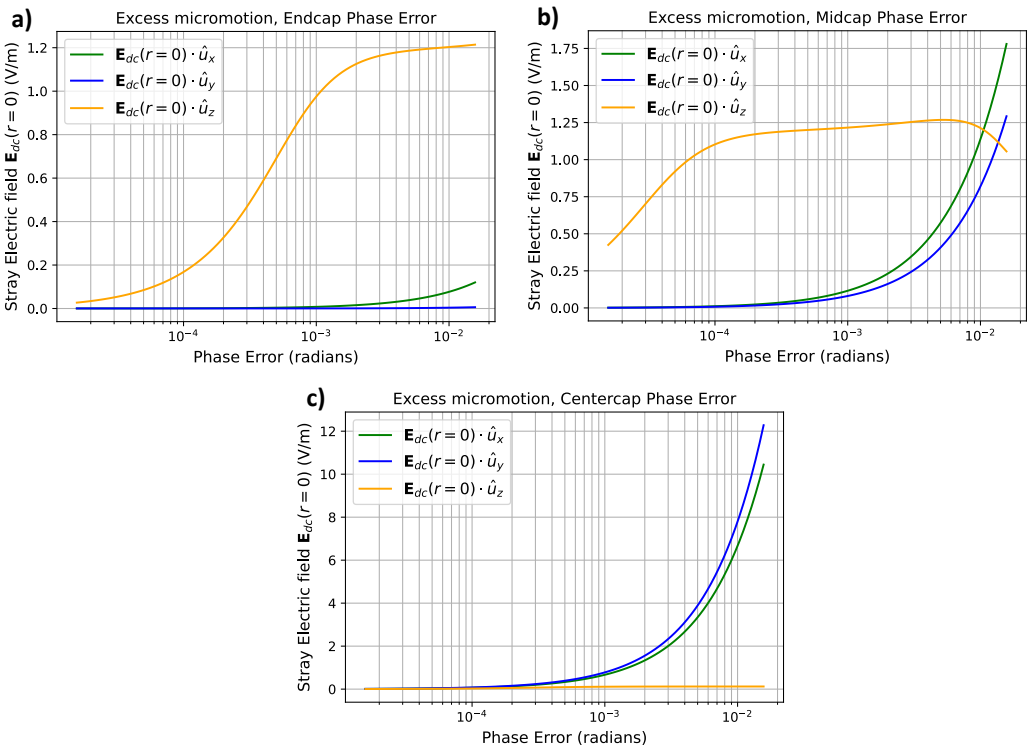



Figure 3.11: Excess micromotion for varying phase errors on various electrodes. Vertical axis displays residual stray electric field from Equation 2.20 along all three spatial directions. For the simulation, $\Omega_{rf}/2\pi = 40$ MHz, $V_{rf} = 400$ V and $V_{end} = 5$ V.

# Chapter 4

# Trapping $^{171}Yb^{+}$ in a blade-style trap

This section will go over the data that the group obtained with the segmented blade trap. I will first go over some details about the laser light delivery and controls. Afterwards, I will show some single ion data. Every member working on this experiment individually contributed towards achieving this data. Lewis Hahn designed the imaging and was present during the collection of the data. Shilpa Mahato and Sakshee Samir Patil helped with setting up the lasers, and the optical engineering to deliver the light to the chamber. Shilpa Mahato also designed the microwave delivery. I designed the electronics, and with Lewis Hahn (equal contribution) wrote the experimental scripts and collected the data for all these scans. The analysis of the data was a shared effort between all group members.

## 4.1 Addressing the ions

### 4.1.1 Laser light delivery

Laser light delivery in the blade trap is fairly straightforward for a few reasons. Firstly, the segments on the blades and the proximity of the blades to the ions make it very easy to align lasers. Secondly there is plenty of optical access to deliver light from multiple directions.

For initial trapping, we set up some temporary delivery modules to confirm that we could trap ions. Figure 4.1 displays the light delivery to the chamber. All 369 nm, 399 nm, 760 nm and 935 nm lasers are External Cavity Laser Diode (ECDL)s from MogLabs which are frequency stabilized using a wavelength meter (WS8-2 from High Finesse GmbH). The

760 nm laser is used as a secondary repump to remove population from the metastable $^2F_{7/2}$ state which has a lifetime of $\tau \approx 5.4$ years. We also deliver 355 nm light into the chamber for our final ionization of the neutral Yb. This frequency tripled Nd:YAG pulsed laser from Coherent (Paladin Compact 4W) has up to 3.75 W available. We currently focus the 355 nm light at an intensity of $4 \times 10^5$ mW/cm$^2$, which makes the ionization process rapid after the 399 nm excitation.

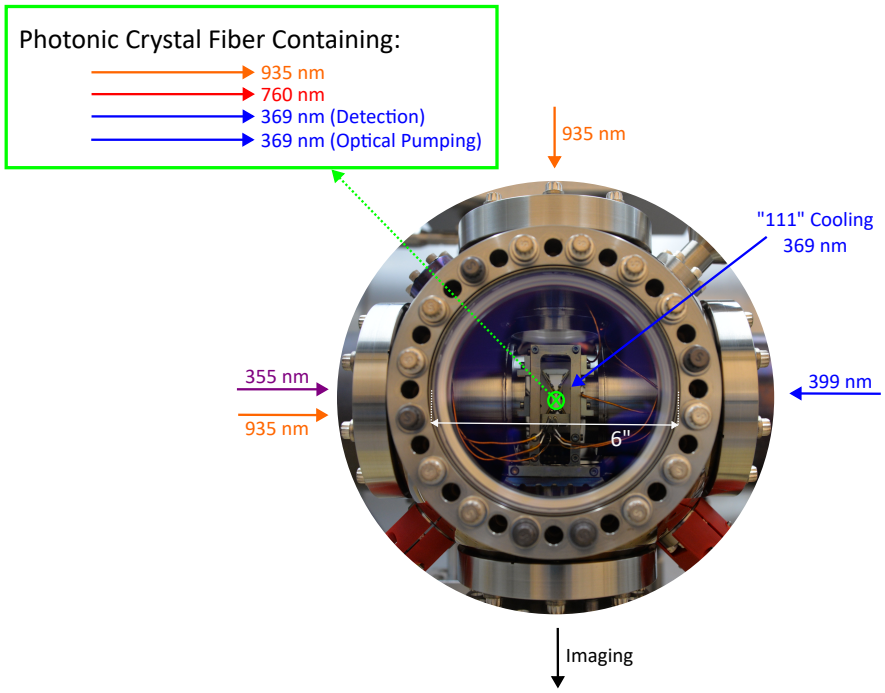



Figure 4.1: Blade trap first trapping temporary light delivery setup. This was how light was delivered for all data presented in the rest of the thesis. The "111" cooling beam is a beam projecting on all 3 motional axis, and therefore we only need a single Doppler cooling beam.

During initial trapping attempts, we learned that our natural abundance atomic oven was malfunctioning most likely due to oxidization of the metal source. Therefore, we decided to bypass trapping $^{174}$Yb$^+$ which is easier to trap and cool because of its zero nuclear spin and absence of coherent dark states. We directly trapped $^{171}$Yb$^+$ with our functioning enriched $^{171}$Yb$^+$ atomic oven. Figure 4.2 displays a chain of 25 $^{171}$Yb$^+$ ions imaged by collecting cooling fluorescence light through a 0.3 NA objective and imaging onto a qCMOS camera (C15550-22UP from Hamamatsu). For more information about the

imaging, refer to Lewis Hahn's MSc thesis [45].

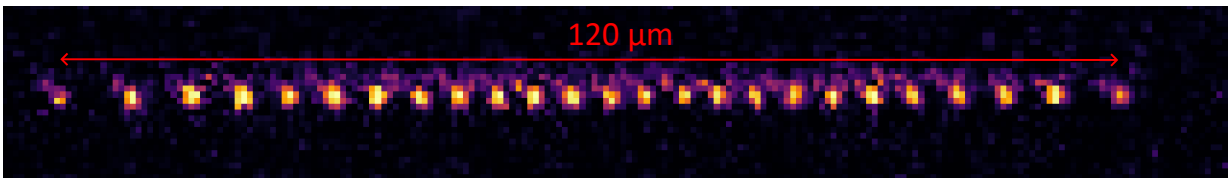



Figure 4.2: False color image of a linear chain of 25 $^{171}Yb^{+}$. Ion fluorescence collected through a 0.3 NA imaging system and imaged onto a Hamamatsu qCMOS camera (C15550-22UP) of pixel size 4.6 $\mu$m. Ions are approximately spaced by 3.5 $\mu$m towards the center of the chain, which is more than the imaging resolution. Individual ion non-uniformity is because of residual aberration in the imaging system.

### 4.1.2 Control system

To run experiments, we use an ARTIQ crate from M-Labs [50]. This crate acts as an Field Programmable Gate Array (FPGA) with Transistor-Transistor Logic (TTL) outputs, Direct Digital Synthesizers (DDS) outputs, Digital to Analog Converter (DAC) outputs and many more. Beyond serving as a high quality FPGA with a great physical interface, all experiments on ARTIQ are coded in native Python.

I set up the control system along with other graduate students in the group. Figure 4.3 displays our current ARTIQ crate. We placed the ARTIQ crate above our microwave sources that drive EOMs and our homemade amplifier box containing the MPA-40-40s. The proximity of the ARTIQ to the amplifier box is useful for the experiments since we need to amplify the signal before sending it to Acousto Optical Modulator (AOM)s. Below is a table of the current connections to ARTIQ for experiments with ARTIQ:

| **Experimental toggle** | **Artiq Card** | **Recipient** |
|---|---|---|
| Cooling | Urukul DDS | Cooling AOM |
| Detection | Urukul DDS | Detection AOM |
| Optical Pumping | Urukul DDS | Optical Pumping AOM |
| Microwave Signal | Urukul DDS | Mixer to reach $\omega_{hf}/2\pi = 12.6428$ GHz |
| 935 nm frequency | Urukul DDS | 935 nm EOM |
| 935 nm power (x3) | Zotino DAC | Voltage Variable Attenuator |
| PMT signal | TTL | PMT |

Table 4.1: Artiq distribution for experiments.

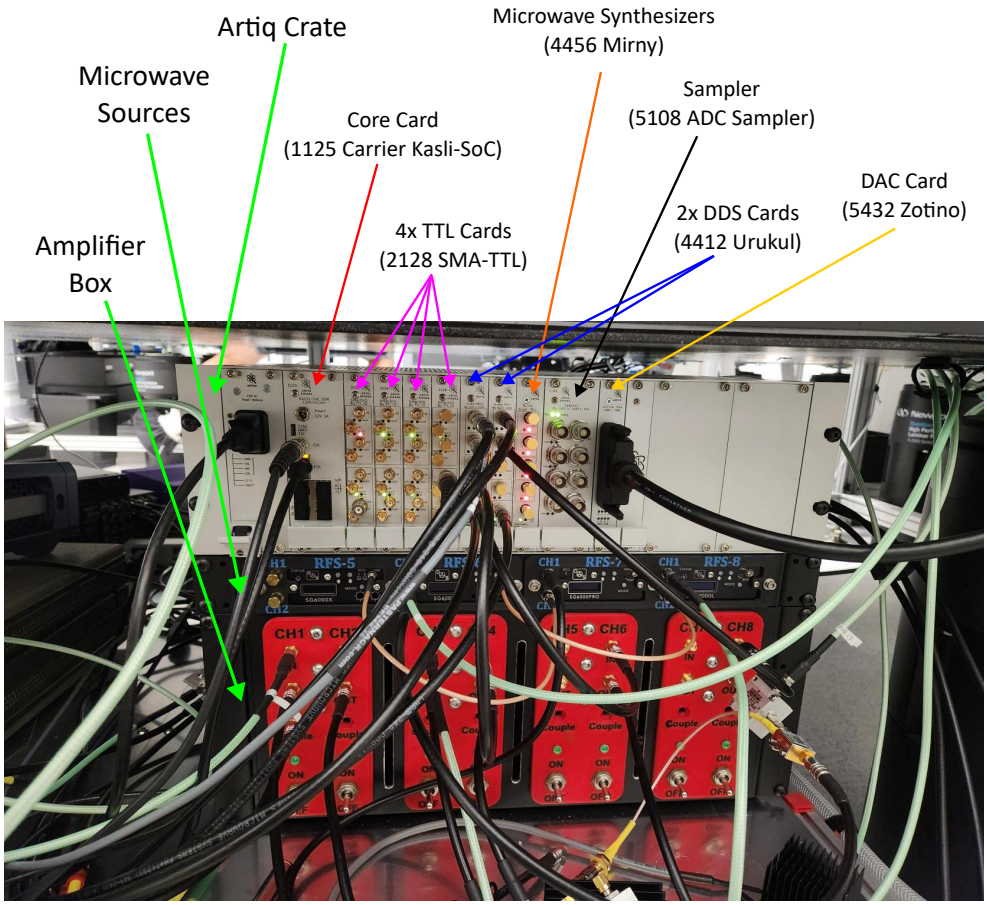



Figure 4.3: Stack around our control system.

## 4.2 First ion data

### 4.2.1 Microwave Rabi

Shortly after trapping ions, we began our first characterizations of the system with some microwave scans. The $\omega_{hf}/2\pi = 12.6428$ GHz signal is passed through a microwave horn directed towards the geometric center of the ion trap. Figure 4.4 displays flopping on the qubit states in the hyperfine manifold. We get a microwave Rabi frequency of $\Omega/2\pi \approx$ 166 kHz.. I plotted absolute PMT counts for simplicity. For this microwave scan, the ion

was first Doppler cooled, state prepared to $|\downarrow\rangle_z$ and then exposed to microwave radiation resonant to the qubit frequency.

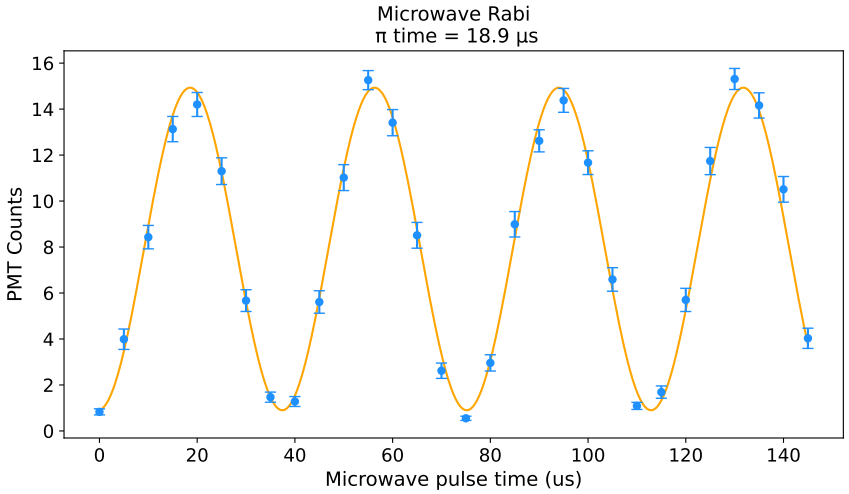



Figure 4.4: Microwave Rabi flopping on the qubit states. Fit represents the function $A\sin^2(Bt+C)+D$, with the error bars as the standard error. 100 shots taken per data point, with the bright state $|\uparrow\rangle$ equal to about 15 PMT counts.

### 4.2.2 Ramsey scans

We start gaining intuition about the system when performing Ramsey scans [51] on both the qubit states and the Zeeman states. A Ramsey scan is commonly used to characterize the dephasing time between the qubit clock and the local oscillator clock. This is typically measured as a $T_2^*$ time, and it quantifies how long the qubit's phase remains coherent. A typical Ramsey scan begins by a $\delta$ detuned microwave $\pi/2$ rotation ($\hat{\mathcal{R}}_x(\pi/2)$), a wait of time $t$ and then another $\hat{\mathcal{R}}_x(\pi/2)$. The detuning $\delta$ determines the precessing frequency along $z$ during the delay time $t$. Since both pulses are chosen to be along $x$, this precessing will be mapped to the $\sigma_z$ basis which we can detect via state dependent fluorescence.

Figure 4.5(a) displays a Ramsey measurement on the qubit states in the blade trap. Oscillations persist even after a wait time of over half a second. The fitting function is a lopsided Gaussian Ramsey given by:

$$N(t) = \sin(\delta t + \phi)\cdot \alpha e^{-t^2/\tau^2} + \beta(1-e^{-t^2/\tau^2}) + c \tag{4.1}$$

where $N$ is the number of counts from the PMT, $\alpha$ and $\beta$ are fit parameters, $\phi$ is a phase offset, $\tau$ is the Gaussian decay, $\delta$ the detuning from resonance and $c$ is a constant offset. These are summarized in Table 4.2. I am choosing to fit the Ramsey data to this model because for the timescales in question, the central limit theorem states that the summation of many noise sources will average out to be Gaussian [52]. Additionally, while Figure 4.5(a) deals with a timescale that could include a mixture of correlated and uncorrelated noise sources, this fitting function is chosen for a comparison with Figure 4.5(b). A more careful experimental procedure would be to perform a Hahn spin echo [53] to wash out the correlated noise and get a $T_2$ time, and then compare it to the Ramsey coherence time $T_2^*$. This would help in separating the correlated noise from the uncorrelated noise. In the context of trapped ions, correlated noise arises from slow drifts such as a slow magnetic field drift (could be power line noise), while uncorrelated noise would be some fast white-noise such as a fluctuating patch potential on an electrode.

| | Carrier Ramsey (Fig. 4.5a) | Zeeman Ramsey (Fig. 4.5b) |
|---|---|---|
| $\alpha$ (Counts) | -11.78 | -4.75 |
| $\beta$ (Counts) | 2.07 | -2.06 |
| $\phi$ (rad/s) | -0.052 | -0.153 |
| $\delta$ (Hz) | 540 | 1855 |
| $\tau$ (ms) | 925 | 2.23 |
| $c$ (Counts) | 11.49 | 4.92 |

Table 4.2: Fit parameters for Figure 4.5

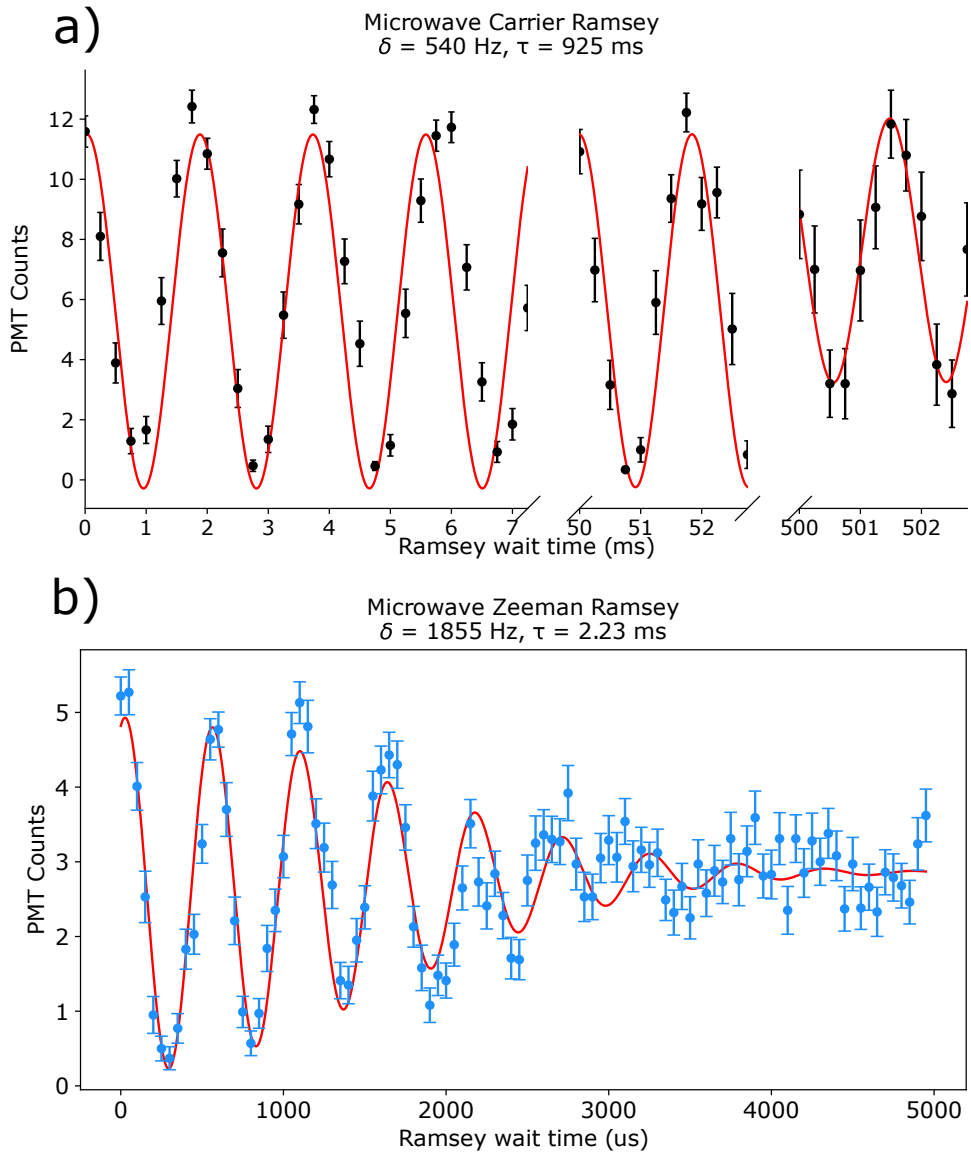



Figure 4.5: Ramsey scans taken within the groundstate hyperfine manifold of an $^{171}Yb^{+}$ ion in the blade trap. Both fits represent the lopsided Gaussian Ramsey from Equation 4.1, and the error bars are the standard error. a) Ramsey on the carrier. $|\uparrow\rangle$ equals to approximately 13 PMT counts. Averaged over 100 shots per point from 0-7 ms, 50 shots per point from 50-53 ms and 30 shots per point from 500-503 ms . b) Ramsey on $^2S_{1/2}\,|F=1, m_F=1\rangle$. $|\uparrow\rangle$ equals to approximately 5.5 counts. Averaged over 100 shots per point.

From Figure 4.5(a) on our qubit states, for the scan with $\delta = 540$ Hz, the associated Gaussian dephasing time $T_2^*$ for our qubit states is of $\tau = 925$ ms. Since the $^{171}Yb^+$ ground state hyperfine qubit $|F = 0, m_F = 0\rangle \rightarrow |F' = 1, m'_F = 0\rangle$ is first order insensitive to magnetic fields, it is not a great transition to quantify magnetic field noise. Other noise source such as Local Oscillator (LO) phase noise, LO power stability and ion hopping may contribute to the phase decoherence as much as the magnetic field noise [1]. Additionally, the fit performed in Figure 4.5(a) with Equation 4.1 may be a crude approximation since this fit does not consider uncorrelated noise sources which would have a $e^{-t/\tau}$ dependence [52]. Regardless, the important note from this data is that phase coherence remains for at least one second, which is plenty for quantum simulation experiments.

The data obtained from a Ramsey on the Zeeman transition of the $^{171}Yb^+$ ground state $|F = 0, m_F = 0\rangle \rightarrow |F' = 1, m'_F = 1\rangle$ can be a great indicator of the inherent magnetic field noise in Gauss. Because of its first-order sensitivity, the phase decoherence is dominated by magnetic field noise. The frequency of the $|F = 0, m_F = 0\rangle \rightarrow |F' = 1, m'_F = 1\rangle$ transition is given by [54, 55]

$$\omega_{Zeeman,+1}(B)/2\pi = \left(12642812118 + 1401080B + 310.8B^2\right) \text{ Hz}. \tag{4.2}$$

The splitting between the carrier and the Zeeman +1 transition was first found and determined to be 6.6196 MHz, and since the first-order Zeeman shift is about 1401080 Hz/G, the estimated magnetic field strength is $B = 4.728$ G. All magnets are permanent around the chamber, made of grade N52 neodymium. From the fit in Figure 4.5(b), the $T_2^*$ coherence time was of $\tau = 2.23$ ms. The magnetic field noise in our system is estimated by differentiating Equation 4.2

$$\delta\omega_{Zeeman,+1}(B)/2\pi = \frac{\partial\omega_{Zeeman,+1}(B)/2\pi}{\partial B}\delta B = (1401080 + 621.6B)\delta B \text{ Hz}, \tag{4.3}$$

and isolating $\delta B$ for

$$\delta B = \frac{\delta\omega_{Zeeman,+1}/2\pi}{(1401080 + 621.6B)} \text{ G}. \tag{4.4}$$

From our Zeeman dephasing time of 2.234 ms, I can convert this to a frequency shift $\delta\omega_{Zeeman,+1} = 1/T_2^* = 447.6$ Hz by inverting the dephasing time. From the result of Equation 4.4, I get a magnetic field noise of $\delta B = 0.318$ mG. To increase the Zeeman coherence time, we plan on implementing mu-metal shielding around the chamber. This can shield the ion from stray magnetic fields and some have observed a decrease of 40 dB in power line noise inside the box [1].

### 4.2.3 State preparation

For the following chapter, a well prepared ion state will be important for the measurements of the micromotion. As described above, before every experiment, the qubit is initialized in the $|\downarrow\rangle_z$ state. Applying a microwave $\pi$ pulse drives all the population to the $|\uparrow\rangle_z$ state. This measurement is repeated a 1000 times each for $|\downarrow\rangle_z$ and $|\uparrow\rangle_z$ state preparations, and afterwards we detect for a fixed time and bin our photon number for each state that was prepared. We then pick a discriminator value $d$ and name anything below dark and anything above bright.

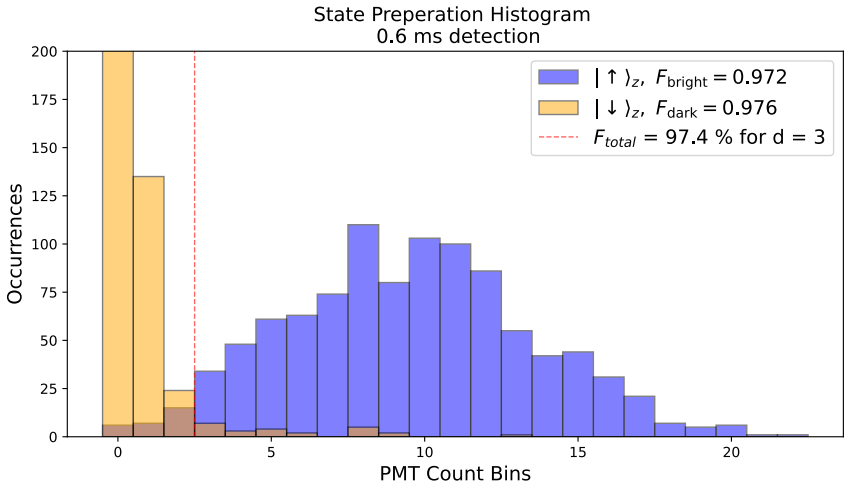



Figure 4.6: State preparation histogram for 0.6 ms detection. 1000 state preparations per state. Dark states histograms are the orange color bars, bright state histogram are the blue color bars and the brown represents overlap. Dotted red line is the discriminator discriminating the bright and dark states, here the optimal is for d = 3. Mean photon collection rate for the dark state is of 0.532 kHz while for the bright state is of 15.823 kHz.

The collected photons for the bright and dark histogram follow a Poisson distribution. As of now, we currently get 97.4% fidelity, and out main limitations are:

- High dark counts. Ideally the orange distribution only resides in the 0 bin. The imaging needs better shielding to decrease dark state collection rate.
- Hot ion. The orange events beyond the discriminator $d$ most likely happened because the ion was not prepared well.

- Limited photon collection. Imperfections with our current imaging system is causing us to lose photons, forcing us to detect for longer. This increases the collected background.

## 4.3 Chapter conclusion

In this chapter, I presented some first ion data. I first introduce the light delivery and the control system required to run experiments. I then characterized the microwave flopping and the state preparation fidelity of above 97 percent. Finally, I obtained phase coherence times from Ramsey sequences on the ground state hyperfine qubit states and Zeeman qubit states. We obtained a phase coherence time exceeding 0.9 s on the hyperfine qubit and a phase coherence time of only 2.23 ms on the Zeeman qubit becasuse of first-order sensitivity to magnetic field fluctuations. In the following chapter, I will further show experimental data collected to probe micromotion in the blade-style trap.

# Chapter 5

# Micromotion sensing with 935 nm repump

This section will outline the work I completed to probe micromotion in a blade style trap. I will first discuss the scheme used to probe micromotion, and then I will explain our implementation in our setup. Afterwards, I will show the results of the micromotion scans taken and discuss what was learned from these scans. I designed the optical system to probe micromotion, in addition to assembling it. The experimental team consisting of Shilpa Mahato, Lewis Hahn and Sakshee Samir Patil equally contributed towards preparing the system for running experiments. Individual contributions are listed in the introductory chapter. In terms of data collection, I primarily took it myself (approx 90%) with the help of Lewis Hahn who was present in the lab during the data collection to share ideas and debug the system. I then did the data analysis myself.

## 5.1 Probing micromotion with a repump transition

### 5.1.1 Micromotion detection scheme

To sense micromotion from a trapped $^{171}Yb^+$ ion in the blade trap, the first-order Doppler shift described in Equation 2.26 will be detected. Unfortunately, the 369 nm $^2S_{1/2} \rightarrow {}^2P_{1/2}$ transition has a linewidth $\Gamma_{369}/2\pi = 19.6$ MHz which is quite close to the trap drive frequency $\Omega_{rf}/2\pi = 35$ MHz. To probe the sidebands of a transition and get good resolution of the micromotion sidebands, it is essential to probe a transition with $\Gamma \ll \Omega_{rf}$. Fortunately for the $^{171}Yb^+$ ion, the $^2S_{1/2} \rightarrow {}^2P_{1/2}$ cycling transition is heavily reliant on the

presence of a 935 nm repump laser which drives population out of the $^2D_{3/2}$ manifold. The $^2P_{1/2}$ state has a 0.48% decay chance to $^2D_{3/2}$, and therefore the population is pumped out with a 935 nm laser resonant to $^2D_{3/2} \rightarrow {}^3[3/2]_{1/2}$ which conveniently then decays back to the ground state.

As such, since the 935 nm transition has a linewidth of $\Gamma_{935}/2\pi = 4.2$ MHz, the detuning around this resonance is varied to probe the modulated lineshape from micromotion because $\Gamma_{935} \ll \Omega_{rf}$. A regular detection sequence with 369 nm and 935 nm can then be performed with a varying 935 nm detuning $\Delta_{935}$ to probe the lineshape. This method was originally proposed by Goham and Britton [14], and our approach follows closely.

Figure 5.1(a) displays the relevant energy levels of the cooling, pumping and detection cycling transitions. During an ideal detection sequence, only the transitions denoted by solid lines are driven. Population starting in $^2S_{1/2}\,|F=1\rangle$ is in a cycling transition with $^2P_{1/2}\,|F=0\rangle$, and every so often population decays to $^2D_{3/2}\,|F=1\rangle$. Population can not decay to $^2D_{3/2}\,|F=2\rangle$ because the $^2P_{1/2} \rightarrow {}^2D_{3/2}$ is an E1 transition and therefore $\Delta F = 2$ is forbidden. Population trapped in $^2D_{3/2}\,|F=1\rangle$ then gets repumped with 935 nm light to ${}^3[3/2]_{1/2}\,|F=0\rangle$, which then has to decay to $^2S_{1/2}\,|F=1\rangle$ because $\Delta F = \Delta m_F = 0$ transitions are forbidden. The detection cycle is therefore closed and cycling without any population leakage besides off-resonant excitations.

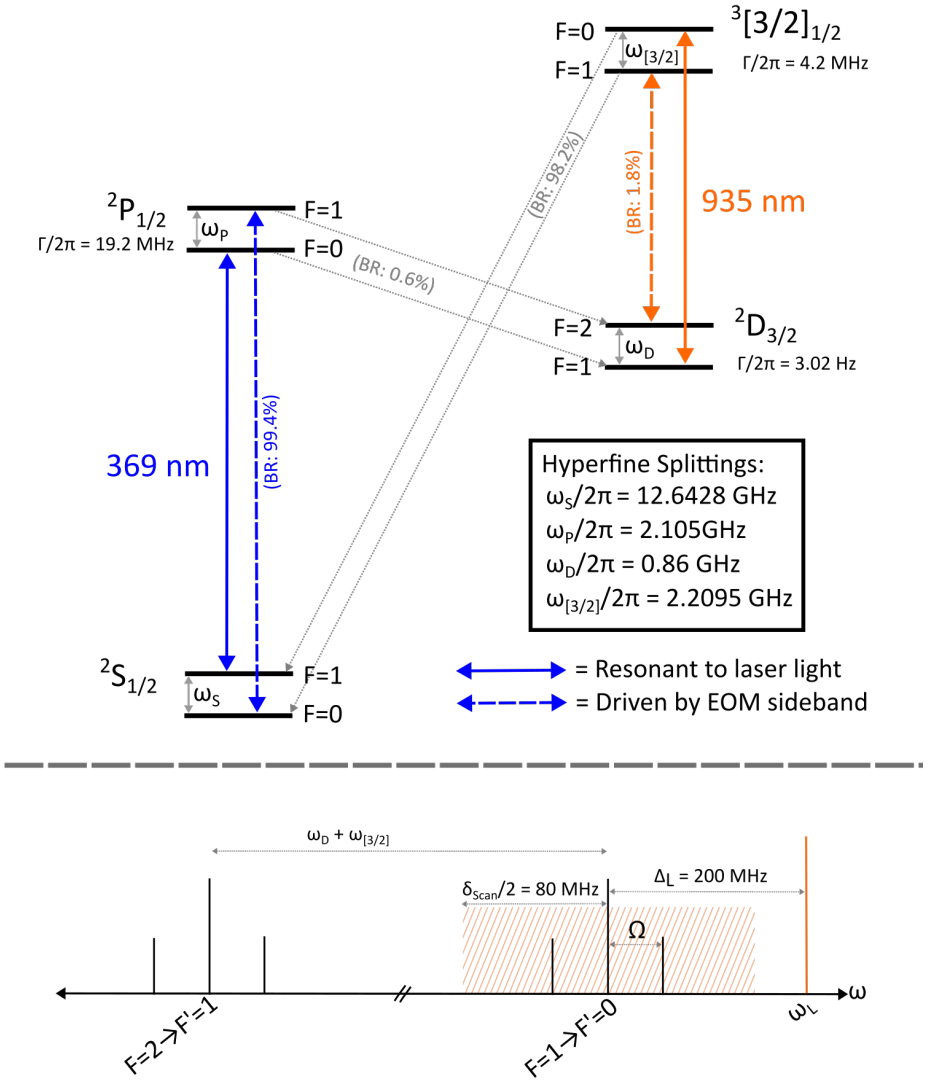



Figure 5.1: Probing micromotion with 935 nm repump transition. a) Relevant energy levels for the micromotion scans. Zeeman levels are not included. Colored lines represent laser driven transitions while dotted gray lines represent possible decays. Adapted from [14]. b) Relevant 935 nm transitions during micromotions scans. Orange shaded regions represents the range of frequencies that gets swept during a micromotion scan. Laser is blue-detuned from all resonances and an EOM drives all transitions.

The parameter that is being varied during one of these detection sequences is the detuning $\Delta_{935}$ from the ${}^2D_{3/2}\,|F=1\rangle \rightarrow {}^3[3/2]_{1/2}\,|F=0\rangle$ transition. Figure 5.1(b) shows the relevant transitions that are possible between these two manifolds. The two accessible optical transitions are the $|F=2\rangle \rightarrow |F'=1\rangle$, $|F=1\rangle \rightarrow |F'=0\rangle$ and their micromotion sidebands. During our detection sequence, the 935 nm laser frequency $\omega_L$ is set 200 MHz blue-detuned from the $|F=1\rangle \rightarrow |F'=0\rangle$ transition. At that location, it is frequency locked to our wavemeter to $\pm 1$ MHz. The 935 nm light is then passed to an EOM (Exail NIR-MPX950-LN-05), which has a bandwidth of DC-5 GHz. Using the maximized $-J_1$ order of the EOM, I am then able to drive any of the transitions displayed in 5.1(b). The detection range $\delta_{scan} = 160$ MHz was chosen so I can see up to two micromotion sidebands $J_1(\beta)$ and $J_2(\beta)$. Therefore, I send an RF signal to the EOM varying from 120 to 280 MHz, and that covers the carrier and 2 micromotion sidebands on each side. Because of the far off-resonant $|F=2\rangle \rightarrow |F'=1\rangle$ transition, the negative higher order EOM sidebands should be well off-resonant. All positive EOM sidebands are also off-resonant since the laser is blue-detuned from all resonances.

A few final important notes for this approach to work effectively is that:

- It is important to drive the 935 nm light at the saturation intensity $I_{sat}$. The saturation intensity is proportional to the inverse cube of the wavelength $I_{sat} \propto \lambda^{-3}$ [56], hence IR transitions typically have extremely low saturation intensities and are easily power broadened. Since I want to resolve the sidebands of the micromotion, this is non-negotiable ($\Gamma(I) \ll \Omega_{rf}$).
- A magnetic field is required for eliminating coherent dark states [57], as well for efficiently pumping population out of Zeeman states in the ${}^2D_{3/2}$ manifold. Since 935 nm light will be delivered from 3 orthogonal directions, each beam should contain a mixture of $\pi$ and $\sigma_{+/-}$ polarization.
- The laser locking stability matters. The 935 nm frequency should be locked to $\approx \pm 1$ MHz otherwise the laser frequency drift effectively broadens the Lorentzian lineshape, reducing resolvability of the sidebands. The locking of the 369 nm is also important, and in our case was locked to about $\pm 2$ MHz. It should be stable enough to keep detection counts steady over the full scan.

### 5.1.2 Experimental sequence

A subtle challenge with this approach is that the segments of the full experimental sequence (from cooling to collecting counts) require different 935 nm parameters. Figure 5.2 displays

the experimental sequence for a single shot of a micromotion scan at a given detuning $\Delta_{935}$. It begins by Doppler cooling for 3 ms, then optical pumping for 70 $\mu$s and a microwave $\pi$ pulse to prepare the $|\uparrow\rangle_z$ state. After this preparation, the 935 nm light's frequency and power are adjusted. Some of the components that will be introduced later have a slow switching time because of Micro-Electro-Mechanical Systems (MEMS) based switching. Finally, I state detect and collect fluorescence for 1 ms. To cover the full 160 MHz scan range shown in Figure 5.1(b), I take 2 MHz steps in $\Delta_{935}$, and for each step I take 100 shots for statistics.

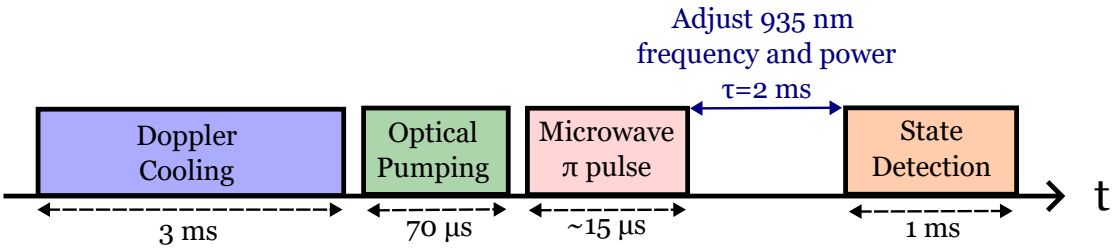



Figure 5.2: Micromotion probing experimental sequence. Typically, frequency steps of 2 MHz are taken for the full 160 MHz scan, and each one of these consists of 100 shots.

In this sequence, cooling and pumping have fairly different requirements in terms of the 935 nm light. Below I will describe the individual requirements.

**935 nm for Doppler Cooling and Optical Pumping**: During Doppler cooling, and optical pumping, strong 935 nm light ($I \gg I_{sat}$) is required while also covering both transitions shown in Figure 5.1(a). To target the $|F=1\rangle \rightarrow |F'=0\rangle$ and $|F=2\rangle \rightarrow |F'=1\rangle$ transitions, two tones are sent to the 935 nm EOM. Since the laser is blue-detuned by $\Delta_L = 200$ MHz, $\Delta_L = 200$ MHz and $\omega_D + \omega_{[3/2]} + \Delta_L = 3.27$ GHz is sent to the EOM. The power sent to the EOM is adjusted such that the unmodulated laser light is suppressed, and then we get a 1:4 ratio of $|F=2\rangle \rightarrow |F'=1\rangle : |F=1\rangle \rightarrow |F'=0\rangle$ light. This ratio is chosen because the $|F=2\rangle \rightarrow |F'=1\rangle$ transition is not driven as often during cooling. In terms of optical power, a lot of power is sent to ensure the cooling and optical pumping is not limited by the repump transition. Typically, $I \approx 100 \cdot I_{sat}$ is delivered. The power of the 935 nm light is controlled by a MEMS based Variable Voltage Attenuators (VVA).

**935 nm for State Detection**: For the state detection, the requirements are quite

different. During the cycling detection transition, only a singular tone near the $|F = 1\rangle \rightarrow |F' = 0\rangle$ is driven on the 935 nm transition. The EOM receives a frequency between $\Delta_L \pm (\delta_{scan}/2) = 200 \pm 80$ MHz. In terms of optical power, I want to be quite near $I \approx I_{sat}$ to avoid any power broadening of the transition to resolve the micromotion sidebands. This is experimentally determined by adjusting the VVA voltage until the linewidth is as small as possible without reducing the carrier peak amplitude by too much. These VVAs have a bandwidth of about 1 kHz, and hence why a 2 ms delay in Figure 5.1(b) is added before detection to update the optical power.

### 5.1.3 Probing micromotion from 3 directions

An extra layer of complexity comes into play when trying to sense micromotion along 3 orthogonal directions. The directions in which 935 nm is delivered was shown in Figure 4.1. To also control the power in each direction, 3 VVAs will be needed. The VVAs chosen can attenuate up to 30 dB.

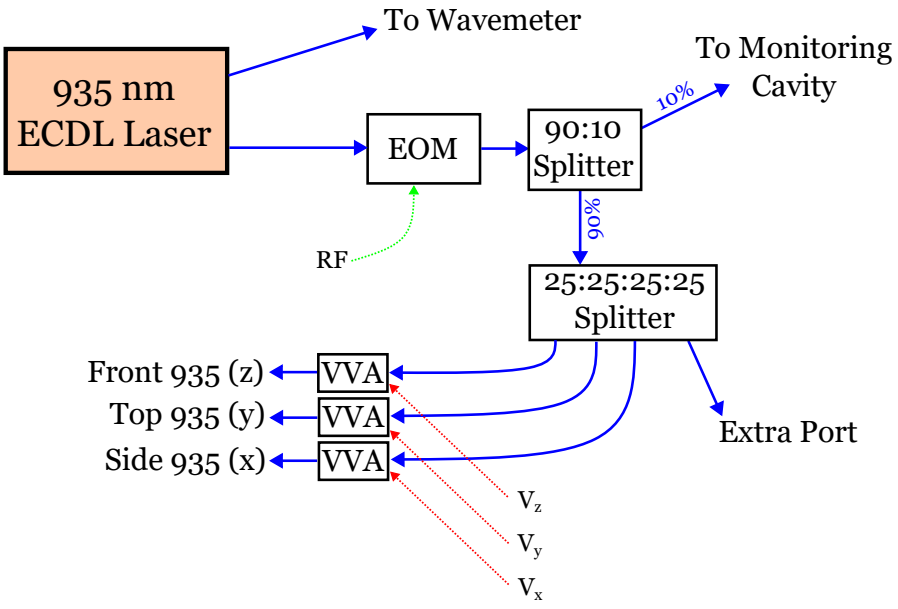



Figure 5.3: Distribution of the 935 nm light. All blue arrows represent in-fiber connection between components. Only the delivery and initial laser coupling are free space.

Figure 5.3 displays the in-fiber modulation, splitting and power control of the 935

nm light. The components include the EOM (Exail NIR-MPX950-LN-05), 90:10 splitter (Thorlabs TW930R2A1), a 4-way splitter (Thorlabs TWQ850HA) and VVAs (Thorlabs V800PA). All fibers interconnecting are polarization maintaining besides the fibers of the 4-way splitter. A portion of our light after the EOM is sent to a monitoring cavity (Thorlabs SA210-8B) with a 10 GHz Free Spectral Range (FSR) to monitor the sidebands produced by the EOM. This is very handy for optimizing the RF power to the EOM, and to ensure the control system is delivering the correct signals. Figure 5.4 displays a cavity scan when sending two tones to the EOM. The important tones are marked on the figure. All other tones are second-order modulations, which are off-resonanant to any transitions. The power of both RF tones ($\Delta$ and $\omega_{hf} = \omega_D + \omega_{[3/2]} + \Delta$) going to the EOM is optimized to suppress the $\omega_L$ tone. During cooling and pumping, $\Delta = 200$ MHz and during detection, the detuning $\Delta$ is somewhere between 120 MHz and 280 MHz.

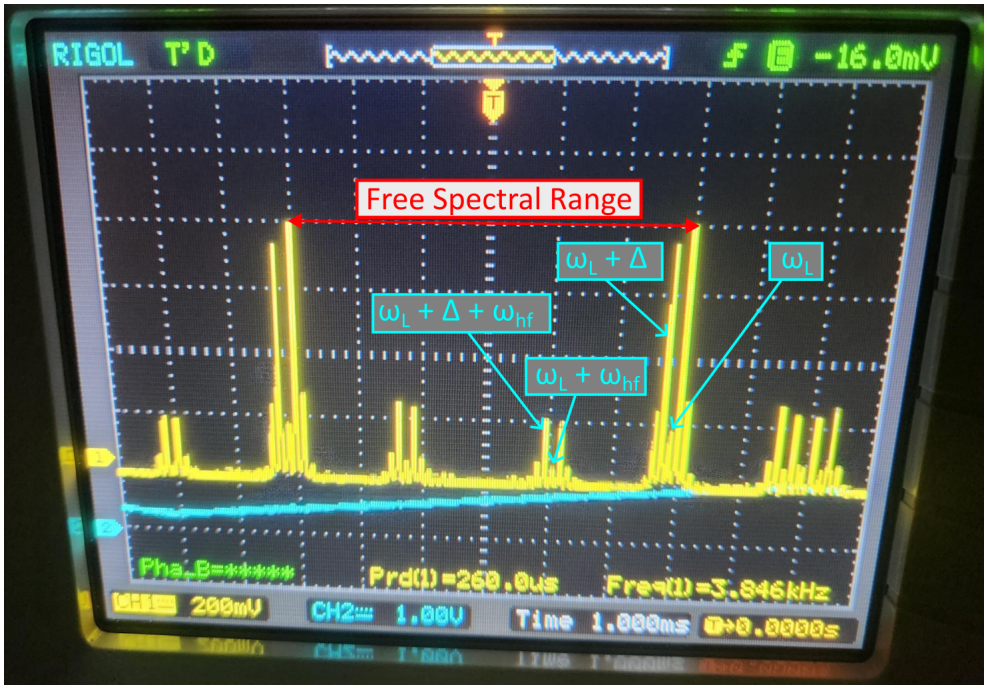



Figure 5.4: Trace on an oscilloscope of a 10 GHz FSR cavity sweep. The detuning $\Delta$ represents some arbitrary detuning between 120 and 280 MHz. The finesse of the cavity is above 150.

In terms of delivery to the chamber, light is delivered from 3 directions to probe micromotion along 3 orthogonal directions. As shown in Figure 4.1, one comes from the top ($\hat{y}$), one from the side ($\hat{x}$) and the final through the Photonic Crystal Fiber (PCF) ($\hat{z}$). Since

the PCF beam size is constrained by the reflective collimator that focuses the light, I could not select the beam size from the $\hat{z}$ direction. For the other beams, I chose to cylindrically focus the beam to have a very long elliptical beam at the ion location between the blades. The beam sizes and associated saturation intensities are given in Table 5.1.

| **Beam Direction** | **Beam waist** $1/e^2$ ($\mu$m) | $I_{sat}$ **(uW)** |
|---|---|---|
| Side 935 ($\hat{x}$) | $62 \times 720$ | 0.95 |
| Top 935 ($\hat{y}$) | $62 \times 720$ | 0.95 |
| PCF 935 ($\hat{z}$) | $50 \times 50$ | 0.053 |

Table 5.1: 935 nm beams for micromotion scans.

The light delivery is then simple since there are 3 fibers that need a few free-space optics to select polarization, and focus the light at the ion location. Figure 5.5(a) displays the in fiber components described above. They are placed in a metal box for isolation, and for ease of disconnecting inputs/outputs. Figure 5.5(b) displays the delivery used for 935 from the side and the top. The components used are a Thorlabs tilt and translation mount for alignment, an asphere for collimation (Thorlabs F240APC-980), a 935 nm half waveplate and a plano-convexe cylindrical lens (Thorlabs LJ1629RM-B). All fibers used to interconnect the components shown in Figure 5.3 are polarization maintaining (Thorlabs P3-780PM-FC-2).

## 5.2 Micromotion data

### 5.2.1 Minimizing micromotion

The purpose of this work is to characterize the micromotion present in our blade-style trap, and to find out how much compensation is needed to minimize it.

A typical micromotion minimization sequence will tackle one direction at a time. A scan will be repeated in one direction and voltages are adjusted until the stray electric field along that direction $\mathbf{E}_{dc} \cdot \hat{u}_i$ is compensated. Under ideal conditions, the compensation field along one direction should not affect the others. This is usually the case but it can vary because of slight misalignment of the hand assembled trap.

I began by getting a measurement of the micromotion present while applying no compensation voltages. This measure is important to determine the inherent level of micro-

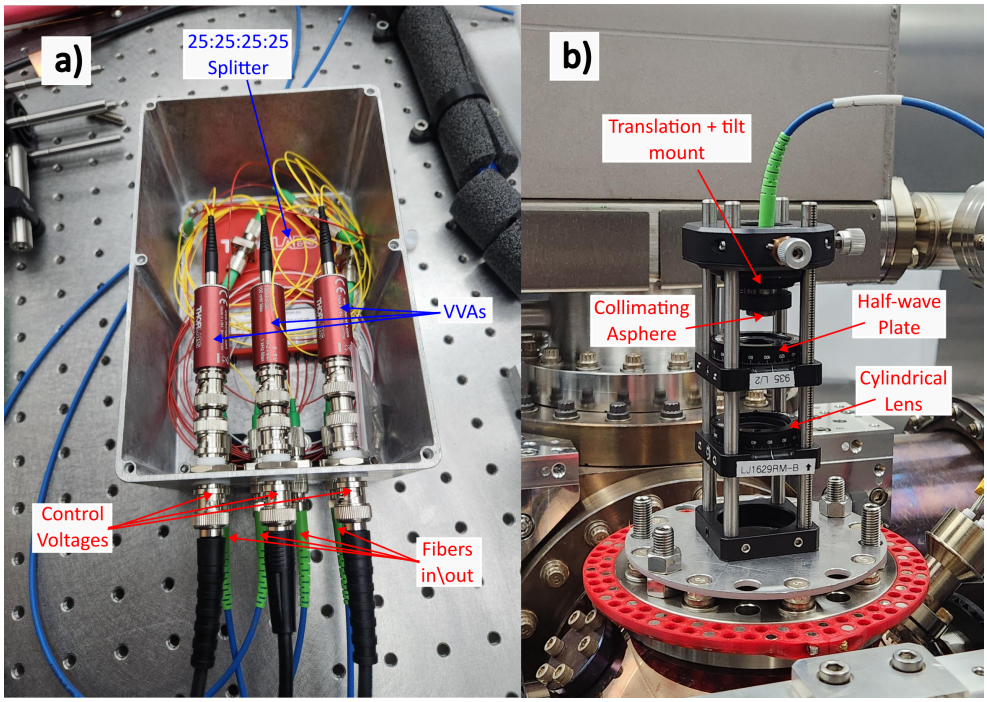



Figure 5.5: Delivery of the 935 nm light to the vacuum chamber. a) Box following the EOM which contains the 4-way fiber splitter and the VVAs. b) Assembly for the delivery of 935 nm from the top (as shown) and from the side (essentially identical but not shown). Beam is aligned with the translation and tilt mount holding the fiber collimator.

motion at the RF null[1] of the trap. Figure 5.6 displays micromotion scans along $\hat{x}, \hat{y}$ and $\hat{z}$. On these figures, the data is taken sweeping the frequency of the 935 nm light during a detection sequence shown in Figure 5.2. The fit is given by Equation 2.26. As a visual indicator, dotted black lines display where the micromotion sidebands would appear relative to the peak if they were present. I indicate the location of the first two order sidebands $\pm\Omega_{rf}, \pm 2\Omega_{rf}$. Micromotion is then quantified along all three directions with the modulation index $\beta$, and I observed a modulation index $\beta$ of 0.40(6) along $\hat{x}$, 0.33(7) along $\hat{y}$ and 0.48(6) along $\hat{z}$.

[1]RF null is the radial location at which the ions would reside if the all DC signals were turned completely off and only the RF was to be left on.

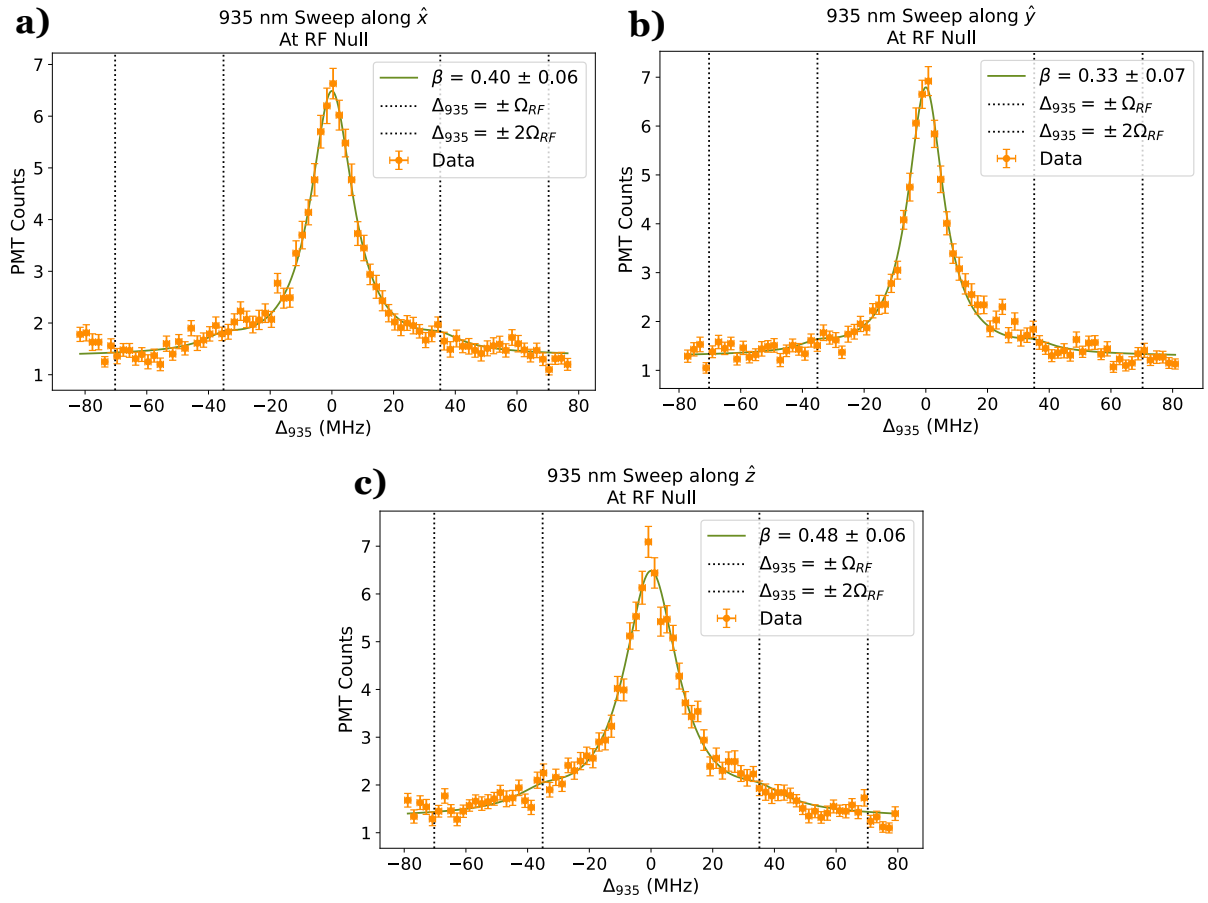



Figure 5.6: Micromotion at the RF null in the blade trap. Dotted lines indicate location of the micromotion sidebands relative to the fit peak. Horizontal error bars represent laser locking stability and vertical ones represent standard error from 100 shots. Green line represents fit of Equation 2.26. a) Scan with 935 along $\hat{x}$. b) Scan with 935 along $\hat{y}$. c) Scan with 935 along $\hat{z}$.

Another observation I made looking at these is that the linewidth $\Gamma$ looks much bigger than the expected natural linewidth of 4.2 MHz. From these fits, I get values $\Gamma_{fit}/2\pi \approx 13$ MHz, which is much larger than the expected $\sqrt{2}\Gamma_{935}/2\pi = 5.93$ MHz when at $I_{sat}$ [56]. My main concern is that the 935 power is higher than the saturation intensity ($I > I_{sat}$), because when continuously decreasing the power, the amplitude of the Lorentzian goes down and sidebands become hard to resolve. Therefore, I stay at the point where the

amplitude remains maximal until the smallest linewidth is achieved. This was a happy medium in terms of getting a good fit for $\beta$ and lowering the linewidth.

The good sign from Figure 5.6 is that the micromotion sidebands at the RF null are hardly resolvable, meaning that only small offset voltages will be necessary to compensate the small residual $\mathbf{E}_{dc}$ at the RF null.

### 5.2.2 Radial micromotion compensation

In a blade-style trap, radial micromotion is the easiest type of micromotion to compensate. The plethora of DC controls makes it easy to compensate the stray $\mathbf{E}_{dc}$ in the radial plane. It is important to note that under the condition where the trap geometry is not perfect, the radial micromotion null line may have a small angle with respect to the ion chain. In that case, only a single ion would truly reside at the micromotion null and others would reside very close to it. To characterize this, it would be insightful to probe micromotion for different ions in a chain and see if their radial null requires the same displacement voltages. This becomes a challenging problem and the segmented blade trap is one of the better suited traps to compensate this problem.

To get an idea of the location of the micromotion null[2] the ion is displaced in both $\hat{x}$ and $\hat{y}$ and micromotion scans are taken as the ion is displaced. This is done is both radial directions and plotted in Figure 5.7. The blue data points display the micromotion along $\hat{x}$ and the red ones along $\hat{y}$. The x axis represents the displacement voltages applied to the ions on pairs on blades as explained in Figure 3.9. $V_{right}$ and $V_{up}$ are positive on the x axis, while $V_{left}$ and $V_{down}$ are shown as negative on the x axis. All displacement voltages are positive DC voltages applied on a pair of blades.

[2]micromotion null is the location at which the ions experience no micromotion

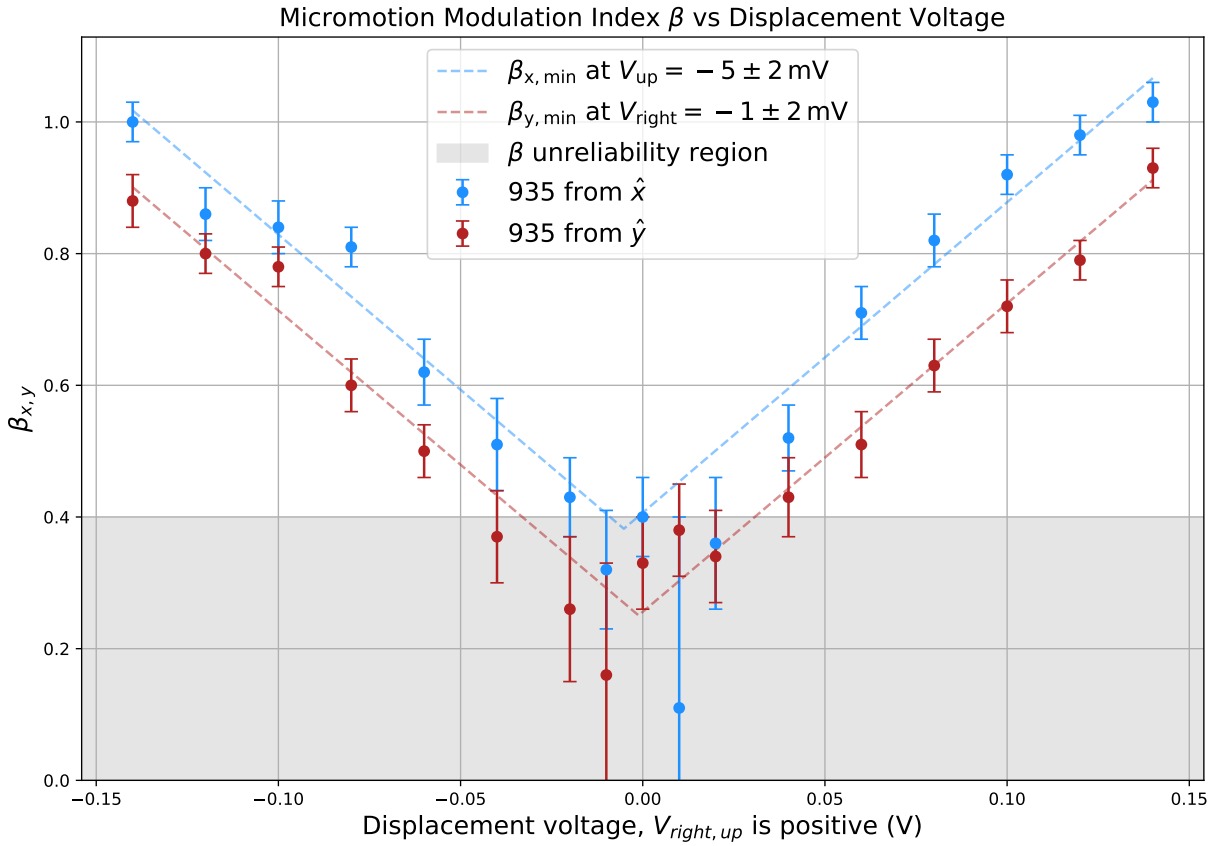



Figure 5.7: Micromotion modulation $\beta$ index scaling as the ion is displaced in both radial directions, blue for horizontal ($\hat{x}$) and red for vertical ($\hat{y}$). Error bars represent the standard deviation from the fit of the $\beta$ parameter. Grey area represents the region where the fitting of the micromotion modulation index $\beta$ can not be trusted because of poor resolvability.

The fit used in this figure is an absolute linear fit. This is an accurate fit because from Equation 2.25, $\beta_i \propto u_{0i}$. The displacement $u_{0i}$ from the offset electric field $\mathbf{E}_{dc}$ is also roughly linearly proportional to the displacement voltage $u_{0i} \propto V_{offset}$. This was confirmed with electrostatic simulations for the working voltage range. The minimum of this absolute linear fit can then serve as a close estimate for the location of the radial micromotion null. For both radial directions, it was estimated that a voltage of $V_{down} = 5 \pm 2$ mV and $V_{left} = 1 \pm 2$ mV was necessary to reach the null. Despite not being the most accurate way to pinpoint then null, this indicates that the alignment of the blades must be pretty good, since only a few millivolts are necessary to reach the micromotion null. From electrostatic

simulations, it was estimated that these displacement voltages correspond to displacements of less than 1 $\mu$m.

The fit on Figure 5.7 relies on the asymptotic scaling behavior of $\beta$ to estimate the micromotion null. A gray zone is added on the figure as an *unreliability fitting region* where the values of $\beta < 0.4$ can not be trusted. They can not be trusted because at such low micromotion, the first-order Doppler shift modulation of the Lorentzian becomes hidden below the lineshape of the Lorentzian itself. The delimiter $\beta < 0.4$ was chosen based off of where the error bars on $\beta$ become considerably large, indicating an unreliable fit. Once the two-photon Raman transition system is integrated in our trap, narrow linewidth sideband spectroscopy of the micromotion sidebands [15] will help in pinpointing the micromotion null around the point that this method located.

### 5.2.3 Micromotion along a long chain of ions

While having inherently low micromotion at the radial DC null of a hand assembled blade trap is impressive, ultimately the level of axial micromotion is more worrisome. Trapping a linear chain of ions in a quadrupole trap has the ions reside on the axial axis, and therefore ions are forced into a position with a stray field along $\hat{z}$ to remain in a linear chain. If on top of this there is a large stray and uniform $\mathbf{E}_{dc}$ along $\hat{z}$ or some projection of the RF onto the axial axis, these blade-style traps can become unusable because of the axial heating.

To simulate the effects of micromotion for ions in a long chain, 3 orthogonal micromotion scans are taken at the axial DC null ($z = 0$) and at ($z = 60$ $\mu$m). This distance is equivalent to the location of an ion at the edge of a chain of 25-30 ions, as shown in Figure 4.2. Figure 5.8 displays these color coded scans.

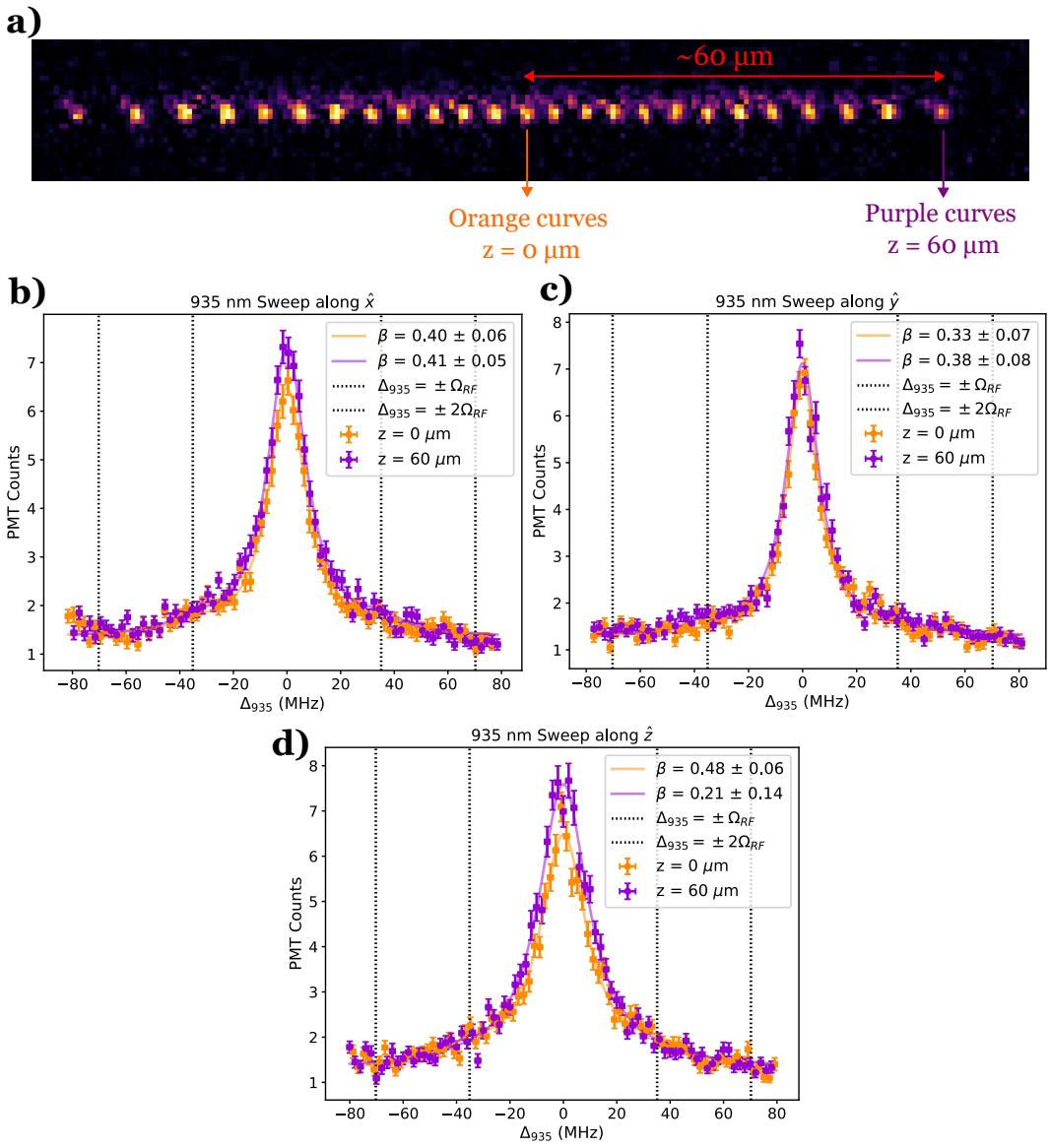



Figure 5.8: Micromotion along 3 orthogonal directions at center and edge of a long chain of ions. For this data, two ions are artificially pushed 60 $\mu$m away from the trap center. a) Image displaying where the ion was placed for both datasets. b-d) Micromotion scans along $\hat{x}$, $\hat{y}$ and $\hat{z}$ with an average of 100 shots per point.

The promising result from these scans is that the micromotion is low and the sidebands are non-resolvable for all 3 scans at the center and 60 microns away from the center. Data was taken at the other edge of the chain but was later found to be erroneous, and thus not presented because the beam alignment was poor after displacing the ion. The data therefore had very low signal to noise. While the axial micromotion is at a very low level at both positions, it does seem to be higher at the trap center. This could be an indication that the axial micromotion null is located slightly away from the geometric center of the trap. This will have to be investigated further by probing micromotion while varying its position axially.

All micromotion scans presented in this section exemplify that there is inherently low excess micromotion in our blade trap. Only small adjustments are required to compensate the radial excess micromotion, and the axial micromotion is hardly resolvable from Figure 5.8. As a comparison, Figure 5.9 displays a scan with a large stray electric field $V_{right} = 0.14$ V. This was included to show that all the scans taken earlier have very low micromotion, and that is a good sign. Also, this is a sign that the hand assembly procedure of the blade trap was a success, and the confining potentials do not cause strong excess micromotion at first glance. Ultimately, heating rates will be the key to understanding how much excess micromotion really affects the ions trapped in the blade trap.

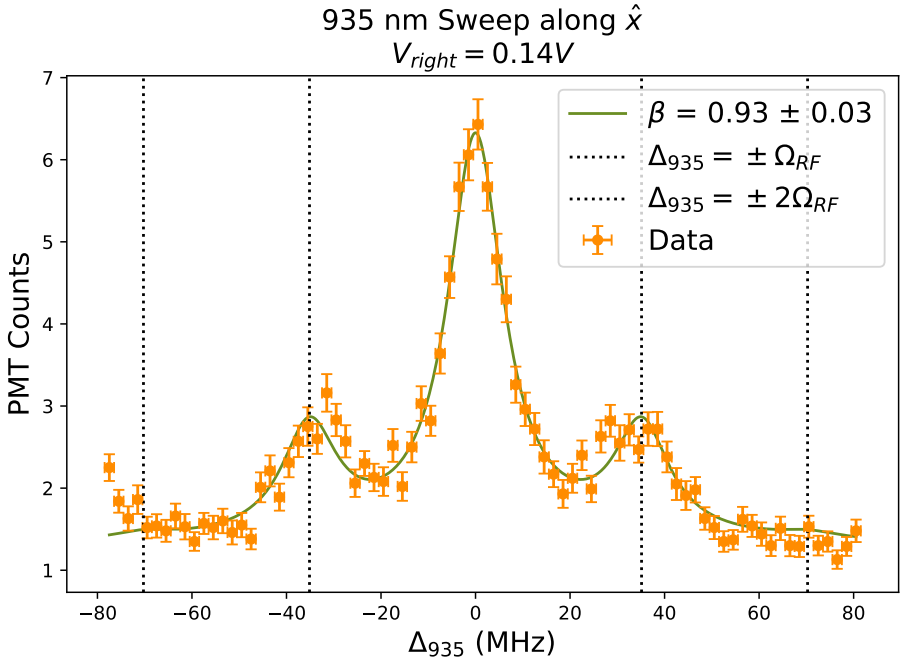



Figure 5.9: Micromotion scan along $\hat{x}$ with a bad stray electric field that was artificially added with $V_{right} = 0.14$ V. This is to exemplify that all scans above have very low micromotion compared to this.

## 5.3 Chapter conclusion

In this chapter, I presented the method used to probe and compensate micromotion in the blade-style trap. I first introduced the scheme for probing micromotion with the 935 nm repump transition in $^{171}Yb^{+}$. I then presented the experimental sequence along with the optical routing and delivery required to probe micromotion along all three spatial directions. Afterwards, experimental data was presented which shows that the blade-style trap has inherently low micromotion with no DC compensation fields. This indicates that the hand assembly was properly done. Additionally, I characterized the RF null positions in the radial plane, and found that it was only at a sub-micrometer distance from the DC null, and required very small compensation fields. More specifically, using Equation 2.25 and the radial $\beta$ values, the radial micromotion null was at a position $< 350$ nm away from the DC null. Finally, micromotion was probed along all three spatial directions at the center, and edge of a long chain of ions (25 ions). At both locations, low micromotion

was observed. This is a great indicator that for future large-scale quantum simulation, micromotion will not be problematic in this blade trap.

# Chapter 6

# Conclusion and outlook

In this thesis, I presented my work towards developing the electronic control and micromotion compensation in a multi-segmented blade-style ion trap. This work is relevant for the bring-up of this large-scale quantum simulator, which in the following years will have much of the infrastructure ready for the implementation quantum simulation protocols. Chapter 2 introduced the concept of trapping an ion in a quadrupole ion trap. From the equations of motion, I introduced the concept of micromotion and motivated why its presence is detrimental to quantum simulation experiments. I additionally introduced some basics of experimental ion trapping techniques. Chapter 3 discussed the multi-segmented blade-style trap, and gave an introduction of the electronic control capabilities due to the segmentation and balanced RF drive. It also discussed the out-of-vacuum electronics and the mixing PCB that I designed. Chapter 4 presented some of the first data that was collected with the blade-style trap. A long chain of 25 ions was displayed, and the phase coherence time was calculated for our ground-state hyperfine qubit to be above 0.9 s. Chapter 5 displayed the efforts towards probing and minimizing micromotion in the blade-style trap. I introduced the sideband spectroscopic method of a narrow-linewidth transition for probing micromotion, and then explained how this would be implement for our ion of choice in our blade trap. I then presented some data demonstrating that there is inherently low micromotion in our hand-assembled trap, required very little compensation to reach the micromotion minima. Additionally, it was shown that there is inherently low micromotion at the edge of a long chain of ions, which will be crucial for large-scale quantum simulation experiments.

During the two years of this degree, much has evolved in the laboratory with the blade trap. When I started, our "lab" was a storage room, and it was completely transformed into a temperature and humidity stabilized space to house our experiment. Nikhil Kotibhaskar,

Sainath Motlakunta and Lewis Hahn closed the vacuum chamber a few months after my arrival, and brought it into the lab. Once it arrived, the whole team including Shilpa Mahato, Lewis Hahn, Sakshee Samir Patil and myself worked towards getting the system ready for experiments. We were then able to get microwave Ramsey scans to obtain qubit phase coherence times exceeding 0.9 s. Additionally, micromotion was probed and minimized in the ion trap.

This thesis covered two important topics. First, I presented our novel approach of having a fully out-of-vacuum electronics delivery, mixing and filtering for the blade-style trap. The mixing PCB was designed to reach some target specifications which were set by experimental targets of trap frequency, filtering requirements and RF phase matching. Additionally, I presented my design of a balanced RF helical resonator. This balanced RF drive allows us to reach high secular trap frequencies ($> 5$ MHz) which will be important for fast quantum logic gates, and lower spectral crowding. I also studied RF phase matching errors between electrodes and its effects on intrinsic and excess micromotion along all three spatial directions. The results demonstrate that phase matching is quite important in this multi-segmented trap since small phase errors can lead to significant micromotion. Secondly, I introduced our method for probing micromotion in our blade-style trap. This was done using the narrow linewidth of our 935 nm transition in $^{171}Yb^{+}$, and performing sideband spectroscopy [14]. I introduced the optical delivery requirements for probing the micromotion along all three spatial directions, and presented the experimental sequence that was used to probe micromotion. I then displayed some data that showed two promising results. Our blade trap has inherently low micromotion at the DC null and requires very low displacements $< 1$ $\mu$m to reach the micromotion null in the radial directions. It was also shown that there is low micromotion at the edge of a long chain of ions in all three spatial directions. This exemplifies that this multi-segmented blade-style trap design induces low micromotion, and the hand assembly method used provided great alignment of the blades. Additionally, it goes to show that hand assembled blade-style traps can reach inherently low micromotion levels comparable to what a micro fabricated trap would reach.

A few challenges remain with the electronics and the micromotion probing. In terms of electronics, a remaining challenge is to find a good way to phase match all of the RF between all of the electrodes. While being a purely electronics problem, this becomes challenging when trying to minimize the loading of the resonator itself. Our PCB already loads our resonator by $> 10$ pF, and I am hoping to find a way to cut down on this, as this directly reduces the quality factor $Q$ of our balanced resonator. In terms of probing and minimizing micromotion, a major challenge that remains for this method to work best is to increase the resolvability of the sidebands. As displayed in Figure 5.7, small values of $\beta$ were not trusted because of the hardly resolvable sidebands. The linewidth of the

transition was measured to be higher than expected ($\Gamma_{935}/2\pi = 4.2$ MHz) during scans. I need to investigate why that is, and how to push the linewidth of a transition during a scan to its natural linewidth. Additionally, other things such as total photon collection and background reduction will help for this process.

A few future outlooks for the continuation of this work will be discussed, including the design a resonator PCB to combine with the mixing PCB. I am hoping that packaging both together will yield better quality factor $Q$ by reducing the loading on our capacitive load. Also, I am currently investigating the best DC filtering options, in addition to simulating various electronic strategies for phase matching all the RF lines. As we plan on soon taking heating rates, lots of grounding strategies will be employed to minimize any spectral noise that reaches the ion. In terms of micromotion, I am hoping to eventually automate the process of micromotion compensation when changing the secular frequencies. Implementation of machine learning tools to minimize micromotion for some secular frequencies will be an important tool for future calibrations. Additionally, I would like to explore other sideband spectroscopic methods for minimizing micromotion in the radial directions. Using a two-photon Raman process, we would like to probe the micromotion sidebands on this ultra-narrow linewidth transition to further minimize radial micromotion.

While this work marks a small step towards characterizing and engineering a large-scale quantum simulator, these studies are important to ensure that our multi-segmented blade-style trap remains at the forefront of ion trapping quantum technologies. Further engineering advances for quantum technologies are imperative for scalable trapped ion devices, and each advancement brings us one step closer to large-scale quantum computation and simulation.

# References


[1] Pengfei Wang, Chun-Yang Luan, Mu Qiao, Mark Um, Junhua Zhang, Ye Wang, Xiao Yuan, Mile Gu, Jingning Zhang, and Kihwan Kim. Single ion qubit with estimated coherence time exceeding one hour. *Nature Communications*, 12(1):233, Jan 2021.

[2] M. C. Smith, A. D. Leu, K. Miyanishi, M. F. Gely, and D. M. Lucas. Single-qubit gates with errors at the $10^{-7}$ level, 2025.

[3] C. M. Löschnauer, J. Mosca Toba, A. C. Hughes, S. A. King, M. A. Weber, R. Srinivas, R. Matt, R. Nourshargh, D. T. C. Allcock, C. J. Ballance, C. Matthiesen, M. Malinowski, and T. P. Harty. Scalable, high-fidelity all-electronic control of trapped-ion qubits, 2024.

[4] Fangzhao Alex An, Anthony Ransford, Andrew Schaffer, Lucas R. Sletten, John Gaebler, James Hostetter, and Grahame Vittorini. High fidelity state preparation and measurement of ion hyperfine qubits with $I > \frac{1}{2}$. *Physical Review Letters*, 129(13), September 2022.

[5] J. M. Pino, J. M. Dreiling, C. Figgatt, J. P. Gaebler, S. A. Moses, M. S. Allman, C. H. Baldwin, M. Foss-Feig, D. Hayes, K. Mayer, C. Ryan-Anderson, and B. Neyenhuis. Demonstration of the trapped-ion quantum ccd computer architecture. *Nature*, 592(7853):209–213, April 2021.

[6] F. W. Knollmann, E. Clements, P. T. Callahan, M. Gehl, J. D. Hunker, T. Mahony, R. McConnell, R. Swint, C. Sorace-Agaskar, I. L. Chuang, J. Chiaverini, and D. Stick. Integrated photonic structures for photon-mediated entanglement of trapped ions. *Optica Quantum*, 2(4):230, August 2024.

[7] Arinjoy De, Alessio Lerose, De Luo, Federica M. Surace, Alexander Schuckert, Elizabeth R. Bennewitz, Brayden Ware, William Morong, Kate S. Collins, Zohreh Davoudi,

Alexey V. Gorshkov, Or Katz, and Christopher Monroe. Observation of string-breaking dynamics in a quantum simulator, 2024.

[8] Shi-An Guo, Yu-Kai Wu, Jing Ye, Lin Zhang, Ye Wang, Wen-Qian Lian, Rui Yao, Yu-Lin Xu, Chi Zhang, Yu-Zi Xu, Bin-Xiang Qi, Pan-Yu Hou, Li He, Zi-Chao Zhou, and Lu-Ming Duan. Hamiltonian learning for 300 trapped ion qubits with long-range couplings. *Science Advances*, 11(5):eadt4713, 2025.

[9] Visal So, Midhuna Duraisamy Suganthi, Abhishek Menon, Mingjian Zhu, Roman Zhuravel, Han Pu, Peter G. Wolynes, José N. Onuchic, and Guido Pagano. Trapped-ion quantum simulation of electron transfer models with tunable dissipation. *Science Advances*, 10(51):eads8011, 2024.

[10] D. Main, P. Drmota, D. P. Nadlinger, E. M. Ainley, A. Agrawal, B. C. Nichol, R. Srinivas, G. Araneda, and D. M. Lucas. Distributed quantum computing across an optical network link. *Nature*, 638(8050):383–388, Feb 2025.

[11] Joonhyuk Kwon, William J. Setzer, Michael Gehl, Nicholas Karl, Jay Van Der Wall, Ryan Law, Matthew G. Blain, Daniel Stick, and Hayden J. McGuinness. Multi-site integrated optical addressing of trapped ions. *Nature Communications*, 15(1):3709, May 2024.

[12] D. J. Berkeland, J. D. Miller, J. C. Bergquist, W. M. Itano, and D. J. Wineland. Minimization of ion micromotion in a paul trap. *Journal of Applied Physics*, 83(10):5025–5033, 05 1998.

[13] T. R. Tan, R. Kaewuam, K. J. Arnold, S. R. Chanu, Zhiqiang Zhang, M. S. Safronova, and M. D. Barrett. Suppressing inhomogeneous broadening in a lutetium multi-ion optical clock. *Phys. Rev. Lett.*, 123:063201, Aug 2019.

[14] Connor J. B. Goham and Joseph W. Britton. Resolved-sideband micromotion sensing in $Yb^+$ on the 935nm repump transition. *AIP Advances*, 12(11):115315, 11 2022.

[15] K. J. Arnold, N. Jayjong, M. L. D. Kang, Qin Qichen, Zhao Zhang, Qi Zhao, and M. D. Barrett. Enhanced micromotion compensation using a phase-modulated light field. *Phys. Rev. A*, 110:033115, Sep 2024.

[16] D. P. Nadlinger, P. Drmota, D. Main, B. C. Nichol, G. Araneda, R. Srinivas, L. J. Stephenson, C. J. Ballance, and D. M. Lucas. Micromotion minimisation by synchronous detection of parametrically excited motion, 2021.

[17] Moji Ghadimi, Alexander Zappacosta, Jordan Scarabel, Kenji Shimizu, Erik W. Streed, and Mirko Lobino. Dynamic compensation of stray electric fields in an ion trap using machine learning and adaptive algorithm. *Scientific Reports*, 12(1):7067, Apr 2022.

[18] G Pagano, P W Hess, H B Kaplan, W L Tan, P Richerme, P Becker, A Kyprianidis, J Zhang, E Birckelbaw, M R Hernandez, Y Wu, and C Monroe. Cryogenic trapped-ion system for large scale quantum simulation. *Quantum Science and Technology*, 4(1):014004, October 2018.

[19] K. G. Johnson, J. D. Wong-Campos, A. Restelli, K. A. Landsman, B. Neyenhuis, J. Mizrahi, and C. Monroe. Active stabilization of ion trap radiofrequency potentials. *Review of Scientific Instruments*, 87(5), May 2016.

[20] I. Pogorelov, T. Feldker, Ch. D. Marciniak, L. Postler, G. Jacob, O. Krieglsteiner, V. Podlesnic, M. Meth, V. Negnevitsky, M. Stadler, B. Höfer, C. Wächter, K. Lakhmanskiy, R. Blatt, P. Schindler, and T. Monz. Compact ion-trap quantum computing demonstrator. *PRX Quantum*, 2:020343, Jun 2021.

[21] Shuqi Xu, Xiaoxing Xia, Qian Yu, Sumanta Khan, Eli Megidish, Bingran You, Boerge Hemmerling, Andrew Jayich, Juergen Biener, and Hartmut Häffner. 3d-printed micro ion trap technology for scalable quantum information processing, 2023.

[22] Soon Teh, Ezra Kassa, Shaobo Gao, Shuma Oya, and Hiroki Takahashi. Ion trapping with a laser-written 3D miniaturized monolithic linear paul trap for microcavity integration, 2024.

[23] Dominik Kiesenhofer, Helene Hainzer, Artem Zhdanov, Philip C. Holz, Matthias Bock, Tuomas Ollikainen, and Christian F. Roos. Controlling two-dimensional coulomb crystals of more than 100 ions in a monolithic radio-frequency trap. *PRX Quantum*, 4:020317, Apr 2023.

[24] Wolfgang Paul and Helmut Steinwedel. Notizen: Ein neues massenspektrometer ohne magnetfeld. *Zeitschrift für Naturforschung A*, 8(7):448–450, 1953.

[25] Wolfgang Paul. Electromagnetic traps for charged and neutral particles. *Rev. Mod. Phys.*, 62:531–540, Jul 1990.

[26] Steven Matthew Olmschenk. *Quantum Teleportation Between Distant Matter Qubits*. Ph.d. dissertation, University of Michigan, Ann Arbor, USA, 2009.

[27] Pei Jiang Low. *Tolerable experimental imperfections for a quadrupole blade ion trap and practical qudit gates with trapped ions*. M.sc. thesis, University of Waterloo, Waterloo, Canada, 2019.

[28] Gerard Higgins, Shalina Salim, Chi Zhang, Harry Parke, Fabian Pokorny, and Markus Hennrich. Micromotion minimization using ramsey interferometry. *New Journal of Physics*, 23(12):123028, dec 2021.

[29] Nikhil Kotibhaskar. *Design and construction of an ion trapping apparatus for quantum simulation experiments*. M.sc. thesis, University of Waterloo, Waterloo, Canada, 2019.

[30] J. Keller, H. L. Partner, T. Burgermeister, and T. E. Mehlstäubler. Precise determination of micromotion for trapped-ion optical clocks. *Journal of Applied Physics*, 118(10):104501, 09 2015.

[31] Yang Liu, Qi-feng Lao, Peng-fei Lu, Xin-xin Rao, Hao Wu, Teng Liu, Kun-xu Wang, Zhao Wang, Ming-shen Li, Feng Zhu, and Le Luo. Minimization of the micromotion of trapped ions with artificial neural networks. *Applied Physics Letters*, 119(13):134002, 09 2021.

[32] R. Blümel, C. Kappler, W. Quint, and H. Walther. Chaos and order of laser-cooled ions in a paul trap. *Phys. Rev. A*, 40:808–823, Jul 1989.

[33] R. G. DeVoe, J. Hoffnagle, and R. G. Brewer. Role of laser damping in trapped ion crystals. *Phys. Rev. A*, 39:4362–4365, May 1989.

[34] Anders Sørensen and Klaus Mølmer. Quantum computation with ions in thermal motion. *Phys. Rev. Lett.*, 82:1971–1974, Mar 1999.

[35] Seyed Shakib Vedaie, Eduardo J. Páez, Nhung H. Nguyen, Norbert M. Linke, and Barry C. Sanders. Bespoke pulse design for robust rapid two-qubit gates with trapped ions. *Phys. Rev. Res.*, 5:023098, May 2023.

[36] M. Cetina, L.N. Egan, C. Noel, M.L. Goldman, D. Biswas, A.R. Risinger, D. Zhu, and C. Monroe. Control of transverse motion for quantum gates on individually addressed atomic qubits. *PRX Quantum*, 3:010334, Mar 2022.

[37] U. Poschinger, A. Walther, K. Singer, and F. Schmidt-Kaler. Observing the phase space trajectory of an entangled matter wave packet. *Phys. Rev. Lett.*, 105:263602, Dec 2010.

[38] Wayne M. Itano, James C. Bergquist, John J. Bollinger, and David J. Wineland. Cooling methods in ion traps. *Physica Scripta*, T59:106, 1995.

[39] Sainath Motlakunta. *Developing a Large-Scale, Programmable Trapped Ion Quantum Simulator with In Situ Mid-Circuit Measurement and Reset*. Ph.d. thesis, University of Waterloo, Waterloo, Canada, 2023.

[40] Y. Castin, H. Wallis, and J. Dalibard. Limit of doppler cooling. *J. Opt. Soc. Am. B*, 6(11):2046–2057, Nov 1989.

[41] A. J. Rasmusson, Marissa D'Onofrio, Yuanheng Xie, Jiafeng Cui, and Philip Richerme. Optimized pulsed sideband cooling and enhanced thermometry of trapped ions. *Phys. Rev. A*, 104:043108, Oct 2021.

[42] Regina Lechner, Christine Maier, Cornelius Hempel, Petar Jurcevic, Ben P. Lanyon, Thomas Monz, Michael Brownnutt, Rainer Blatt, and Christian F. Roos. Electromagnetically-induced-transparency ground-state cooling of long ion strings. *Phys. Rev. A*, 93:053401, May 2016.

[43] Michael A. Nielsen and Isaac L. Chuang. *Quantum Computation and Quantum Information: 10th Anniversary Edition*. Cambridge University Press, 2010.

[44] Nikhil Kotibhaskar. *Towards Large Scale Quantum Simulations with Trapped Ions: Programmable XY model, Precise Light Sensing, and Extreme High Vacuum*. Ph.d. thesis, University of Waterloo, Waterloo, Canada, 2024.

[45] Lewis Hahn. *Developing a robust quantum simulator with trapped ions*. M.sc. thesis, University of Waterloo, Waterloo, Canada, 2024.

[46] M. Brownnutt, M. Kumph, P. Rabl, and R. Blatt. Ion-trap measurements of electric-field noise near surfaces. *Reviews of Modern Physics*, 87(4):1419–1482, December 2015.

[47] Joshua M. Wilson, Julia N. Tilles, Raymond A. Haltli, Eric Ou, Matthew G. Blain, Susan M. Clark, and Melissa C. Revelle. In situ detection of rf breakdown on micro-fabricated surface ion traps. *Journal of Applied Physics*, 131(13):134401, 04 2022.

[48] J. D. Siverns, L. R. Simkins, S. Weidt, and W. K. Hensinger. On the application of radio frequency voltages to ion traps via helical resonators. *Applied Physics B*, 107(4):921–934, Jun 2012.

[49] Ron Kapusta, Haiyang Zhu, and Colin Lyden. Sampling circuits that break the kT/C thermal noise limit. In *Proceedings of the IEEE 2013 Custom Integrated Circuits Conference*, pages 1–6, 2013.

[50] Sébastien Bourdeauducq, Robert Jördens, Peter Zotov, Joe Britton, Daniel Slichter, David Leibrandt, David Allcock, Aaron Hankin, Florent Kermarrec, Yann Sionneau, Raghavendra Srinivas, Ting Rei Tan, and Justin Bohnet. ARTIQ 1.0. https://doi.org/10.5281/zenodo.51303, May 2016. Version 1.0.

[51] Norman F. Ramsey. A molecular beam resonance method with separated oscillating fields. *Phys. Rev.*, 78:695–699, Jun 1950.

[52] Thomas Monz. *Quantum information processing beyond ten ion-qubits*. Ph.d. dissertation, University of Innsbruck, Innsbruck, Austria, 2011.

[53] E. L. Hahn. Spin echoes. *Phys. Rev.*, 80:580–594, Nov 1950.

[54] P.T.H. Fisk, M.J. Sellars, M.A. Lawn, and G. Coles. Accurate measurement of the 12.6 GHz "clock" transition in trapped $^{171}Yb^{+}$ ions. *IEEE Transactions on Ultrasonics, Ferroelectrics, and Frequency Control*, 44(2):344–354, 1997.

[55] J. Z. Han, B. Q. Lu, N. C. Xin, Y. M. Yu, H. R. Qin, S. T. Chen, Y. Zheng, J. G. Li, J. W. Zhang, and L. J. Wang. Precise determination of ground-state hyperfine splitting and calculation of zeeman coefficients for $^{171}Yb^{+}$ microwave frequency standard, 2023.

[56] Christopher J. Foot. *Atomic physics*. Oxford master series in atomic, optical, and laser physics. Oxford University Press, Oxford, 2007.

[57] S. Ejtemaee, R. Thomas, and P. C. Haljan. Optimization of $Yb^{+}$ fluorescence and hyperfine-qubit detection. *Phys. Rev. A*, 82:063419, Dec 2010.

[58] Q. A. Turchette, Kielpinski, B. E. King, D. Leibfried, D. M. Meekhof, C. J. Myatt, M. A. Rowe, C. A. Sackett, C. S. Wood, W. M. Itano, C. Monroe, and D. J. Wineland. Heating of trapped ions from the quantum ground state. *Phys. Rev. A*, 61:063418, May 2000.

[59] W. W. Macalpine and R. O. Schildknecht. Coaxial resonators with helical inner conductor. *Proceedings of the IRE*, 47(12):2099–2105, 1959.